UNIVERSITÀ
DEGLI STUDI
DI BRESCIA

DOTTORATO DI RICERCA IN INGEGNERIA DELL'INFORMAZIONE
FIS/01 Fisica Sperimentale

CICLO XXXVI

MODELING ANTINUCLEON-NUCLEUS INTERACTIONS AT LOW ENERGY: ANALYSIS OF EXPERIMENTAL DATA USING AN OPTICAL POTENTIAL APPROACH

Dottorando: Stefano Migliorati

Relatore: Professor Luca Venturelli

Contents

List of Figures

List of Tables

A tutte le persone
che non hanno
mai avuto
una dedica.

Abstract

The current understanding of the processes of elastic scattering and annihilation of antinucleons with matter – particularly at low energy ($E < 50\,\mathrm{MeV}$) – is limited to a narrow set of data involving a few specific nuclei in a constrained phase space. To study these interactions, a phenomenological model is needed to infer information from the available experimental data. This information can help modify and refine the model to reproduce the data better and understand the underlying theory. The present work uses a complex optical potential called the Woods-Saxon potential, a phenomenological model to study the cross sections for elastic and reaction scattering of antiprotons on four different targets (carbon-12, oxygen-16, calcium-40, and lead-208) at different projectile momenta (between 300 and 600 MeV/c). Solving the Schrödinger equation, the cross sections are calculated and then the parameters of the Woods-Saxon optical potential are determined by fitting to the experimental data, using chi-square minimization.

The results indicate that for light nuclei (such as carbon and oxygen) there are different values of the strength parameters (potential energies) than for medium and heavy nuclei (such as calcium and lead). The geometrical parameters, which describe the shape of the nuclei, are quite similar among the different fits. However, the cross-sections appear very sensitive to these geometrical parameters and are strongly correlated with the strength potential parameters. These results, adopting some simplifying assumptions, are used to make predictions at low energies for elastic scattering of antiprotons. These predictions show that for future experiments the lowest value of momentum of antiprotons to make feasible measurements for the study of nuclear interactions is 50 MeV/c ($E \sim 1.3\,\mathrm{MeV}$). Below this value, the nuclear interaction contribution is hidden by the dominant Coulomb interaction. These projections can be valuable for designing future experiments to be carried out at facilities where low-energy antimatter is studied, such as ELENA at the Antiproton Decelerator at CERN (Geneva) or FLAIR at GSI in Germany. In addition, fitting parameters are used to estimate the antineutron-neutron oscillation time, a useful quantity for designing experiments to study this hypothetical phenomenon. Lower time limits for this time are in agreement with previous results. The observation of the antineutron-neutron oscillation is significant for understanding matter-antimatter asymmetry and the eventual baryonic number non-conservation.

This analysis is a first attempt to the purpose of constructing a reliable single nuclear model, whose values are based on fits made to all available data (both elastic scattering and reactions). To achieve this, all the data are needed, which unfortunately are unavailable in the online databases. Further analysis with some modifications to the model used (including, for example, momentum dependence, detailed study of the correlations of the fitting parameters, and different parametrizations of the model...) would be desirable to understand some discrepancies (e.g., the anomaly observed in the cross sections of antiprotons and antineutrons), to investigate in depth the interactions at low energies for antimatter, and to make predictions to design new experiments that can shed light on the interaction between matter and antimatter at low energy.

La comprensione attuale dei processi di scattering elastico e annichilazione degli antinucleoni con la materia – in particolare a bassa energia ($E < 50\,\mathrm{MeV}$) - è limitata ad un ristretto numero di dati che coinvolgono alcuni nuclei specifici in uno spazio delle fasi vincolato. Per studiare queste interazioni, è necessario un modello fenomenologico per inferire informazioni dai dati sperimentali disponibili. Queste informazioni possono aiutare a modificare e perfezionare il modello per riprodurre al meglio i dati e comprendere la teoria che sta alla base. Il presente lavoro utilizza un potenziale ottico complesso detto potenziale di Woods-Saxon, un modello fenomenologico per studiare le sezioni d'urto per lo scattering elastico e di reazione degli antiprotoni su quattro diversi bersagli (carbonio-12, ossigeno-16, calcio-40 e piombo-208) a diverse quantità di moto del proiettile (tra 300 e $600\,\mathrm{MeV/c}$). Risolvendo l'equazione di Schrödinger, vengono calcolate le sezioni d'urto e successivamente vengono determinati i parametri del potenziale ottico di Woods-Saxon tramite il fitting ai dati sperimentali, utilizzando la minimizzazione del chi-quadro.

I risultati indicano che per i nuclei leggeri (come il carbonio e l'ossigeno) vi sono diversi valori dei parametri di intensità del potenziale rispetto a quelli dei nuclei medi e pesanti (come il calcio e il piombo). I parametri geometrici, che descrivono la forma dei nuclei, sono piuttosto simili tra i diversi fit. Tuttavia, le sezioni d'urto sembrano essere molto sensibili a questi parametri geometrici e sono fortemente correlate ai parametri di intensità del potenziale. Questi risultati, adottando alcune ipotesi semplificative, vengono utilizzati per fare previsioni a basse energie per lo scattering elastico degli antiprotoni. Queste previsioni mostrano che per futuri esperimenti il valore più basso di quantità di moto degli antiprotoni per effettuare misurazioni fattibili per lo studio delle interazioni nucleari è di $50\,\mathrm{MeV/c}$ ($E \sim 1.3\,\mathrm{MeV}$). Al di sotto di questo valore, il contributo dell'interazione nucleare è nascosto dalla dominante interazione coulombiana. Queste proiezioni possono essere preziose per progettare futuri esperimenti da svolgere in strutture dove si studia l'antimateria a bassa energia, come ELENA presso il Deceleratore di Antiprotoni al CERN (Ginevra) o FLAIR presso il GSI in Germania. Inoltre, i parametri di fitting vengono utilizzati per valutare il tempo di oscillazione antineutrone-neutrone, una grandezza utile per progettare esperimenti per lo studio di questo ipotetico fenomeno. I limiti inferiori per questo tempo sono in accordo con i risultati precedenti. L'osservazione dell'oscillazione antineutrone-neutrone è significativa per la comprensione dell'asimmetria materia-antimateria e della possibile non conservazione del numero barionico.

Questa analisi è un primo tentativo di costruire un modello nucleare singolo affidabile, i cui valori sono basati su fit a tutti i dati disponibili (sia lo scattering elastico che le reazioni). Per raggiungere ciò, sono necessari tutti i dati, che sfortunatamente non sono disponibili nei database online. Ulteriori analisi con alcune modifiche al modello utilizzato (includendo, ad esempio, la dipendenza dalla quantità di moto, lo studio dettagliato delle correlazioni dei parametri di fitting e diverse parametrizzazioni del modello...) sarebbero auspicabili per comprendere alcune discrepanze (ad esempio, l'anomalia osservata nelle sezioni d'urto degli antiprotoni e degli antineutroni), per investigare approfonditamente le interazioni a basse energie per l'antimateria e per fare previsioni per progettare nuovi esperimenti che possano gettare luce sull'interazione tra materia e antimateria a bassa energia.

Chapter 1

Introduction

1.1 Research context

During the 1980s and 1990s, the Low Energy Antiproton Ring (LEAR), at the European Council for Nuclear Research (CERN) laboratories in Geneve, emerged as a crucial facility for scientific exploration. It served as a testing ground for antinucleon annihilation and elastic scattering processes, particularly at energies below 50 MeV. This was a pioneering period, marked by a series of experiments that contributed immensely to our understanding of subatomic interactions.

These experiments, undertaken by numerous scientific teams, examined how antiprotons interacted with different atomic nuclei producing a wealth of data [1–16]. Their studies involved the meticulous measurement of cross sections and scattering patterns, providing valuable insights into the behavior of antinucleons at low energies. These findings paved the way for further exploration in the field of nuclear physics.

Further experimental exploration of low-energy antinucleon interaction was possible with the Antiproton Decelerator (AD) facility, which supplies different experiments of antiprotons at low energy. One of these experiments, the ASACUSA experiment, made a remarkable contribution to our understanding of antiproton interactions. The measurements of the collaboration were made with antiprotons with a momentum of 100 MeV/c, corresponding to the kinetic energy of 5.3 MeV [17–21]. These measurements involved intricate experimental setups and offered a comprehensive look at annihilation processes.

Furthermore, the ASACUSA collaboration extended their investigation to very low energies, as low as 125 keV [22]. This level of precision allows for the establishment of both upper and lower limits for annihilation cross section values. This work is pivotal, as it sheds light on the behavior of antiprotons at the extremely low-energy end, providing essential data points for understanding these interactions across a broad energy spectrum.

The antinucleon-nucleus interactions at low energies have profound implications for nuclear physics, including the detection of nuclear resonances and the determination of potential parameters that govern these interactions. The knowledge gained from these experiments can also be extrapolated to the broader context of cosmology, where the presence of antimatter in the universe remains a fascinating subject of study [23, 24]. These experiments serve as a valuable tool in testing hypotheses related to antimatter's existence and behavior in cosmic scenarios.

Beyond fundamental physics, low-energy antiproton interactions play a role in the study of cosmic rays, particularly those originating from outside Earth's atmosphere [25, 26]. These cosmic rays contain low-energy antiprotons, and understanding their behavior is crucial for space science and astrophysics. Moreover, the data is instrumental in the field of medical physics, where low-energy antiprotons are used for various medical applications, such as cancer treatment [27–29].

However, the data available nowadays are limited in energy and only a few and not totally accurate information can be extracted from these. Data on antiproton and antineutron scattering from different nuclei, in particular, are only for a quite narrow range of angles and energies. The most used approach to interpret these data and extrapolate information regarding the strong nuclear interaction and its attributes is the use of a phenomenological potential, which describes the interaction between the projectile and the nucleus in the framework of a Schödinger equation.

In many cases, the phenomenological potential is an *optical potential.* This model is based on the analogy with optics, where a complex refraction index is used to include both diffusive and absorptive phenomena [30]. The method of the optical potential has been used since the 1960s to calculate cross sections and to extrapolate information about the nuclei and the projectile-target interactions - in particular for the strong nuclear and electromagnetic forces [31]. The potential has different parameters, which can be tuned to reproduce the available data. Through a fitting procedure with experimental measurements, the values of these parameters are determined to give cross sections that follow data behavior. The physical interpretation of these parameters gives information about the interaction and its properties.

The parameter values obtained by the fitting procedure can be used to make predictions of the antinucleon-nucleus interaction at poorly explored energies, calculating the cross section for different processes that could occur at those energies [32, 33]. The study of these processes with the phenomenological potential could help to solve some open questions about antimatter that the present theories cannot explain completely due to mathematical and modeling limitations.

Recently, a new interest in the knowledge of antinucleon-nuclei cross sections has come back due to the interest in other possible measurements, *e.g.* antineutron-neutron oscillations [33, 34]. The discovery of antineutron-neutron oscillation is crucial in understanding the matter-antimatter asymmetry in the universe and whether the number of baryons could not be conserved, as requested by the Sakharov conditions [35]. The simplest way to do such calculations is still the optical potential approach, which apart from some problems with parameters ambiguity also continues to be successful in recent works [32, 36–38].

1.2 Objectives and structure of the thesis

The main objective of this work is to analyze data collected during the 1970s–1980s by LEAR experiments and, more recently, by other collaborations and laboratories, involving both antiprotons and antineutrons. The analysis employs the Woods-Saxon optical potential, which involves a variable number of parameters in the calculation of cross sections. Therefore, the analysis is aimed to find the optimal parameters that reproduce the current data available for differential elastic cross section (from now on just elastic cross section) and reaction cross section for antinucleons. Additionally, this work aims to project low- and very-low-energy cross sections for antiproton interactions with target nuclei. These projections can be valuable for designing future experiments to be conducted in low-energy antimatter facilities, such as ELENA at the Antiproton Decelerator at CERN (Geneva) or FLAIR at GSI in Germany.

The thesis is organized as follows. In Chapter 2 the theoretical background of the physical problem and the model used for the analysis are introduced; in particular, a focus on the literature review of previous studies of this kind is made. In Chapter 3 the used methodology is presented, describing the code used for the analysis and the fitting of the data. In Chapter 4 the main results of the analysis are shown and an interpretation of such results is presented. In Chapter 5 a deeper discussion of the analysis results is done and some projections at low-energy regimes are made. Moreover, an estimation of the antineutron-neutron oscillation time is done and briefly commented on. Chapter 6 concludes the work with a summary of the previous chapters and some comments on possible future developments of the current work and valuable applications in the design of future experiments.

Chapter 2

Phenomenological Foundations

2.1 Particle and antiparticle physics

The Standard Model of elementary particle (or simply Standard Model, from now on SM) describes two of the three fundamental interactions present in nature: the electroweak force and the strong nuclear one[1]. These interactions are represented as quantum fields which interact with the quantum particles through the exchange of mediator particles.

The properties and dynamics of quantum particles have been synthesized in the quantum field theory equations of the SM, each one describing a different kind of particle depending on its physical properties. The basic attributes of a quantum particle encompass spin, intrinsic parity, mass, and electrical charge. Particles with zero spin are governed by equations distinct from those of non-zero spin particles, with different consequences on their dynamics and interactions with other particles.

Each particle has its own *antiparticle partner* (or simply *antiparticle*), which is a particle with the same mass as the particle but with opposite quantum numbers (*e.g.* electric charge, leptonic number, baryonic number,...). This is valid both for fundamental particles (leptons and quarks) and composite particles (protons, neutrons,...). For composite particles, the difference stands in the valence quarks contribution, which are the quarks giving the main properties to the (anti)particle. For example, for nucleons, *i.e.* proton and neutron, since they are *hadrons* we have three valence quarks

$$p = \begin{pmatrix} u \\ u \\ d \end{pmatrix}, \quad n = \begin{pmatrix} u \\ d \\ d \end{pmatrix} \tag{2.1}$$

where u and d are the *up* and *down quarks*. For antinucleons, they are also hadrons, and being the antiparticle patterns of protons and neutrons their quarks contribution is

$$\overline{p} = \begin{pmatrix} \bar{u} \\ \bar{u} \\ \bar{d} \end{pmatrix}, \quad \overline{n} = \begin{pmatrix} \bar{u} \\ \bar{d} \\ \bar{d} \end{pmatrix} \tag{2.2}$$

---

[1] This is the more recent interpretation of the SM. Traditionally, there are three forces described: the electromagnetic one, the weak one, and the strong nuclear one. The electromagnetic and the weak nuclear interactions however were unified in the Weinberg-Salam theory. The gravitational interaction is not present in the SM.

where $\bar{u}$ and $\bar{d}$ are the up and down quarks' antiparticle partners, *i.e.* antiup and antidown.

The first antiparticle observed was the antielectron (or positron), revealed from cosmic rays in 1932 by Anderson [39], using a Wilson chamber in a magnetic field. Due to the opposite charge, he observed a different direction in the curvature of the trajectory with respect to the electron, and from the radius and the momentum of the particle he determined the mass which was the same as the electron. The antiproton was observed two decades later in 1955 by Chamberlain and Segrè [40]. As for the positron, the presence of the antiproton was anticipated by Dirac after the discovery of the positron. The year after the discovery of the antiproton, the antineutron was observed at the Bevatron [41].

Baryonic matter and antimatter can interact with each other via electromagnetic and nuclear processes. Like electrically charged particles, electrically charged antiparticles can be scattered from a nucleus of matter via Coulomb potential. Both electrically neutral and charged antiparticles can interact with the strong nuclear potential, which depends on their *baryonic properties* (*e.g.* baryonic number). The strong nuclear interaction at the nucleon level is the residue of the partons interactions, *i.e.* quarks and gluons. In first approximation, we can think of nucleon and antinucleon interactions as the exchange of pions, charged and neutral particles with a mass about 1/7 of the proton mass, by the framework of *quantum field theory*. This picture says that for each interaction there exists one or more *bosonic particle* (or simply *boson*), *i.e.* with integer-spin value, which mediates that interaction through its exchange. These are described by different sets of equations, depending on the value of their spin (*e.g.* zero spin particle: Klein-Gordon equation). Both nucleon and antinucleon, for example, are fermions since they are half-spin particles, and therefore they follow the *Fermi-Dirac statistics*.

Particles and antiparticles can also interact and *annihilate* each other, generating particles of different nature, respecting the conservation laws (*e.g.* conservation of momentum, energy, quantum numbers,...). For example, an electron annihilating with an anti-electron (more often called *positron*) can lead to two 511 keV photons in the case of a singlet initial configuration. Another example, more interesting for the present work, is the *antiproton-proton annihilation*, which generates in the final channels a different number of pions and kaons[2]. The measurements of the products of nucleon-antinucleon annihilation and the multiplicity of the charged and neutral pions are of relevance in the field of antimatter studies since can give some information about the structure of the hadrons and about the models used to describe them.

Particles and antiparticles are not completely symmetric since their difference can be observed through some processes that involve weak nuclear interaction. Since their masses are equal [42], they cannot be discriminated by spectrometry measurements, unless one considers the direction of the trajectory curvature in the magnetic field, since the two charges are opposite if we consider a charged particle. The lepton and baryon quantum numbers instead are opposite in value for the particle and

---

[2] The multiplicity of these mesons depends on the properties of the fundamental interaction between the partons that form the nucleons. This interaction is described by the theory of *quantum chromodynamics* (or *QCD*).

its antiparticle (*e.g.* electron has leptonic number +1 while positron has -1, and the proton has baryonic number +1 while antiproton -1). These quantum numbers govern the processes between particles and antiparticles following conservation laws derived from the fundamental physics symmetries.

Both particles and antiparticles are described by equations that have discrete symmetries, nominally *Charge Conjugation* (C), *Parity* (P), and *Time Reversal* (T) [43]. Charge Conjugation is the conversion of a particle into its antiparticle, inverting the sign of its internal quantum numbers (*e.g.* electric charge, baryon number, lepton number...). In many cases, this gives the antiparticle partner of the particle. Parity is the change in the sign of the spatial coordinates, which means a mirrored space. Time reversal reverses the direction of time in equations describing physical processes. C-symmetry implies that particles and antiparticles obey the same physical laws in processes. P-symmetry ensures the same behavior for left- and right-handed particles. T-symmetry gives the same physical results disregarding the direction in time of the process considered. The combined application of these symmetries, the so-called CPT-symmetry, is conserved in the SM. However C, P, and T symmetries are violated individually or when applied in pairs, depending on the interaction.

Among these internal symmetries, the Charge Conjugation and the Parity symmetries are maximally violated in weak nuclear interaction. As a consequence, particles and antiparticles behave differently in weak processes and they do not always exist in some chiral states (*e.g.* left- and right-handed particles and antiparticles). The combination of C and P, the CP-symmetry, is conserved in all the interactions, except for *weak interaction* where it is responsible, for example, for the particle-antiparticle oscillations that occur for neutral particles (*e.g.* neutral kaons) [43].

2.2 Antinucleon-nucleus interactions

As mentioned in the previous section, an antinucleon can interact via many different processes with matter. The main processes that an antinucleon can have with a nucleus are the same that can occur for a nucleon. These processes are:

- elastic scattering: $\bar{N} +^A_Z X \rightarrow \bar{N} +^A_Z X$
- inelastic scattering: $\bar{N} +^A_Z X \rightarrow \bar{N}' +^A_Z X^*$
- annihilation: $\bar{N} +^A_Z X \rightarrow B + C + \dots$
- charge exchange: $\bar{p} +^A_Z X \rightarrow \bar{n} +^A_{Z-1} Y$ or $\bar{n} +^A_Z X \rightarrow \bar{p} +^A_{Z+1} Y$
- knockout reaction: $\bar{N} +^A X \rightarrow \bar{N}' +^{A-A'} B +^{A'} C + \dots$

where $\bar{N} = (\bar{p}, \bar{n})$ are antinucleons, A is the mass number of the target nucleus X, and B, C, Y are other products of the possible reactions. The interactions we are interested in are the elastic scattering, where the total kinetic energy is conserved but the projectile deviates of a certain angle θ with respect to the initial direction, and the *reaction* processes, which in this work define all the processes where the projectile disappeared. The reaction process includes a variety of other processes, like annihilation and charge exchange, since in the final state the projectile is not present. The main process that can occur between the antinucleon and nucleon of the matter of materials is the annihilation, and therefore the disappearance of the original antinucleon. Therefore, antiprotons and antineutrons can survive only if isolated from matter, which is feasible for antiprotons using electromagnetic traps, but not trivial for antineutrons.

These processes are mediated by two interactions: the electromagnetic one and the strong nuclear one. The electromagnetic forces in the nucleus are well known and the Coulomb scattering is studied with high precision. It can also be quantified with nearly exact calculations obtaining an analytical expression for the cross section (see next chapter). The elastic scattering via strong nuclear force is more difficult to predict since calculations from first principles are quite complicated and require a great computational time. Some models for this residual strong force from interacting quarks "inside" the nucleus have been proposed over the decades, and recently other models added to the list. These models attempt to describe the *potential* of the nucleus from the known physical properties and to construct an effective interaction between the projectile and the target.

2.3 The optical potential approach

Due to the wave-particle duality, we can describe a particle as a wave with $k = 2\pi/\lambda_{dB}$, where $\lambda_{dB} = 2\pi\hbar/p$ is the de Broglie wavelength, which depends on the kinematics of the particle [44]. The scattering of a projectile particle from a target nucleus can be viewed in this frame as the diffraction of an incoming wave from an obstacle. The Copenhagen interpretation of quantum mechanics then affirms that the "intensity" of this wave is the density of probability to observe the projectile particle in a certain point of space.
We can think about a plane wave with wave number $\mathbf{k} = k\hat{z}$, where $\hat{z}$ is the direction of the wave along the z-axis, represented by the function $\psi(x) \propto e^{i\mathbf{k}\cdot\mathbf{r}} = e^{ikz}$. As shown in Figure 2.1, we can expect two main behaviors for this wave:

1. diffusion around the obstacle

2. absorption of part of the wave by the obstacle

The transmitted wave, passing through a semi-transparent mean, part is absorbed and part "distorted" by the interactions in the means. The net effect is the presence of a *phase shift* concerning the initial wave in the outgoing wave. The absorption reduces the amplitude of the outgoing waves.

As stated before, these are optics phenomena; however, due to wave-particle duality, we can find the same phenomena – with different properties – in the diffraction of a particle through an obstacle. We call them differently, *i.e.*

1. elastic scattering of the projectile particle

2. inelastic scattering or reaction of the projectile particle.

The analogy is also in the approach to make calculations of the main quantity for studying these phenomena, that is *cross section* σ. The cross section classically can be defined as the proportionality constant that relates the event rate of a process with a beam of particle A that scatters from target particles B giving the reaction

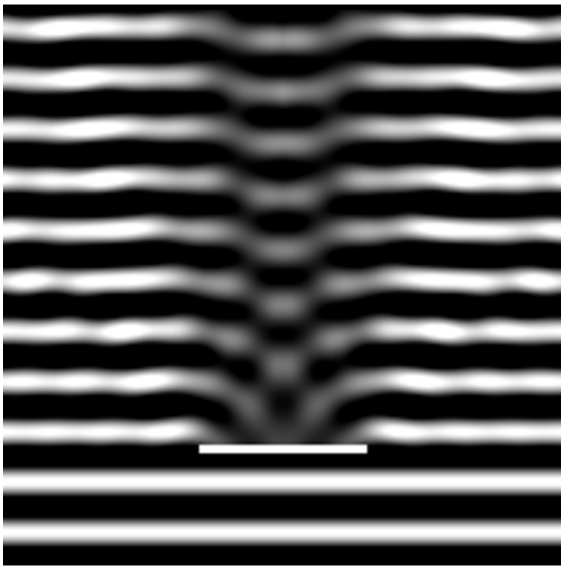

Figure 2.1: A simulation of diffraction (diffusion) phenomenon through an obstacle. The result is analog to the single-slit diffraction due to the *Babinet principle*.

$A + B \to X_1 + \cdots + X_n$. The reduction of the A beam intensity in the final state is given by

$$-dI = I_A N_B \sigma dx \tag{2.3}$$

where I_A is the initial intensity of the beam of particles A per unit area and time, N_B is the number of targets B per unit volume and dx is the thickness of the target. The cross section has the dimension of a surface and depends on the kinematic variables of the scattered particle. The total cross section of a reaction is usually defined as the sum of the elastic scattering cross section σ_{el} and all the inelastic (or reaction) processes cross sections σ_r [44]:

$$\sigma_{tot} = \sigma_{el} + \sigma_r. \tag{2.4}$$

Usually, for the elastic scattering, one is also interested in the distribution of this quantity with respect to the solid angle, $d\sigma_{el}/d\Omega$, where $d\Omega$ is the element of the solid angle where the particle passes through after being scattered if passed through the ring of surface $d\sigma$, as showed in Figure 2.2.

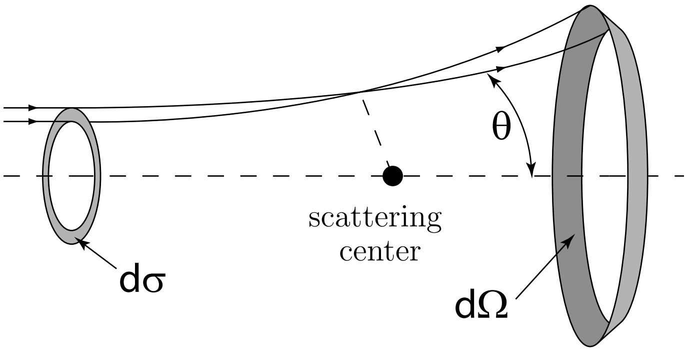

Figure 2.2: "Diagram of a scattering process", JabberWok, Wikimedia Commons, License: CC BY 3.0

In the presence of only elastic scattering, *e.g.* Coulomb scattering, we can represent the interaction between the projectile and the nucleus using a real potential, *e.g.* the Coulomb potential in the case of Coulomb scattering, as in optics we use a real refractive index to calculate the refraction and deviation in the mean. If we include absorption phenomena, we need a *complex* potential (or complex refractive index in case of optics) to consider the reduction of the "intensity" – *i.e.* of the square of the amplitude – which, in the case of quantum particles, is the probability of the non-absorptive processes. Adding an imaginary term (or more, depending on the model) introduces a reduction of the flux of the outgoing particles, obtaining the desired effect to represent absorption phenomena by the target.

To calculate the cross section, we need to solve the stationary states of the Schrödinger equation, which is

$$\left[\frac{\hbar^2\nabla^2}{2\mu} - V(r)\right]\psi(\mathbf{r}) = E\psi(\mathbf{r}) \tag{2.5}$$

where μ is the reduced mass of the system, ∇^2 is the *laplacian operator*, V is the potential and E is the energy of the system. Therefore, the potential V, to include absorption phenomena, takes the form

$$V(r) = V_R(r) + iV_I(r) \tag{2.6}$$

where V_R and V_I are real function of r. However, the effects of real and imaginary parts are not neatly separated. The real part contributes both to the elastic and inelastic scattering and the same is true for the imaginary part since the calculations are not perfectly linear and separated. Nonetheless, the reduction of the flux of particles is only due to the imaginary part. In fact, in the case of complex potential, the continuity equation becomes

$$\frac{\partial\rho}{\partial t} = \frac{i\hbar}{2\mu}\left[\psi^*\nabla^2\psi - \psi\nabla^2\psi^*\right] + \frac{i}{\hbar}\left(V - V^*\right)\rho \tag{2.7}$$

and since $V - V^* = 2iV_I$

$$\frac{\partial\rho}{\partial t} = \frac{i\hbar}{2\mu}\left[\psi^*\nabla^2\psi - \psi\nabla^2\psi^*\right] - \frac{2}{\hbar}V_I\rho \tag{2.8}$$

where $\rho = \psi^*\psi$. The term $-2V_I\rho/\hbar$ then reduces the amplitude of the wave function and depends only on the imaginary part of the potential V. In the determination of ψ, however, both V_R and V_I play a role (see Section 3.3.2 for explicit calculations).

Another important feature of the optical potential is the choice of its shape. There are many models of optical potential that describe the nucleus. All of them make some reasonable assumptions:

1. the potential must depend on the matter density distribution in the nucleus
2. the shape must take into account a "smoothed" surface

The first assumption is due to the dependence of strong force with the presence of nucleons in the nucleus: the greater the number of nucleons, the greater the strong interactions exchanges between them. The distribution of matter inside a nucleus has been measured and to model it, usually the *Fermi function* is used:

$$f(r) = \frac{1}{1 + \exp\left(\dfrac{r - r_0}{a_0}\right)} \tag{2.9}$$

where r is the radial coordinate (in spherical approximation), r_0 is the nuclear radius and a_0 is the diffuseness – *i.e.* the “surface thickness” – of the nucleus surface. The r_0 parameter is usually parametrized as $r_0 \to r_0 A^{\frac{1}{3}}$, where A is the atomic weight of the nucleus in amu units. This shape can vary to adapt more accurately to the measurements, introducing correction factors.

The second assumption, satisfied by Equation 2.9, is due to observations. Using a non-smooth surface shape, *e.g.* square-well, the annihilation rate is underestimated, since this process occurs mainly on the surface of the nucleus. Therefore, it is necessary to take into account this diffuseness of the surface. Another shape for the form factor of the nucleus that satisfies these requirements is for example the Gaussian, used frequently for these studies and usually requires at least one parameter less than the Fermi function since

$$f(r) = \exp\left(-\frac{r^2}{a_0^2}\right). \tag{2.10}$$

In the most general case, this shape can be chosen differently for the real and imaginary parts.

2.4 Scattering data analysis with the optical potentials

2.4.1 Optical models in N–A scattering experiments

The first applications of the optical potential model date back to 1935[3], from a proposal by Bethe and other colleagues that wanted to study nuclear reactions and slow neutron resonances using a complex potential well. Even if this strategy was a failure in this field, after World War II, with the beginning of the high-energy experiments era, the optical model started to spread for the analysis of nuclear data. The first documented use of a similar approach was by Fernbach, Serber & Taylor in 1949, using instead of an optical potential a complex index of refraction. From this index, they could calculate the mean free path and the diffraction scattering at small angles. An application in a low-energy regime was performed during the 1950s when the nuclear shell model was developing and succeeded in the physics community, demonstrating that the nuclear matter is not highly absorptive, contrary to what Bethe assumed initially in the 1930s. The first model used in these cases was a complex square well applied to proton elastic scattering data at 18 MeV by LeLevier and Saxon in 1952; in the same year, Barschall *et al.* applied the optical model in an experiment, confirming the possibility to use it also at low-energies. However, the complex square well was not the final solution, since it underestimated the reaction cross section, due to the higher reflection rate than the observed one. That problem was solved by introducing potential shapes with a tapered surface, and Woods and Saxon, in 1954, applied for the first time the potential with the shape that takes their name:

$$V_{\mathrm{WS}}(r) = -\left(V_0 + iW_0\right)\left[1 + \exp\left(\frac{r-R}{a}\right)\right]^{-1} \tag{2.11}$$

---

[3] All the historical information about the use of the optical potential are taken from Ref. [30].

where V_0 and W_0 are the real and imaginary strength potential parameters, *i.e.* the potential-well depth for the non-absorptive and absorptive terms. Using this potential, they obtained good fits in this and future data analyses. From that time, the Woods-Saxon shape has been the most used phenomenological potential shape for optical potential models in these kinds of analyses.

The optical potential approach has been used in the decades after for many different nuclear species, obtaining successful fits and predictions for some phenomena[4]. More terms were added to take into account other features of the nuclear processes, like the absorption at the surface. In particular, the most used potential – without considering the spin-orbital terms – is the following:

$$-V_{\mathrm{WS}} = V_0 f(r, R, a) + iW_0 f(r, R', a') + iW_{0\mathrm{D}} g(r, R', a') \tag{2.12}$$

where

$$f(r, R, a) = \left[1 + \exp\left(\frac{r-R}{a}\right)\right]^{-1} \tag{2.13}$$

$$g(r, R, a) = -4a\frac{df(r, R, a)}{dr}. \tag{2.14}$$

and $W_{0\mathrm{D}}$ is the surface absorption term, which represents the absorption phenomena that can occur on the surface of the nucleus (*i.e.* annihilation). The functions f and g are represented in Figure 2.3 as functions of the radial distance r, expressed in femtometers, for fixed parameter values.

The surface term has a peak at $r = R$, which is the middle point of the nuclear surface width. As stated before, this term is useful to represent phenomena that take place mainly at the surface of the nucleus (*e.g.* absorption and annihilation). With this model, many analyses have been done through decades, from the 1960s to 1990s and beyond, using one-particle projectile (like nucleons) but also composite projectile (*e.g.* alpha particles). However, it is not the only optical model used. There are other models with different parametrization and assumptions, some using available data to assess the geometrical values of the nucleus (*e.g.* folding models) or that start from the first principles (*e.g.* microscopic models). These models are more adequate for studying the nucleus structure, making them more valuable for comprehending and forecasting energy levels and other characteristics within the nucleus.

Similar models are sometimes used with a different parametrization based on the use of atomic data to estimate some parameters. An example of a recently and frequently used one is the model by Batty *et al.* [32]:

$$-V(r) = \frac{2\pi\hbar c}{\mu}\left(1 + \frac{\mu}{m_{\mathrm{p}}}\right)(a + ib)\rho(r) \tag{2.15}$$

where μ is the reduced mass of the projectile-target system, m_{p} is the mass of the projectile, $a + ib$ is the parametrization of the *scattering length* and ρ is the *matter density distribution* of the nucleus – usually a Woods-Saxon shape. This parametrization has some advantages. First of all, it depends directly on the scattering length which is an important quantity to be determined (see the next section).

---

[4] We stress here that we are talking about a phenomenological model and it does not say anything about the internal structure of the nucleus, which is the role of the shell model of strong force.

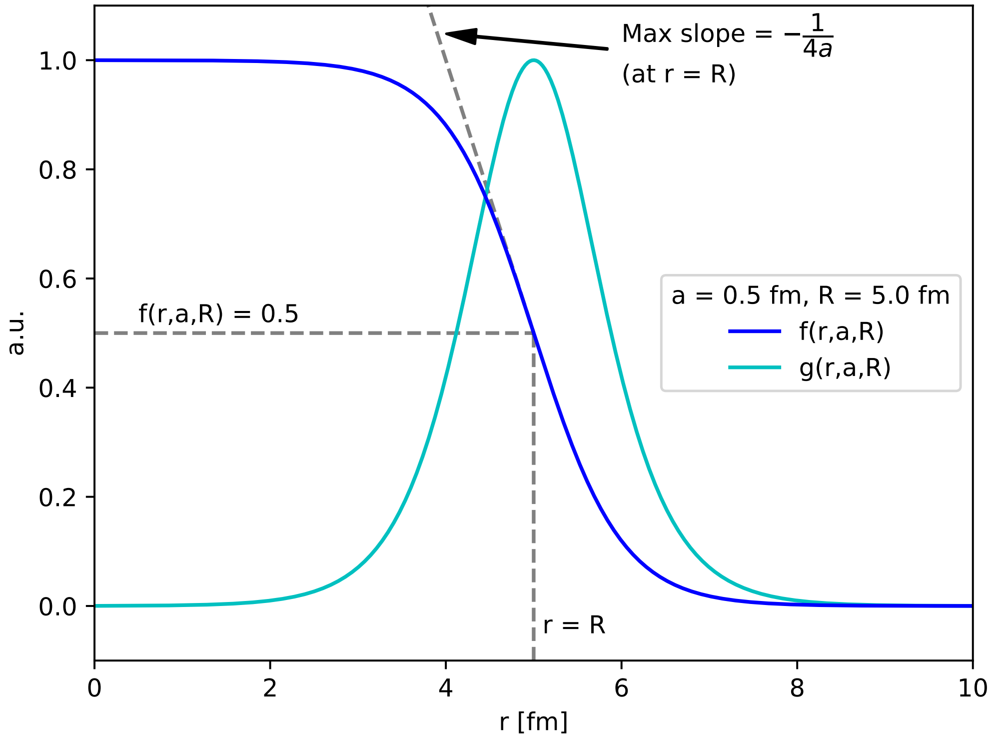

Figure 2.3: The Woods-Saxon shape f and its normalized derivative g defined in Equations 2.13 and 2.14 in function of the radial distance r. The geometrical parameters are fixed at values $a = 0.5\,\text{fm}$ and $R = 5\,\text{fm}$. The annotation on the slope is inserted to better understand the meaning of the parameter a.

Secondly, the density distribution ρ can be modified to take into account the nucleus content of neutrons and protons. However, we will not use this parametrization since we focused on the different models described in the next chapter.

2.4.2 $\bar{\text{N}}$–A scattering and annihilation

With the beginning of low-energy experiments with antinucleons, mainly thanks to the LEAR facility, the optical potential was also used to analyse the scattering of antiprotons and antineutrons on the target nuclei. The models in fact can be applied independently from the nature of the projectile – both proton and antiproton are fermions and the only difference in this model is the electric charge which only plays a role in the electromagnetic interaction and not in the strong nuclear one. Since the possible reactions and phenomena with antinucleons are different with respect to the ones with nucleons (*e.g.* annihilation), the values of the parameters in the optical potentials change between nucleons and antinucleons to describe the possible different processes. In particular, we can expect the imaginary part to be higher in values than in the experiment of scattering with nucleons, where the absorption phenomena are limited.

In the 1980s experiments at LEAR performed measurements on elastic scattering and reactions for antiprotons with nuclei of different atomic weights. During the period 1984–1986, numerous analyses of these data were published. The most important for our study are those by Garreta *et al.* [45, 46], by Heiselberg *et al.* [47], and by Janouin *et al.* [48]. The data analysed in their papers come actually from the same experiment, PS209.

In the first analysis, Garreta *et al.* analysed differential cross section of elastic scattering of 180 MeV antiproton with three different targets, *i.e.* carbon-12, calcium-40, and lead-208. They used the Woods-Saxon shape (in the article appeared with the name *Dover-Richard model*) with different parameters for real and imaginary parts:

$$-V_{\mathrm{DR}} = \frac{V_0}{1+\exp\left(\dfrac{r-r_{0\mathrm{V}}A^{1/3}}{a_{\mathrm{V}}}\right)} + \frac{iW_0}{1+\exp\left(\dfrac{r-r_{0\mathrm{W}}A^{1/3}}{a_{\mathrm{W}}}\right)}. \tag{2.16}$$

They compared this optical model with another model, obtaining a better fitting to data with the former. The values obtained for these parameters are quite different from the ones obtained for nucleon-nucleus scattering. They obtained that $W_0 > 2\,V_0$. Their best-fit parameter values are summarized in Table 2.1. This work concluded that the potential strength is well determined at the surface of the nucleus (*i.e.* $r = r_{0\mathrm{W}}A^{1/3}$). The results are comparable to the ones obtained by microscopic models with good fit results ($0.8 < \chi^2/n_{\mathrm{dof}} < 1.5$). Therefore, the optical model works quite properly with the scattering data and gives also a good prediction for the values of the reaction cross section in the momentum region analysed ($p \sim$ 600 MeV/c).

Target	V_0 [MeV]	W_0 [MeV]	r_{0V} [fm]	r_{0W} [fm]	a_V [fm]	a_W [fm]
^{12}C	30	118	1.225	1.1	0.514	0.500
^{40}Ca	30	124	1.225	1.1	0.572	0.590
^{208}Pb	30	172	1.225	1.1	0.672	0.649

Table 2.1: The best values for parameters in Garreta *et al.* (1984).

Heiselberg *et al.* and Janouin *et al.* analysed quite the same data from 300 MeV/c and 600 MeV of the same experiment and used similar methods for the analysis. The latter added to the analysis also two other targets, namely oxygen-16 and oxygen-18. They both described the procedure of fitting in a detailed manner; however, they used different codes (respectively `DWUCK` and `ECIS`) for the calculations, both standards in the field of research. The interesting aspect of these two analyses is that we can compare two similar methods used on the same data. They both used the minimization of the following χ^2:

$$\chi^2 = \min_{\lambda\in[0.9,1.1]} \sum_{i=1}^{N} \frac{\left[\lambda\sigma(\theta_i) - \sigma_x(\theta_i)\right]^2}{\left[(\Delta\sigma_i)^2 + \left(\dfrac{d\sigma(\theta)}{d\theta}\dfrac{\sigma_x(\theta_i)}{\sigma(\theta_i)}\Delta\theta\right)^2\right]} \tag{2.17}$$

where σ_xs are the experimental values of the differential elastic scattering cross sections at the angle θ_i, and $\Delta\theta = 0.2°$ is the error on the angle measurements, while λ is the normalization factor. The theoretical prediction σ is defined as:

$$\begin{gathered}\sigma(\theta)=\frac{1}{3}\left[\sigma_0(\theta)+\sigma_0(\theta+\delta\theta)+\sigma_0(\theta-\delta\theta)\right]\\ \delta\theta=\frac{1}{2}\sqrt{\frac{1}{2}}\alpha\end{gathered}\tag{2.18}$$

where σ_0 is the differential cross section from calculations and α is the *effective angular opening* of the experiment[5]. In the case of Janouin *et al.* analysis, the χ^2 add an explicit *pull term* for the λ parameter, which appears in the last parenthesis of the formula:

$$\chi^2=\min_{\lambda}\sum_{i=1}^{N}\frac{\left[\lambda\sigma(\theta_i)-\sigma_x(\theta_i)\right]^2}{\left[(\Delta\sigma_i)^2+\left(\frac{d\sigma(\theta)}{d\theta}\frac{\sigma_x(\theta_i)}{\sigma(\theta_i)}\Delta\theta\right)^2\right]}+\left(\frac{\lambda-\lambda_0}{\Delta\lambda}\right)^2\tag{2.19}$$

where $\lambda_0=1.0$ and $\Delta\lambda=0.1$ so that its value is constrained in the interval 1.0 ± 0.1. The parameters' values of their best fits are reported in Tables 2.2.

p_{cm} [MeV/c]	Target	V_0 [MeV]	W_0 [MeV]	r_{0V} [fm]	r_{0W} [fm]	a_V [fm]	a_W [fm]	λ	$\tilde{\chi}^2$	
300.0	^{12}C	18	109	1.36	1.10	0.59	0.50	0.96	0.61	H
		25	61	1.22	1.17	0.56	—	1.0	0.70	J
303.3	^{40}Ca	40	100	1.10	1.10	0.60	0.60	1.01	0.72	H
		9	143	1.4	1.03	0.63	—	1.0	0.68	J
304.9	^{208}Pb	20	140	1.10	1.10	0.65	0.65	0.96	0.54	H
		0.0	22	—	1.38	0.50	—	1.0	0.58	J
607.9	^{12}C	20	113	1.35	1.10	0.44	0.50	0.93	0.91	H
		44	184	1.05	0.935	0.56	—	1.0	0.86	J
608.0	^{40}Ca	16	123	1.34	1.10	0.50	0.60	0.92	0.52	H
		40.5	111	1.1	1.1	0.63	—	1.05	0.63	J
609.0	^{208}Pb	14	272	1.34	1.05	0.47	0.65	0.92	0.91	H
		60	105	1.097	1.13	0.70	—	1.0	1.07	J

Table 2.2: The best values for parameters in Heiselberg *et al.* (H) and Janouin *et al.* (J). The reduced χ^2 is defined as $\tilde{\chi}^2=\chi^2/n_{\mathrm{dof}}$, where n_{dof} is the number of degrees of freedom ($n_{\mathrm{data}}-n_{\text{free-params}}$). For Janouin results we reported the diffuseness a as a_V since $a_V=a_W=a$.

In the case of Janouin *et al.*, the real and imaginary diffuseness are imposed to be equal, while the real and imaginary radii are kept different. However, one can notice that in the majority of cases, the values for a_{V} and a_{W} are similar and not afar. Hence, the Janouin *et al.* assumption of imposing $a_V=a_W$ can be considered appropriate, which also allows us to reduce the number of free parameters and the ambiguity in their determination. The strength parameter values are quite

---

[5] Neither the papers which use this formula nor the original paper with the information about the experiment and these data report the value for α.

different in the two analyses, in particular for ^{208}Pb. Unfortunately, no detail about the algorithm used for the fitting procedure or other code-related comments are present in the papers, and therefore we have no clue about what this difference – apart from the typical ambiguity for this model in the search of the values – is due to. The analysis of Janouin *et al.* is particularly important since they deeply investigated many aspects of the potential, considering also the correlations among the parameters, the continuous-parameters ambiguity (see Section 2.5), and the dependence on energy of the parameters. In their meticulous analysis, they found confirmation for what has been found in the previous analyses, plus some interesting relations. In particular, they found a slight dependence of the diffuseness both on $A^{1/3}$ and on the unbalance of neutron and proton in the nucleus. This allows in principle to reduce the number of free parameters and to better determine their values. They showed that using the same values for V_0, W_0 and $r_{0\mathrm{V}} = r_{0\mathrm{W}}$ for all the targets with antiproton at a certain momentum, calculating the diffuseness with the relations found, the fits are quite good ($\tilde{\chi}^2 < 3.0$).

All the analyses mentioned before, in addition to the differential elastic scattering cross sections, considered also the evaluation of the reaction cross sections. The *"black disk" model* was used with the inclusion of the diffuseness in the formula:

$$\sigma_r = \pi \left(r_0 A^{1/3} + a \right)^2 \tag{2.20}$$

where a is the diffuseness parameter of the nucleus. In all the analyses these parameters have similar values (*e.g.* at 180 MeV, $r_0 \sim 1.5\,\mathrm{fm}$ and $a \sim 0.65\,\mathrm{fm}$) and accurately reproduce the data and previous predictions . No calculation has been performed with the same optical potential and with partial-wave formalism for the elastic scattering cross section.

The interest in reaction and annihilation processes has recently grown in research, and the necessity to analyse directly new and updated data increased with it. The most recent data available nowadays has been taken from experiments in the facility of low energy antimatter, such as the Antiproton Decelerator (AD) at CERN, the heir of LEAR. An analysis with a possible unique model which is a reparametrization of optical potential similar to Equation 2.15 was made by Batty *et al.* [32]. They directly analysed the reaction data, extrapolating also useful information about the scattering length of the antiproton in some light targets. These results were also compared with another "black disk" model, dependent on the momentum of the projectile:

$$\sigma_R = \pi R^2 \left(1 + \frac{2mZe^2}{\hbar^2 k_L k R} \right)^2 \tag{2.21}$$

where R is the nuclear radius, e is the elementary charge, m is the projectile mass, Z is the number of proton in the nucleus and k_L and k are respectively the projectile wave numbers in the laboratory and center-of-mass frames.

In this same direction worked Lee & Wong [36], who in 2018 analysed the antineutron annihilation data on different nuclear species (including ^{12}C and ^{208}Pb).

A slightly different parametrization of the optical model was used:

$$-V_{\mathrm{opt}}(r) = V_V(r,p) + i\left[W_V(r,p) + W_{\mathrm{D}}(r,p)\right] \tag{2.22}$$

$$V_V(r,p) = V_0(p) f(r, r_V, a_V) \tag{2.23}$$

$$W_V(r,p) = W_0(p) f(r, r_W, a_W) \tag{2.24}$$

$$W_{\mathrm{D}}(r,p) = -4 a_W W_{0\mathrm{D}}(p) \frac{d}{dr} f(r, r_{W_{\mathrm{D}}}, a_{W_{\mathrm{D}}}) \tag{2.25}$$

$$f(r, r_x, a_x) = \left[1 + \exp\left\{\left(\frac{r - r_x}{a_x}\right)\right\}\right]^{-1}, \quad x = \{V, W, W_{\mathrm{D}}\}. \tag{2.26}$$

Here the surface term W_{D} is different from zero in general, and one can notice that the strength parameters V_0, W_0 and $W_{0\mathrm{D}}$ are momentum-dependent to take into account the difference in behavior at high and low energies. The form of momentum dependence on the real potential is the following:

$$V_0(p_{\mathrm{lab}}) = V_0' \cdot \left(\frac{\cosh\left(\sqrt{b_0 + p_{\mathrm{lab}}} - \sqrt{b_0}\right)}{\cosh\left(\sqrt{b_1 + p_{\mathrm{lab}}} - \sqrt{b_1}\right)}\right) \tag{2.27}$$

where V_0' is a momentum-independent potential strength parameter, and b_0 and b_1 are adjustable parameters. The formula 2.27 was chosen to have $V_0 \to V_0'$ for $p_{\mathrm{lab}} \to 0$. The only free-parameters used here are V_0', W_0, $W_{0\mathrm{D}}$, b_0 and b_1. The radius and diffuseness were estimated from the approximation

$$\sigma_{\mathrm{ann}} = \pi \left(r_R A^{1/3}\right)^2 \tag{2.28}$$

and related to the r_V and a_V of the optical model through

$$r_V = r_R \left[1 - \frac{1}{3}\left(\frac{\pi a_V}{r_R A^{1/3}}\right)^2\right]. \tag{2.29}$$

assuming the real and imaginary geometrical parameters of the volume terms are equal in values[6]. The results of this complex parameters estimation can be found in Ref. [36]. The important result is that this model seems to work quite well both for antineutron and antiproton annihilation cross sections (see Figure 1 of the same reference).

There is a notable effect in the reaction cross sections of antinucleons. It is expected that negatively charged particles (*i.e.* antiprotons) are focused on the nucleus, due to the Coulomb attraction. As a consequence, the annihilation rate at low energies should be increased for antiprotons with respect to antineutrons. However, in the data, this enhancement is not observed or at least less evident than expected. It should be highlighted that in their work the introduction of a momentum-dependent parameter plays an important role.

2.5 Continuous-parameters ambiguity

It was already observed in the analysis of α–N scattering that, once the shape of the potential is chosen, the optical potential strengths (V and W) give good agreement

---

[6] No information about the estimation of the geometrical parameters of the surface absorption term are given in the paper.

with data for many different values. The same was observed by Wong *et al.* [49] and Kubo *et al.* [50] during the first experiments about antiproton scattering. The former study was done before the LEAR data release and based solely on $\bar{p}$-atom data for x-ray transition to the lowest atomic state. The energy shift and the widths of the transitions can be calculated from an optical model. They supposed the usual Woods-Saxon shape including a parameter, w, which considers the electron scattering

$$-V_{\text{opt}} = V_0 \frac{1 + w \cdot (r/R)^2}{1 + \exp\left(\dfrac{r-R}{a_V}\right)} + iW_0 \frac{1 + w \cdot (r/R)^2}{1 + \exp\left(\dfrac{r-R}{a_W}\right)}. \tag{2.30}$$

Wong *et al.* concluded that two kinds of potential exist: the S (deep real and shallow imaginary part) and the D (deep imaginary and shallow real part). Both could represent $\bar{p}$-atom data correctly – considering also that some of the measurements were not precise, with large errors. However, they have different consequences on the elastic scattering predictions at large angles and also in the estimation of the $\bar{n} - n$ oscillation time $\tau_{\bar{n}n}$, which is related to the optical potential through [49]

$$\tau_A = \tau_{\bar{n}n}^2 \frac{\left(V_{\bar{n}} - V_n\right)^2 + W_{\bar{n}}^2}{2\hbar W_{\bar{n}}} \tag{2.31}$$

where τ_A is the *neutron effective mean lifetime* in the nuclear matter for annihilation, $V_{\bar{n}}$ and $W_{\bar{n}}$ are the real and imaginary strengths parameters of the optical potential for antineutron and V_n is the real strength parameter for neutron. Therefore, the kind of potential determines different estimations for this quantity, which is of extreme importance nowadays for future experiments on this extremely rare phenomenon. They pointed out also the possibility that the next-to-be-released measurements by LEAR could enlighten about which family of potentials could describe both the energy shifts and widths in x-ray emission and the scattering data.

The study by Kubo *et al.* the following year (1984), when the LEAR data were published, went in this direction. They assumed the same shape for potential – the Woods-Saxon one, *i.e.* proportional to nuclear matter density distribution in the nucleus – which was fitted to the available data. They found that for a wide range of different values, the differential elastic scattering cross section for ^{12}C at 46.8 MeV/c was the same for all the range 0°-180°. They also considered the deformation of the ^{12}C nucleus in their calculations. Moreover, they used the *eikonal approximation* to estimate the *absorption radius*, *i.e.* the radius for which

$$\left|\exp\left[X\left(R_{\text{abs}}\right)\right]\right| = \frac{1}{2} \tag{2.32}$$

where

$$X(b) = i \int_{-\infty}^{+\infty} dz \left[K(\rho(r)) - k\right] \tag{2.33}$$

$$\frac{K^2(\rho)}{k^2} = 1 + \frac{4\pi}{k^2} \rho(r) f(0) \tag{2.34}$$

where $\rho(r)$ is the nuclear matter density at r, $f(0)$ is the scattering amplitude in the laboratory frame at $\theta = 0$ and k is the wave number in the laboratory frame (for the antiproton). This calculation lead to $R_{\text{abs}} = 3.7\,\text{fm}$ using the values of Ref. [50]. They concluded that this radius, being larger than the radius of half-density c, *i.e.*

$\rho(c) = \rho_0/2$ – equivalent to R in the Woods-Saxon model –, the elastic and inelastic scattering are sensible to the structure of the nucleus only at a large distance.

Both these studies, and successive too, confirmed that there is more than one possible set of values for the continuous parameters of the Woods-Saxon shape for optical potential.

2.6 Summary

We have seen the physics underlying the antinucleon-nucleus interactions for what concerns the strong nuclear force. Antimatter and matter interact with each other both through matter-like processes (*e.g.* elastic and inelastic scattering) and unique phenomena (*e.g.* annihilation). To model these interactions, many tries have been done – and also nowadays are done – and the most used and most successful method is the use of an *optical potential* for the calculation in partial-wave formalism (explained in detail in the next chapter).

We showed that using a complex potential proportional to the nuclear matter density distribution, nominally a *Woods-Saxon shape*, many analyses found good agreement with available data. Being a phenomenological model, the parameters are calculated with a fitting procedure and not calculated from first principles. Some attempts to extract such parameters from other data, *e.g.* $\bar{p}$-atom x-ray emission, have been made. However, not all of them can be estimated with this method, and some parameters must be free. There are no unique combinations of such parameters since different values for these can lead to equally good fits.

Chapter 3

Methodology

The main objective of this work is to determine in the most precise way the parameters of an optical potential to reproduce experimental data. In this chapter, we elucidate the choices of data, the analysed targets, the optical model used, and all the methods we applied to achieve the results obtained and which are shown in Chapter 4.

3.1 Data collection of scattering and annihilation

For the determination of the optical potential parameters, we use different available data for antiprotons. The data are the following:

- Antiproton elastic scattering: the final state of the process has the same initial particles (nucleus and projectile)
  - Differential cross sections of elastic scattering for ^{12}C, ^{40}Ca and ^{208}Pb at around 300 and 600 MeV/c (Ref.s [45, 46, 48])
  - Differential cross sections of elastic scattering for ^{16}O and ^{18}O at around 600 MeV/c (Ref. [48])
- Antiproton reaction: the projectile in the final state disappears
  - Reaction cross section for ^{12}C from 100 to 500 MeV/c (Ref.s [18])
  - Reaction cross section for ^{40}Ca at around 600 MeV/c (Ref. [45])
  - Reaction cross section for ^{208}Pb from 500 to 650 MeV/c (Ref. [45, 51]

These data were collected by many different experiments from the 1970s and 1990s. Mainly, these are data from the experiments at the Low Energy Antiproton Ring (LEAR). The LEAR facility was an antiproton accelerator that permitted the exploration of the low-energy region of the antiproton processes. The experiments around this accelerator discovered many mesonic resonances and performed measurements about antiproton properties and interactions, obtaining the most accurate results also used nowadays. More recently, other experiments made new measurements, mainly on the reaction cross section of antiproton and nuclei, *e.g.* ASACUSA at the Antiproton Decelerator (AD).

The data listed above are not present in the form of tables, or many of them were lost during the years due to private communications as the main interchange method.

Due to the absence of precise values tabled properly, we had to extract the data from the existing plot in the original articles, using the online tool `WebPlotDigitizer` [52]. This software allows the extraction of data from images, calibrating the axes of a plot, and obtaining an accurate coordinates system. However, the selection of the points on the calibrated image is manual and the error bars are not implemented in this extraction. This means that in the extraction of the data we introduce a little error due to the user's precision in pointing correctly the data. This is not trivial in some cases, since the ink of the digitized plot is not uniform and sometimes points are "blurred" and overlaid. Regarding the error bars of the cross section data, we wrote a simple script to calculate them starting from a text file containing the data points collected from `WebPlotDigitizer` and considering some additional points indicating the upper extreme of the error bars and supposing the error bars are symmetric. In the majority of data, the errors on the angles or the momenta are ignored in the representation of data, and therefore we have not considered them in our analysis either.

We are interested in particular in the case of ^{12}C. For this target, we have a quite large amount of data in a wide region of angles or momenta. We also have both reaction and elastic cross section data, and both for antiproton and antineutrons (in the case of reaction cross sections). In addition, we have data for different momenta for ^{12}C (300, 466, 542 and 608 MeV/c). We also focus on ^{40}Ca and ^{208}Pb because they are the most used in the previous analyses and therefore we can make useful comparisons concerning these analyses and understand the differences in the results obtained.

3.2 The Woods-Saxon optical potential

As discussed in Chapter 2, many optical potentials have been proposed over the years, depending on the analysis the work was focused on. However, some characteristics have been consolidated during the decades. For example, the need for a smooth surface to account for the annihilation process that a square-well potential underestimates. Microscopic optical potential relies on some experimental measurements to extrapolate some parameter values, reducing the number of free parameters needed; phenomenological optical potential instead has more free parameters and usually has a simple parameterization. Our choice falls on the phenomenological potential and more precisely on the *Woods-Saxon optical potential* (from now on *WSOP* or *WS*). The WSOP, in its general form, can be written as follows:

$$\begin{aligned} -U_{\text{WS}} &= V_0\mathcal{F}(r|\mathbf{\Lambda}_R) + iW_0\mathcal{F}((r|\mathbf{\Lambda}_I) + && \text{Volume terms} \\ &\quad +V_{0\text{D}}\,\mathcal{G}(r|\mathbf{\Lambda}_R) + iW_{0\text{D}}\,\mathcal{G}(r|\mathbf{\Lambda}_I) + && \text{Surface terms} \\ &\quad + \left[V_{0,\text{LS}}\,\mathcal{G}(r|\mathbf{\Lambda}_R) + iW_{0,\text{LS}}\,\mathcal{G}(r|\mathbf{\Lambda}_I)\right](\mathbf{L}\cdot\mathbf{S}) && \text{Spin-orbit terms} \end{aligned} \tag{3.1}$$

where

$$\mathcal{F}(r|\mathbf{\Lambda}_x) = \left[1 + \exp\left(\frac{r - r_{0x}}{a_{0x}}\right)\right]^{-1} \tag{3.2}$$

$$\mathcal{G}(r|\mathbf{\Lambda}_x) = 4a_{0x}\frac{d\mathcal{F}(r|\mathbf{\Lambda}_x)}{dr} \tag{3.3}$$

$\mathbf{\Lambda}_x = (r_{0x}, a_{0x})$ are the geometrical parameters of the optical potential for the real ($x = R$) and imaginary ($x = I$) parts. V_0 and W_0 are, respectively, the real and imaginary *strengths* of the volume terms of the potential, *i.e.* the depth of the "well"; $V_{0\mathrm{D}}$ and $W_{0\mathrm{D}}$ are the real and imaginary *surface strengths*, while V_{LS} and W_{LS} are the real and imaginary *spin-orbit couplings* and $\mathbf{L}$ and $\mathbf{S}$ are the orbital and spin angular momentum operators of the projectile particle. The function $\mathcal{F}$ in Equation 3.2 is the *Woods-Saxon function* that describes the shape of the potential generated by the nucleus and the matter density distribution of it. Each term of this potential has 6 parameters: 2 strengths (V_0, W_0) and 4 geometrical parameters (r_0, a_0 for both real and imaginary parts). If we consider the general form of the Woods-Saxon optical potential, we have a total of 18 free parameters. In practice, there is no need for all the terms present in the general form. In our specific case, we can rid of the spin-orbit terms, since we are not interested in measurements of the final spin state and we calculate the unpolarized cross sections. As mentioned by [31], efforts to distinguish between surface and volume absorption potentials showed negligible practical differences when parameters were optimized to fit experimental data, suggesting their equal efficacy. Moreover, as highlighted in [53], for projectile energies above 10 MeV the surface absorption is less probable, and around 100 MeV the volume term is more adequate to reproduce data. Therefore, we have a total of 6 free parameters (considering different geometrical parameters for the real and imaginary part) for the case of antiproton-nuclei unpolarized cross section calculation. There is also an additional parameter that we have to consider in the fitting procedure, a *normalization* parameter (we discuss it in the next section).

3.3 Implementation of the theoretical model and the fit procedure

The code used for the analysis is a 1990s software written in `FORTRAN77` and developed by more people during the years, derived from a main code called `THREEDEE` by Chant and Roos [54]. This code had no documentation available online since it is a mixture of different codes and it has been used for many analyses during the 1990s. Retrieving its operation in detail required a quite great amount of time, and some parts of the codes were not properly commented on. However, the general operation is clear and the procedure used for the calculation of the cross section is well known.

The code uses the *partial-wave approach* for the calculation of both the reaction and elastic cross sections, and solving the non-relativistic Schrödinger equation with the use of the *Numerov-Fox-Goodwin method.*

3.3.1 The partial-wave formalism

To calculate the cross sections, we must solve the time-independent Schrödinger equation:

$$\left(\frac{\hbar^2\nabla^2}{2\mu} - U_{\mathrm{WS}}(r) - U_{\mathrm{C}}(r)\right)\psi(\mathbf{r}) = -E\psi(\mathbf{r}) \tag{3.4}$$

where μ is the *reduced mass* of the system, and U_{WS} and U_{C} are respectively the Woods-Saxon potential (defined in the previous section in Equation 3.1) and the

Coulomb potential of a distributed charge:

$$U_{\mathrm{C}}(r) = \begin{cases} \dfrac{Z_t Z_p e^2}{2R_C}\left(3 - \dfrac{r^2}{R_C^2}\right), & r \leq R_C \\ \dfrac{Z_t Z_p e^2}{r}, & r > R_C. \end{cases} \tag{3.5}$$

where Z_t and Z_p are respectively the target and projectile charge expressed in units of elementary charge, e (in the antiproton case $Z_p = -1$) and R_C is the Coulomb radius that we assume to be $R_C = 1.2\,A^{1/3}\,\mathrm{fm}$ where A is the mass of the nucleus[1]. Both U_{WS} and U_{C} are spherically symmetric since we are supposing that the nucleus has the same symmetry. Hence, we can solve the Schrödinger equation in a spherically symmetric case, and therefore the wave function is $\psi(\mathbf{r}) = \psi(r, \theta, \phi)$. Re-writing the Laplace operator in spherical coordinates:

$$\nabla^2 f = \frac{1}{r^2}\frac{\partial}{\partial r}\left(r\frac{\partial f}{\partial r}\right) + \frac{1}{r^2 \sin\theta}\frac{\partial}{\partial \theta}\left(\sin\theta\frac{\partial f}{\partial \theta}\right) + \frac{1}{r^2 \sin^2\theta}\frac{\partial^2 f}{\partial \phi^2} \tag{3.6}$$

and considering the factorization of the wave function ψ:

$$\psi(r, \theta, \phi) = R(r)\Theta(\theta)\Phi(\phi), \tag{3.7}$$

substituting Equations 3.6 and 3.7 in Equation 3.4, we obtain three independent equations:

$$\frac{d^2\Phi}{d\phi^2} = -m^2\Phi \tag{3.8}$$

$$\sin\theta\frac{d}{d\theta}\left(\sin\theta\frac{d\Theta}{d\theta}\right) + \ell(\ell+1)\sin^2\theta\Theta = m^2\Theta \tag{3.9}$$

$$\frac{d}{dr}\left(r^2\frac{dR}{dr}\right) - \frac{2\mu r^2}{\hbar^2}\left[U_{\mathrm{WS}} + U_{\mathrm{C}} - E\right]R = \ell(\ell+1)R. \tag{3.10}$$

Since the phenomena we are interested in, *i.e.* scattering, are planar phenomena, the resulting wave function has an azimuthal symmetry, and then is independent of ϕ and m can be considered always equal zero. The part we are interested in solving is the radial equation, which depends on the physical properties of the particles and the potentials of the case studied. In particular, a common practice to solve the radial Schrödinger equation is to define $u(r) = rR(r)$ and substitute it in Equation 3.10, so that we obtain:

$$\frac{d^2u}{dr^2} - \left[\frac{2\mu}{\hbar^2}\left(U_{\mathrm{WS}} + U_{\mathrm{C}}\right) + \frac{\ell(\ell+1)}{r^2}\right]u = -\frac{2\mu}{\hbar^2}Eu. \tag{3.11}$$

We are interested in the calculation of the cross sections, and to do that we need a representation of the wave function in the form of ongoing and outgoing waves. In the first approximation, we can consider an ongoing plane wave and an outgoing spherical wave from the target. Then, we can write:

$$\psi(r, \theta) \propto e^{-ikz} + \frac{e^{i\mathbf{kr}}}{r}f(\theta, k) \tag{3.12}$$

---

[1] A is expressed in atomic mass unit (amu).

where f is the *scattering amplitude* and $k = p/\hbar$, with p the projectile momentum, corresponding to the free particle energy expression $E = \hbar^2 k^2/2\mu$. Considering that the wave function is the sum of contribution for each *partial-wave*, *i.e.* the contribution from each possible value of the quantum angular momentum number ℓ, also f can be written as the sum of many contributions of different ℓ. This expansion is called *partial-wave expansion* and the amplitude general form is given by:

$$f(\theta, k) = \sum_{\ell=0}^{\infty} f_\ell(\theta, k) = \frac{1}{2ik} \sum_{\ell=0}^{\infty} (2\ell + 1)(S_\ell - 1) P_l(\cos\theta) \tag{3.13}$$

where $P_\ell(x)$ are the *Legendre polynomial*

$$P_\ell(x) = \frac{1}{2^\ell \ell!} \frac{d^\ell}{dx^\ell} \left(x^2 - 1\right)^\ell, \tag{3.14}$$

while S_ℓ are the diagonal elements of the matrix that define the amplitude for each ℓ. In this case is a function of ℓ that we can calculate from the solutions of the Schrödinger equation. The relation between the scattering amplitude and the cross sections is given by [55, p. 29-30]

$$\frac{d\sigma_{el}}{d\Omega} = |f(\theta, k)|^2 = \frac{1}{4k^2} \left| \sum_{\ell=0}^{\infty} (2\ell + 1)(S_\ell - 1) P_l(\cos\theta) \right|^2 \tag{3.15}$$

where $d\sigma_{el}/d\Omega$ is the *differential cross section* with respect to the solid angle Ω for the *elastic scattering* process. In the present work, we are considering two different interactions: the electromagnetic interaction and the strong nuclear interaction. Hence, the scattering amplitude f will consist of two contributions due to the different interaction

$$f(\theta, k) = f_N(\theta, k) + f_C(\theta, k) \tag{3.16}$$

where f_N is the amplitude of the nuclear force

$$f_N(\theta, k) = \frac{1}{2ik} \sum_\ell (2\ell + 1) e^{2i\sigma_\ell} (S_\ell - 1) P_\ell(\cos\theta) \tag{3.17}$$

while f_C is the one for the Coulomb interaction

$$f_C(\theta, k) = \frac{1}{2ik} \sum_\ell (2\ell + 1)(e^{2i\sigma_\ell} - 1) P_\ell(\cos\theta) \tag{3.18}$$

where $\sigma_\ell = \arg\left[\Gamma(1 + \ell + i\eta)\right]$ is the *Coulomb phase shift*, with $\eta = Z_t e^2 \mu/\hbar p$ [55, p. 30-32].

To obtain the integral cross section, it is sufficient to integrate the Equation 3.15 on the full 4π-solid angle:

$$\sigma_{el} = \int_\Omega \frac{d\sigma_{el}}{d\Omega} d\Omega = \int_{-\pi}^{\pi} \int_{-1}^{1} \frac{d\sigma_{el}}{d\Omega} d\phi d\cos\theta = 2\pi \int_{-1}^{1} \frac{d\sigma_{el}}{d\Omega} d\cos\theta. \tag{3.19}$$

Remembering that:

$$|f|^2 = \sum_{\ell,\ell'} f_\ell f_{\ell'}^*$$

and that for the Legendre polynomial the following identity is valid:

$$\int_{-1}^{1} P_\ell(x)P_{\ell'}(x)dx = \frac{2}{2\ell+1}\delta_{\ell,\ell'}$$

where $\delta_{\ell,\ell'}$ is the *Kronecker delta*, the integration of the differential cross section is:

$$\sigma_{el} = \frac{\pi}{k^2}\sum_\ell (2\ell+1)\left|(S_\ell - 1)\right|^2 . \tag{3.20}$$

The reaction cross section, using the definition of total cross section given in Equation (2.4), is given by

$$\sigma_r = \sigma_{tot} - \sigma_{el}$$

where σ_{tot} can be calculated using the *optical theorem* which states that

$$\sigma_{tot} = \frac{4\pi}{k}\mathrm{Im}\left[f(\theta = 0)\right] . \tag{3.21}$$

Using the explicit expression of f from Equation (3.13) for $\theta = 0$, the total cross section results:

$$\sigma_{tot} = -\frac{2\pi}{k^2}\sum_\ell (2\ell+1)(\mathrm{Re}\left[S_\ell\right] - 1). \tag{3.22}$$

Therefore, the reaction cross section is

$$\sigma_r = \frac{\pi}{k^2}\sum_\ell (2\ell+1)\left(1 - |S_\ell|^2\right) . \tag{3.23}$$

In both elastic and reaction cross sections, we can notice the dependence on $1/k^2$. All the summations in Equations 3.15 and 3.23 theoretically go from 0 to infinity. However, just a limited number of partial-waves contribute in a significant way in the calculation. Therefore, in the practical applications of the partial-wave formalism, the sum on ℓ is limited to an $\ell_{\max} = kR$ where R is the *interaction range*, *i.e.* the distance at which the interaction begins to fade [55]. The interaction range depends on the nucleus we are considering since the strong interaction and the electromagnetic field depend on how many nucleons there are in the nucleus. This means that, for example, for a projectile of momentum $p = 600\,\mathrm{MeV/c}$ (*i.e.* $k = p/\hbar \approx 3\,\mathrm{fm}^{-1}$) scattered by a nucleus of carbon-12 with $A = 12\,\mathrm{amu}$ and supposing that $R = r_0 A^{1/3}$ with $r_0 \approx 1.2\,\mathrm{fm}$, we have $\ell_{\max} \approx 5$. Thus, for carbon-12 we just need 6 partial-waves to calculate with satisfying precision the cross sections.

3.3.2 Solving the non-relativistic Schrödinger equation

All the calculations in Subsection 3.3.1 require knowing the diagonal-matrix $S_{\ell\ell} = S_\ell$, which represents the nucleus interaction core information. It depends on the potential used for the problem. However, in the majority of cases, there is no analytical way to calculate this quantity, and therefore the only way is to pass through the *numerical solving* of the Schrödinger equation. As mentioned at the beginning of Section 3.3, the core of the software for the cross section calculations is a `FORTRAN77` code which calculates the cross sections using partial-wave formalism and the *distorted-wave method*. This method consists of the use of ongoing waves which are constructed as plane waves distorted by the Coulomb field of the nucleus [55, ch. 5]. Then, these waves are scattered by the nuclear strong force, and the result includes both the electromagnetic and the strong forces. The *Coulomb waves* are well known in literature and can be easily calculated analytically or numerically. The main problem is the calculation of the outgoing waves, which must be done numerically using an algorithm to solve the radial Schrödinger equation, *i.e.* an ordinary differential equation of second order in which the first-order term does not appear. To do that, the `FORTRAN77` code uses the *Numerov-Fox-Goodwin algorithm* [56, ch. 13], a fourth-order linear multi-step method to solve differential equations of the form

$$\frac{d^2y}{dx^2} = -g(x)y(x) + s(x). \tag{3.24}$$

The formal solution for the step $n+1$ is given by the expression:

$$\begin{aligned} y_{n+1}\left(1+\frac{h^2}{12}g_{n+1}\right) = 2y_n\left(1-\frac{5h^2}{12}g_n\right) - y_{n-1}\left(1+\frac{h^2}{12}g_{n-1}\right) + \\ + \frac{h^2}{12}\left(s_{n+1}+10s_n+s_{n-1}\right) + \mathcal{O}(h^6). \end{aligned} \tag{3.25}$$

Since our case corresponds to the substitutions

$$x = r, \tag{3.26}$$

$$y = u(r), \tag{3.27}$$

$$g = \frac{2\mu}{\hbar^2}\left(U_{\mathrm{WS}} + U_{\mathrm{C}} - E\right) + \frac{\ell(\ell+1)}{r^2}, \tag{3.28}$$

$$s = 0 \tag{3.29}$$

the Equations 3.24 and 3.25 reduce to

$$\frac{d^2u}{dr^2} = -g(r)u(r) \tag{3.30}$$

$$u_{n+1}\left(1+\frac{h^2}{12}g_{n+1}\right) = 2u_n\left(1-\frac{5h^2}{12}g_n\right) - u_{n-1}\left(1+\frac{h^2}{12}g_{n-1}\right). \tag{3.31}$$

The quantity S_ℓ is usually parametrized using the *phase shift* δ_ℓ (in general a complex parameter) in the form

$$S_\ell = e^{2i\delta_\ell} \tag{3.32}$$

similarly to the Coulomb phase shift σ_ℓ. With this parametrization, we can calculate the phase shift δ_ℓ and then calculate the element S_ℓ and use it in the cross section formulae. The Schrödinger equation solutions at large distances from the nucleus, *i.e.* where all the potentials are negligible, have analytical solutions, which are

$$\chi_\ell(r) \propto kr\left[j_\ell(kr)\cos\delta_\ell - n_\ell(kr)\sin\delta_\ell\right]. \tag{3.33}$$

where j and n are the *spherical Bessel functions*

$$j_\ell(x) = (-x)^\ell \left(\frac{1}{x}\frac{d}{dx}\right)^\ell \frac{\sin x}{x} \tag{3.34}$$

$$n_\ell(x) = -(-x)^\ell \left(\frac{1}{x}\frac{d}{dx}\right)^\ell \frac{\cos x}{x}. \tag{3.35}$$

If we take as "large distance from nucleus" $r = r_{\max}$ and we take another radius $r' > r_{\max}$, we can divide the two solutions at different radii and obtain the ratio

$$\mathcal{K}(\delta_\ell) = \frac{r'\chi_\ell(r_{\max})}{r_{\max}\chi_\ell(r')} = \frac{j_\ell(kr_{\max}) - n_\ell(kr_{\max})\tan\delta_\ell}{j_\ell(kr') - n_\ell(kr')\tan\delta_\ell}. \tag{3.36}$$

Thus, we can calculate δ_ℓ from

$$\tan\delta_\ell = \frac{\mathcal{K}j_\ell(kr') - j_\ell(kr_{\max})}{\mathcal{K}n_\ell(kr') - n_\ell(kr_{\max})} \tag{3.37}$$

where in our case $\mathcal{K}$ has been calculated with the numerical solution u_ℓ of the Schrödinger equation, hence

$$\mathcal{K} = \frac{r'u_\ell(r_{\max})}{r_{\max}u_\ell(r')}. \tag{3.38}$$

The `FORTRAN77` code implements these methods, calculating the δ_ℓ, then $S_\ell = e^{2i\delta_\ell}$ used in Equation 3.13 and finally allows us to calculate the differential and integral cross sections using Equations 3.15, 3.20 and 3.23.

3.3.3 Fitting procedure

To perform the fitting, the `FORTRAN77` code has been wrapped with a `Python` code and five software with graphic interfaces have been created (see Appendix A) to automatize the procedure. The output of the `FORTRAN77` code is used to define functions in the `Python3` code, using the `subprocess` class and methods. The functions are defined so that the user can change the number of parameters used in the fitting procedure. The Woods-Saxon shape has 5, 6, or 7 free parameters, including a possible *normalization factor* of the model. We take into account this normalization factor λ in the definition of the χ^2

$$\chi^2 = \min_\lambda \left[\sum_i^N \left(\frac{\sigma^{\mathrm{ex}}(x_i) - \lambda\sigma^{\mathrm{th}}(x_i)}{\Delta\sigma_i}\right)^2 + \left(\frac{\lambda - \lambda_0}{\Delta\lambda}\right)^2\right] \tag{3.39}$$

where σ^α ($\alpha = (\mathrm{ex}, \mathrm{th})$, *i.e.* experimental and theoretical) here is used for both differential and integral cross sections, $\Delta\sigma_i$ is the uncertainty over the i-th experimental data and $\Delta\lambda = 0.1$ is the uncertainty over normalization factor λ. The *pull* term of the χ^2 function is present to force the value of λ around the value $\lambda_0 = 1$ so that λ must be in $[\lambda_0 - \Delta\lambda, \lambda_0 + \Delta\lambda] = [0.9, 1.1]$ after the fitting procedure. The choice fell on this definition of the χ^2 since is similar to the standard χ^2, which is simpler than the other χ^2 choices that required also the calculation of the derivative of the cross section, with the addition of the normalization factor, which can take into account experimental error and data underestimation (or overestimation).

To do the fit to the data listed in Section 3.1, we use the `Python` package `iMinuit` (version 2.16.0) – derived from the `Minuit` package of `FORTRAN77` and `C++` languages –, using Migrad and Simplex algorithms for the minimization of the χ^2 and Hesse and Minos for the calculation of covariance matrix and asymptotic and asymmetric errors.

Since the function is written in a `FORTRAN77` code and we call it from a `Python` code, the procedure is quite slow.

3.4 Summary

The data used in the analysis were described and the references to these data were reported. Due to the absence of properly reported antiproton scattering data on the main online database available (*e.g.* EXFOR), we had to extract data directly from the figures in the articles using a software tool. These procedures introduced small errors that cannot be eliminated. This highlights the fact that antiproton scattering and annihilation data are not available to everyone since they were frequently exchanged via *private communications.* The only data available are the ones by Nakamura *et al.* [57].

After that, we reported in detail the optical potential we chose and the reasons behind this choice. We also explained the method used to solve the non-relativistic Schrödinger equation, which consists mainly of a *Numerov-Fox-Goodwin algorithm.* To do that, we also had to take into account the formalism used to solve the Schrödinger equation, *i.e.* the *partial-wave formalism.* We finally defined the fitting procedure, based on the minimization of a χ^2 with a normalization parameter constrained by a pull term.

Chapter 4

Analysis of the Scattering Data

4.1 Analysis of the experimental data

In the present work, we limit our analysis to the data of the following targets:

- ^{12}C (elastic scattering and reaction)
- ^{16}O (elastic scattering)
- ^{40}Ca (elastic scattering and reaction)
- ^{208}Pb (elastic scattering and reaction)

As seen in Chapter 2, these are the same data used in the previous analyses. In that way, the results of the present work can be compared with the previous works.

In these data, the antiproton kinetic energies (momenta) are about 50 MeV ($\sim$ 300 MeV/c) and 180 MeV ($\sim$ 600 MeV/c) in the center-of-mass frame for the differential elastic scattering cross section data. Data for elastic scattering were extracted from the plots of Ref. [48]. For the reaction cross sections, we used data summarized in Ref. [18].

The analysis of the data has been done using different numbers of free parameters:

- 5 parameters: V_0, W_0, $r_{0R} = r_{0I} = r_0$, $a_R = a_I = a$, λ
- 6 parameters: V_0, W_0, r_{0R}, r_{0I}, $a_R = a_I = a$, λ
- 7 parameters: V_0, W_0, r_{0R}, r_{0I}, a_R, a_I, λ.

These parameters were implemented in the original `FORTRAN77` code, apart from λ.

For simplicity, all the parameters are assumed to be momentum-independent, *i.e.* they do not change value with the change of the projectile momentum. Considering the potential defined in Equation 3.1 and these conditions, the potential used here is

$$-V_{\text{opt}}(r) = V_0\mathcal{F}(r, r_{0R}, a_R) + iW_0\mathcal{F}(r, r_{0I}, a_I) \tag{4.1}$$

where

$$\mathcal{F}(r, r_{0x}, a_x) = \left[1 + \exp\left(\frac{r - r_{0x}A^{\frac{1}{3}}}{a_x}\right)\right]^{-1} \tag{4.2}$$

where A is as usual the nucleus mass in amu unit.

Using this sign convention, the values of V_0 and W_0 must be greater than zero since we are assuming an attractive potential[1], and therefore we limited our search to that region. The geometrical parameters (r_{0x}, a_x) are limited to positive values since they represent spatial extensions.

We are considering all the nuclei in the analysis as spherical, without any distortion.

As mentioned above, we changed the number of free parameters during the analysis to understand which is the minimum number of parameters that could be adequate to reproduce the data of different energies.

The analysis is done only on the differential elastic scattering cross section data since the reaction cross section data have only a few points and the direct fitting is not reliable[2]. Instead, the reaction cross sections are calculated using the same parameters of the differential elastic scattering and Equation (3.23).

The parameters are calculated from the minimization of the χ^2 defined in Equation 3.39. The minimization is performed using the `iMinuit` (version 2.16.0) Python3 package[58], using `MIGRAD` algorithm[59] and the Hessian method for the calculation of the asymptotic errors of the parameters evaluation. Knowing these errors, the 1-σ and 2-σ error bands are calculated via propagation – using the `jacobi.propagate` Python3 method – and represented graphically together with the best-fit line.

4.2 Results

In the following sections, we present the results of the fitting divided by target and projectile momentum. For each nucleus, we present analyses with 5, 6, and 7 parameters.

4.2.1 Carbon-12

4.2.1.1 300 MeV/c

Data at projectile-momentum 300 MeV/c [46] are distributed quite homogeneously in the range 0° – 65°. The number of data of this measurement is $n_{\mathrm{data}} = 45$. In particular, in the region around the minimum of the oscillating pattern, we have two points[3]. In Figures 4.1 the results of the fitting are shown, together with the experimental data from Ref. [46]. The parameter values are summarized in Tables 4.1.

The 5-parameter fit (Figure 4.1a) is quite precise in determining all the parameters, except for W_0 which has around 50 % error. The 6- and 7-parameter fits are very similar in values. The main differences between the 5- and 6-/7-parameter fit are the different values for the real and imaginary part and the normalization factor λ. The difference in U_0 and W_0 values can be understood by noticing that in both

---

[1] In general, this is not true, since they can be attractive or repulsive depending on the distance between the projectile and the nucleus. However, these limitations are confirmed by many attempts that we have performed where the parameters were set free without any limitation of values and they always went on positive values. The negative values were associated with many problems in convergence or with unexpected values of the geometrical parameters.

[2] This fact was also observed during many tries, which are not presented in this work due to the unsatisfactory results obtained.

[3] These comments in the present chapter are explained more in detail in Chapter 5.

n_{par}	U_0 [MeV]	W_0 [MeV]	$r_{0\text{R}}$ [fm]	$r_{0\text{I}}$ [fm]	a_{R} [fm]	a_{I} [fm]	λ	$\tilde{\chi}^2$
5	18 ± 5	27 ± 12	1.35 ± 0.13	—	0.43 ± 0.07	—	1.19 ± 0.03	0.78
6	23 ± 5	16 ± 6	1.3 ± 0.1	1.5 ± 0.1	0.40 ± 0.05	—	1.0 ± 0.1	0.70
7	23 ± 5	16 ± 5	1.3 ± 0.1	1.5 ± 0.1	0.4 ± 0.1	0.4 ± 0.1	1.00 ± 0.09	0.72

Table 4.1: Best-fit parameters for ^{12}C at $p = 300\,\text{MeV/c}$ ($n_{\text{dof}} = 45 - n_{\text{par}}$). The empty cells are for geometrical parameters forced to be the same in value as the corresponding ones of the real part.

the 6- and 7-parameter fits the imaginary radii are bigger than the real ones. This fact seems to compensate for the lower value for W_0. It is not possible to observe this feature in the 5-parameter fit since $r_{0R} = r_{0I}$. About λ, it is more difficult to understand the reason for the change in value. This parameter could represent an underestimation of experimental errors in the 5-parameter fit; however, for the 6- and 7-parameter fits λ seems to be around 1.0.

All the fits have a low reduced χ^2 (~ 0.7). This is an indication of a good fit – which can be assessed also from Figures 4.1. In this case, the 5-parameter description seems to suffice to describe the observed data.

4.2.1.2 608 MeV/c

As in the 300 MeV/c case, the data are homogeneously distributed in the same range ($0° - 65°$), with around the same number of data ($n_{\text{data}} = 47$). Some data are near the minimum of the diffraction pattern at $\theta \sim 45°$. When these points are present, we notice that the fits are more stable in the values and they seem to converge more easily.

The best-fit parameters values are reported in Table 4.2. The best-fit curves and error bands with the relative data from Ref. [45] are shown in Figures 4.2.

n_{par}	U_0 [MeV]	W_0 [MeV]	r_{0R} [fm]	r_{0I} [fm]	a_R [fm]	a_I [fm]	λ	$\tilde{\chi}^2$
5	71 ± 7	159 ± 18	0.97 ± 0.03	—	0.478 ± 0.009	—	1.20 ± 0.03	0.90
6	52 ± 15	179 ± 29	1.05 ± 0.08	0.94 ± 0.04	0.477 ± 0.009	—	1.22 ± 0.03	0.92
7	64 ± 20	158 ± 44	1.03 ± 0.08	0.96 ± 0.06	0.43 ± 0.06	0.49 ± 0.02	1.21 ± 0.04	0.93

Table 4.2: Best-fit parameters for ^{12}C at $p = 607.9\,\text{MeV/c}$ ($n_{\text{dof}} = 47 - n_{\text{par}}$). The empty cells are for geometrical parameters forced to be the same in value as the relative one of the real/imaginary part.

An important difference with respect to the previous case is the absorptive character of the optical potential for all fits with different numbers of parameters. The values are quite stable varying the number of parameters used ($U_0 \sim 50$–$70\,\text{MeV}$, $W_0 \sim 160$–$180\,\text{MeV}$, $r_{0R} \sim 1$–$1.05\,\text{fm}$, $r_{0I} \sim 0.95\,\text{fm}$, $a_R \sim a_I \sim 0.4$–$0.5\,\text{fm}$). Moreover, the normalization λ has always a value around 1.2, which can be interpreted as an underestimation of experimental data values. A good fit of the theoretical curves to the data can be observed also in this case ($\tilde{\chi}^2 \sim 0.9$). The 5-parameter description suffices for a good description of the potential in this case. For 6- and 7-parameter fits, the errors on the estimation of U_0 and W_0 are quite large (~ 20–$30\,\%$). These changes in the strengths parameters do not imply necessarily a large difference in the cross section values if one considers only the range of the data. In this region,

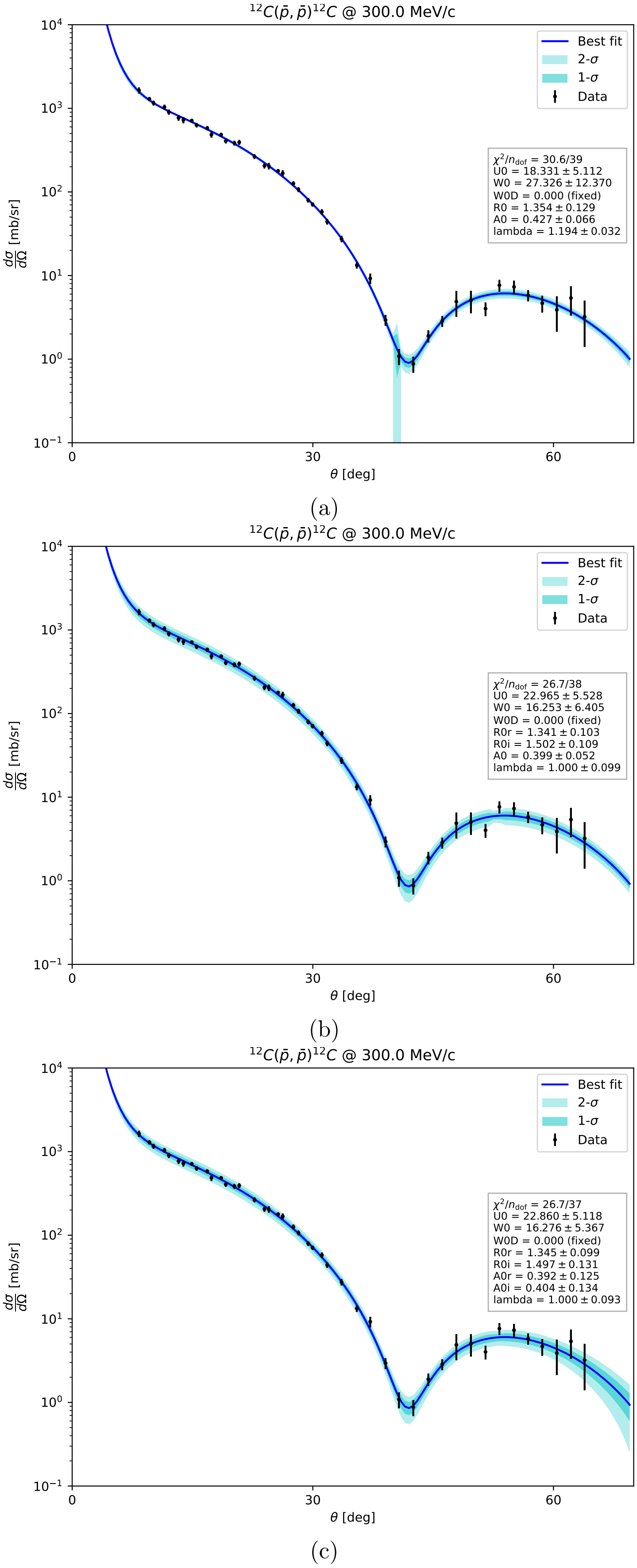

(a)

(b)

(c)

Figure 4.1: 5- (4.1a), 6- (4.1b) and 7- (4.1c) parameter best-fit curve with error bands at 1-σ and 2-σ for ^{12}C at $E_{\bar{p}} = 46.8\,\text{MeV}$ ($p = 300\,\text{MeV/c}$) between $0° - 65°$.

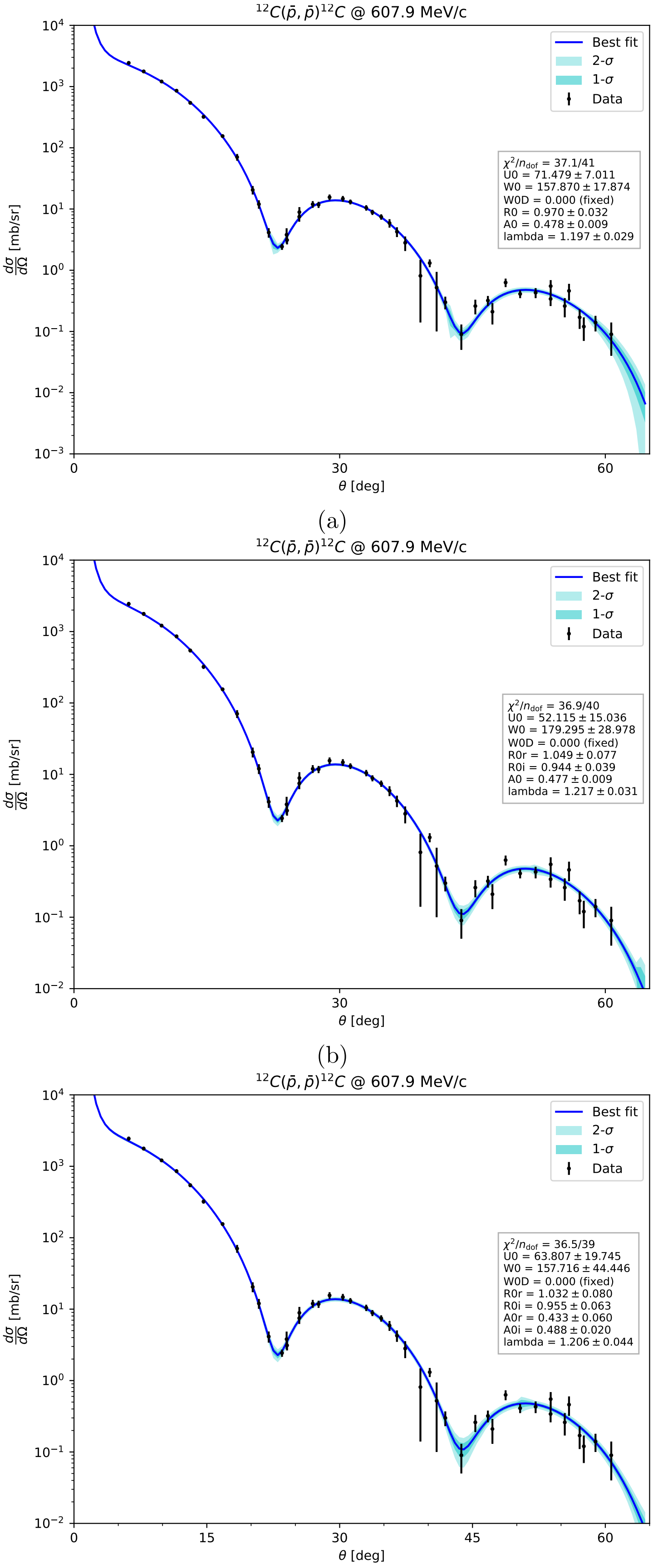

Figure 4.2: 5- (4.2a), 6- (4.2b) and 7- (4.2c) parameters best-fit curve with error bands at 1-σ and 2-σ for ^{12}C at $E_{\bar{p}} = 179.7\,\text{MeV}$ ($p = 607.87\,\text{MeV/c}$) between $0^\circ - 65^\circ$.

the changes in values of the cross section are much smaller than for angles larger than 65° (see the Supplementary Figures B.8).

4.2.1.3 466 MeV/c **and** 522 MeV/c

Some attempts of fitting to data taken by Nakamura *et al.* [57] for $p = 466\,\mathrm{MeV/c}$ and $p = 522\,\mathrm{MeV/c}$ have been done. However, no convergence has been reached in any attempt. The explanation of this problem could be in the very-narrow angle range $0^\circ - 20^\circ$ of these data. In this region, many different values of the parameters can be used and no changes can be observed (see Figure B.10). Data for the same range as before $(0^\circ - 65^\circ)$ could have helped to find a possible *momentum-dependent function* to describe the variation of strength parameters.

4.2.1.4 Reaction cross sections

Using the values found with the previous fits, the reaction cross sections are calculated and then compared with the available experimental data. The results of this procedure are in Table 4.3 and represented graphically in Figures 4.3 and 4.4.

p [MeV/c]	$\mathbf{n}_{\mathrm{par}}$	σ_r^{th} [mb]	σ_r^{x} [mb]
300.0	5	326 ± 29	—
	6	227 ± 17	
	7	297 ± 30	
607.9	5	400 ± 3	$483 \pm 20^{(*)}$
	6	400 ± 4	
	7	401 ± 4	

$^{(*)}p = 622\,\mathrm{MeV/c}$

Table 4.3: Predicted values of the reaction cross section at for ^{12}C, compared with the experimental value in the nearest value of momentum.

In the figures, the χ^2 is not to be intended as in the fitting case since we do not fit directly to the reaction cross section data. It can be interpreted as the sum of the squared residuals. Therefore, it is simply an indicator of how much the theoretical curve is in the proximity of experimental data, considering experimental errors.

The 5-parameter case for 300 MeV/c antiproton (Figure 4.3a) reproduces better the reaction cross section data than the 6- and 7-parameter fitting values (Figures 4.3b and 4.3c). However, no one of the best-fit values seems to determine accurately the experimental data behavior, both at low ($p < 300\,\mathrm{MeV/c}$) and high ($p > 300\,\mathrm{MeV/c}$) momenta. Moreover, there is no data near $p = 300\,\mathrm{MeV/c}$ to compare them with the theoretical curve.

On the contrary, the best-fit values for 608 MeV/c antiproton give good agreement between experimental data and the calculated reaction cross sections for all the data with $p \geq 600\,\mathrm{MeV/c}$ (see Figure 4.4). The only datum outside the prediction is the one at $p = 100\,\mathrm{MeV/c}$, which is around 2–3-σs distant from the theoretical curve. Again, the 5-parameter fit values (Figure 4.4b) seem to reproduce slightly better the experimental reaction cross section data with respect to 6- and 7-parameter ones(Figures 4.4b and 4.4c). From the graphical results and the χ^2, the

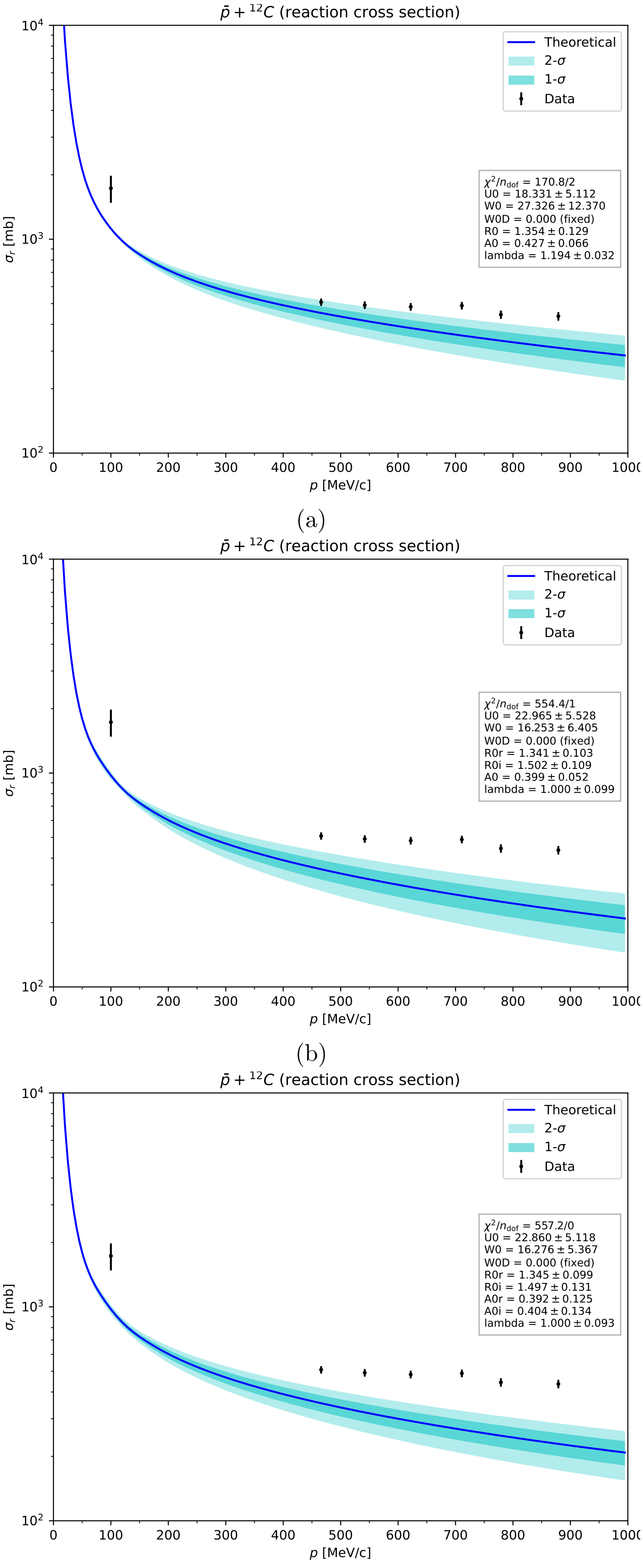

(a)

(b)

(c)

Figure 4.3: Theoretical curves of the reaction cross section using best-fit results at 300 MeV/c from Table 4.1 for 5- (4.3a), 6- (4.3b) and 7- (4.3c) parameter fits.

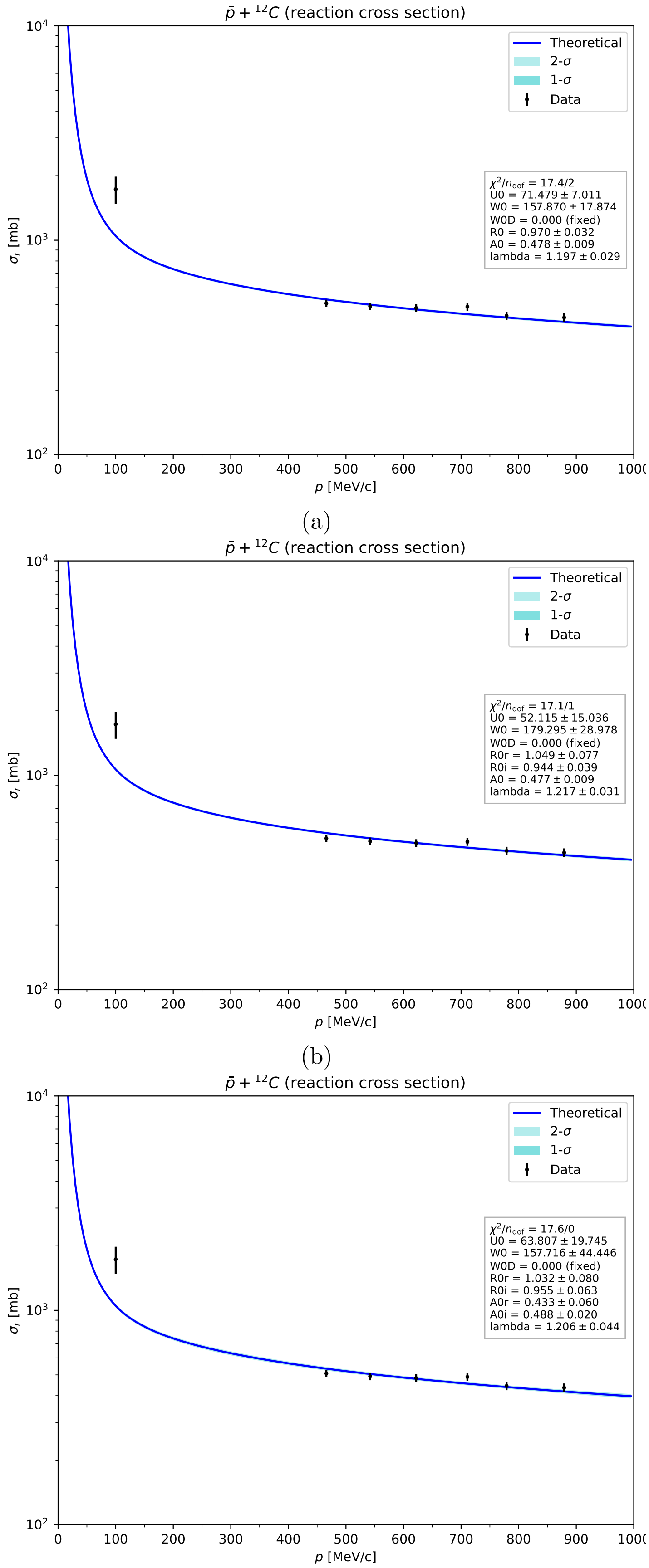

(a)

(b)

(c)

Figure 4.4: Theoretical curves of the reaction cross section using best-fit results at 607.9 MeV/c from Table 4.2 for 5 (4.4a), 6 (4.4b) and 7 (4.4c) parameters fits.

theoretical curves for the reaction cross sections fairly agree with experimental data. The error bands in these figures are very narrow, so they practically are invisible.

The agreement of the theoretical curves with experimental data for 608 MeV/c and not for 300 MeV/c is not a surprise. The available reaction cross section data are in momentum regions outside the data analysed for the best-fit values. Moreover, we know from theory that above a certain threshold, the reaction cross section tends to flatten, which is the case for data above 608 MeV/c that are quite similar in σ_r values ($\sim$ 500–600 mb). Therefore, the best-fit values found at $p = 608$ MeV/c give a better agreement with respect to the ones at $p = 300$ MeV/c. Both show a similar distance from the 100 MeV/c datum, which is outside the momentum range of both fits. This fact can be seen as evidence of the energy dependence of some parameters of the optical potential.

From Table 4.3 we can see, however, that the calculated values are slightly below concerning the experimental datum at 622 MeV/c, resulting in a global underestimation of the reaction cross section. No comparison is possible with 300 MeV/c since the absence of reaction cross section data in this region.

4.2.2 Oxygen-16

4.2.2.1 605 MeV/c

For oxygen-16, data are only available at projectile-momentum 605.5 MeV/c. Data are distributed in the range $0° - 60°$ quite homogeneously as for ^{12}C, with $n_{\text{data}} = 29$. Also in this case, some data near the first two minima of the diffraction pattern ($\sim 20°$ and $\sim 38°$) are present. In Figures 4.5 the results of the fitting are shown with the data from Ref. [48]. The parameter values are summarized in Tables 4.4.

n_{par}	U_0 [MeV]	W_0 [MeV]	$r_{0\text{R}}$ [fm]	$r_{0\text{I}}$ [fm]	a_{R} [fm]	a_{I} [fm]	λ	$\tilde{\chi}^2$
5	37 ± 2	72 ± 6	1.19 ± 0.02	—	0.46 ± 0.01	—	1.19 ± 0.03	2.0
6	39 ± 14	71 ± 12	1.18 ± 0.07	1.19 ± 0.04	0.46 ± 0.01	—	1.18 ± 0.08	2.1
7	38 ± 9	70 ± 9	1.19 ± 0.06	1.19 ± 0.03	0.46 ± 0.05	0.47 ± 0.02	1.18 ± 0.06	2.2

Table 4.4: Best-fit parameters for ^{16}O at $p = 605.5$ MeV/c ($n_{\text{dof}} = 29 - n_{\text{par}}$). The empty cells are for geometrical parameters forced to be the same in value as the relative one of the real/imaginary part.

Again, the 5-parameter scenario suffices to describe with good agreement the scattering data. The parameters values are quite constant for all fits with different number of parameters used ($U_0 \sim 38$ MeV, $W_0 \sim 71$ MeV, $r_{0R} \sim r_{0I} \sim 1.2$ fm, $a_{0R} \sim a_{0I} \sim 0.46$ fm). The normalization factor λ is constant in the different fits with a value around $\lambda \sim 1.18$, which could be a sign that the systematic errors could have been underestimated. Moreover, this parameter has also the same values of the ^{12}C 5-parameter case for $p = 300$ MeV/c and near the values of 607.9 MeV/c cases, which is in agreement with the fact that they come from the same experiment.

From the Figures 4.5a, 4.5b and 4.5c we can see that in all the cases the best-fit line is in good agreement with data. There is an exception for the datum at $\theta \sim 38°$, which in all cases results to be around 3–4-σs distant from the calculated cross section at this angle. The other data seems to follow the behavior of the curve – in the experimental error limit.

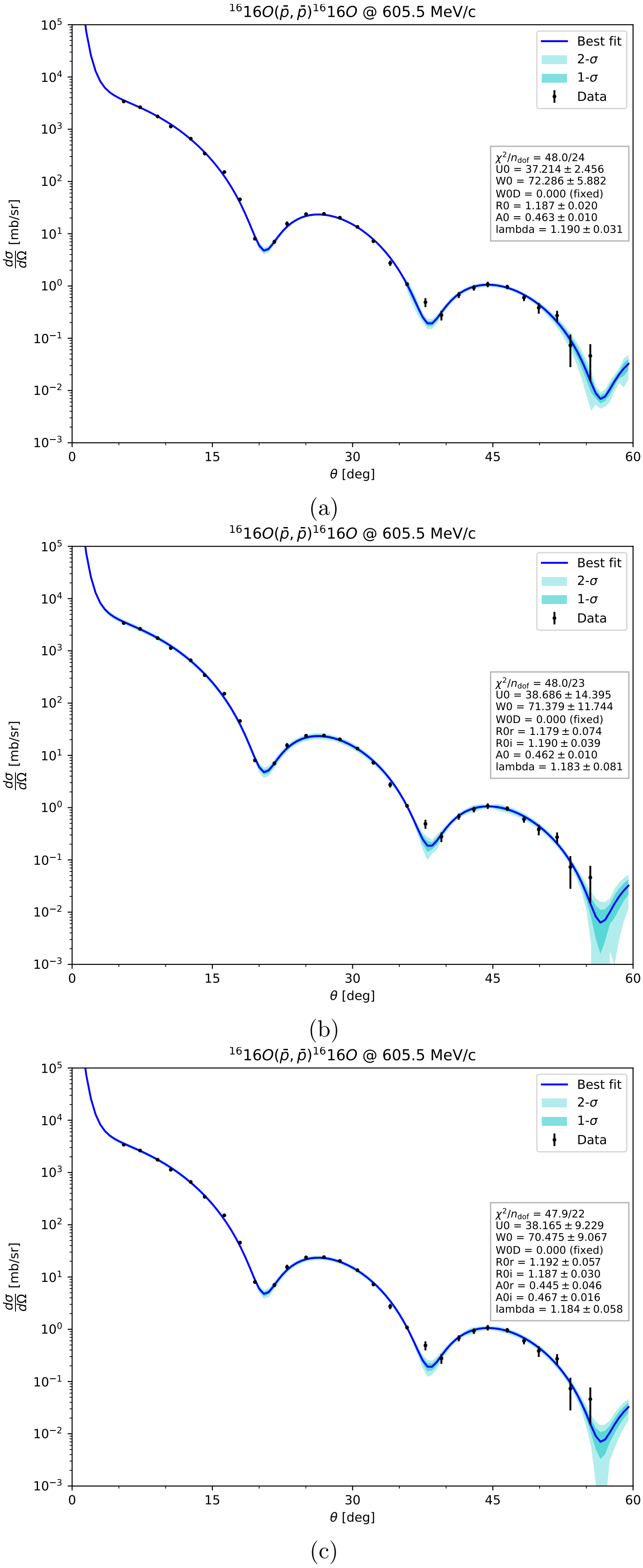

Figure 4.5: 5- (4.5a), 6- (4.5b) and 7- (4.5c) parameters best-fit curve with error bands at 1-σ and 2-σ for ^{16}O at $E_{\bar{p}} = 178.4\,\mathrm{MeV}$ ($p = 605.5\,\mathrm{MeV/c}$) between $0° - 60°$.

4.2.2.2 Reaction cross sections

For ^{16}O, there are no low-momentum ($p < 605.5\,\mathrm{MeV/c}$) elastic scattering or reaction cross section data. However, we calculated the reaction cross section at the momentum of the data fitted in the analysis and compared the value with the datum for the element with the closest mass and projectile momentum available. Our choice is then to compare these values with the ^{12}C datum at 622 MeV/c.

p [MeV/c]	$\mathbf{n}_{\mathrm{par}}$	σ_r^{th} [mb]	σ_r^{x} [mb]
605.5	5	481 ± 5	$483 \pm 20^{(*)}$
	6	481 ± 5	
	7	481 ± 5	

$^{(*)}$ ^{12}C, $p = 622\,\mathrm{MeV/c}$

Table 4.5: Predicted values of the reaction cross section at for ^{16}O, compared with the datum of ^{12}C at similar energy.

We also include the prediction of the reaction cross sections for ^{16}O in the range 0–1000 MeV/c. These are represented in Figures 4.6.

No particular differences between the 5- (4.6a), 6- (4.6b), and 7-parameter (4.6c) theoretical curves can be observed. The best-fit parameters are very similar between the various fits, hence the shape of the curve does not change appreciably.

4.2.3 Calcium-40

4.2.3.1 303 MeV/c

The 303.3 MeV/c data are distributed in the range $0° - 45°$ quite homogeneously with $n_{\mathrm{data}} = 23$. The parameter values are summarized in Tables 4.6.

$\mathbf{n}_{\mathrm{par}}$	$\mathbf{U_0}$ [MeV]	$\mathbf{W_0}$ [MeV]	$\mathbf{r}_{0\mathrm{R}}$ [fm]	$\mathbf{r}_{0\mathrm{I}}$ [fm]	$\mathbf{a}_{\mathrm{R}}$ [fm]	$\mathbf{a}_{\mathrm{I}}$ [fm]	λ	$\tilde{\chi}^2$
5	93.1 ± 1.2	22.1 ± 1.5	1.152 ± 0.012	—	0.498 ± 0.015	—	1.045 ± 0.024	1.6
6	98 ± 8	20 ± 2	1.10 ± 0.08	1.21 ± 0.07	0.54 ± 0.05	—	1.04 ± 0.02	1.6
7	—	—	—	—	—	—	—	—

Table 4.6: Best-fit parameters for ^{40}Ca at $p = 303.3\,\mathrm{MeV/c}$ ($n_{\mathrm{dof}} = 23 - n_{\mathrm{par}}$). The empty cells are for geometrical parameters forced to be the same in value as the corresponding ones of the real part. In this case, the 7-parameter fit is not present due to failure of convergence.

For low-momentum antiproton the optical potential tends to have a deep real part and a shallow imaginary one, contrary to what we found in the other targets. Both the fits result in the deep-real/shallow-imaginary case and a reduced $\chi^2 \sim 1.6$. In general, the evaluation errors seem to be very small and normalization $\lambda \sim 1.0$. Despite the small number of data, the fits are in good agreement with the data.

In Figures 4.7 the results of the fitting and the relative data from Ref. [48] are shown. The most distant point is the small-angle one, nearby $\theta \sim 10°$. In this case, data cover just one of the minima of the diffraction pattern ($\theta \sim 27°$) and the range for this energy is quite narrow to perform a good fit as in the ^{12}C cases.

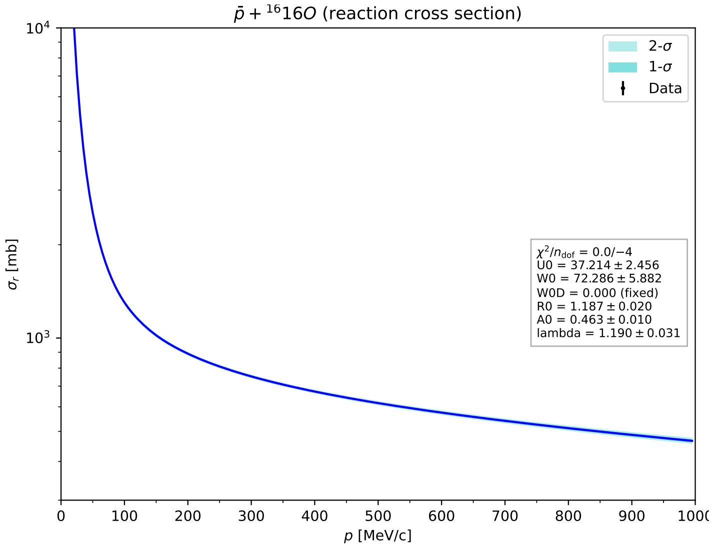

(a)

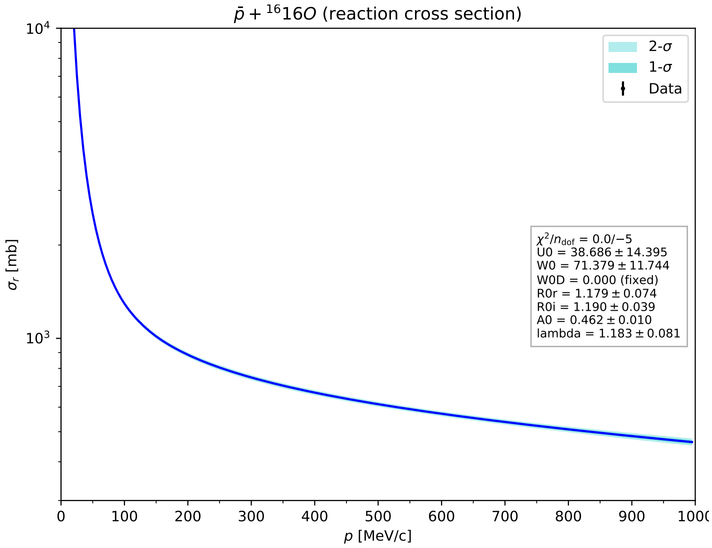

(b)

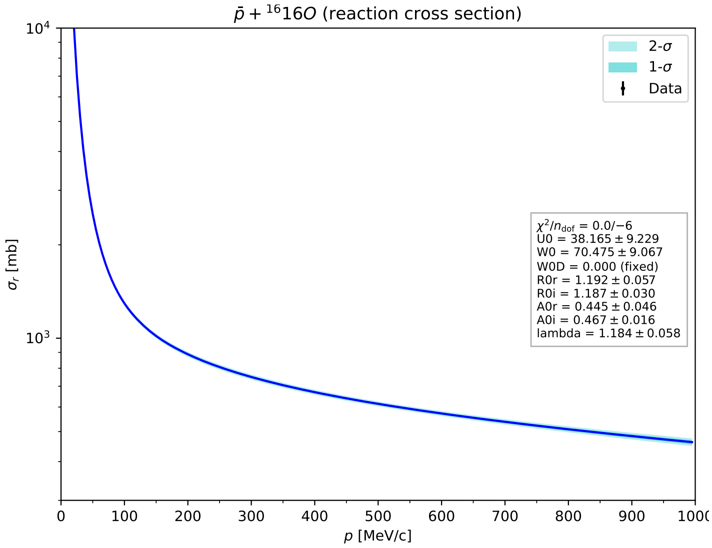

(c)

Figure 4.6: Reaction cross section theoretical curves using best fit results from Table 4.4 for 5 (4.6a), 6 (4.6b) and 7 (4.6c) parameters fits.

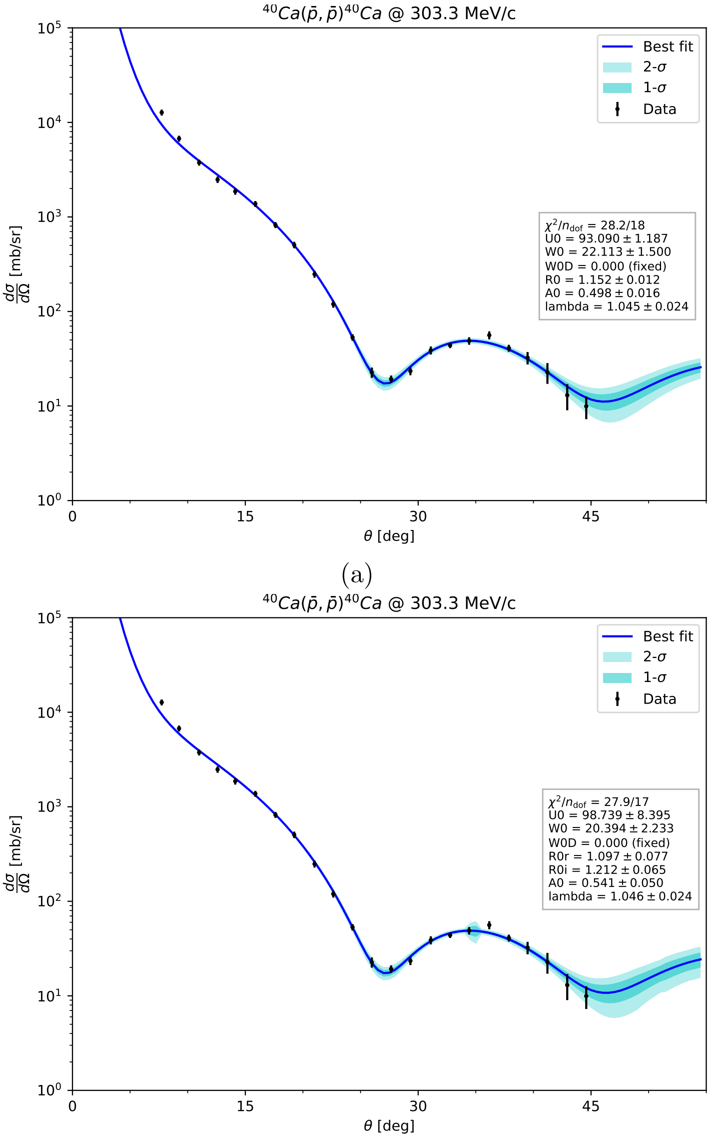

(a)

(b)

Figure 4.7: 5- (4.7a) and 6- (4.7b) parameters best-fit curve with error bands at 1-σ and 2-σ for ^{40}Ca at $E_{\bar{p}} = 46\,\mathrm{MeV}$[?]($p = 303.3\,\mathrm{MeV/c}$) between $0^\circ - 45^\circ$.

The 7-parameter case is absent since no convergence has been found in many tries. In general, this case is quite anomalous and it is difficult to understand the reasons for this anomaly, if not for the motivation we have given about the experimental data and their range.

4.2.3.2 608 MeV/c

For the highest momentum case (608 MeV/c), the data [48] are in the range $0° - 55°$ and $n_{\text{data}} = 45$. The best-fit parameters values are reported in Table 4.7.

$\mathbf{n}_{\text{par}}$	$\mathbf{U_0}$ [MeV]	$\mathbf{W_0}$ [MeV]	$\mathbf{r}_{0\text{R}}$ [fm]	$\mathbf{r}_{0\text{I}}$ [fm]	$\mathbf{a}_{\text{R}}$ [fm]	$\mathbf{a}_{\text{I}}$ [fm]	λ	$\tilde{\chi}^2$
5	26 ± 2	37 ± 4	1.33 ± 0.02	—	0.50 ± 0.02	—	1.14 ± 0.03	3.0
6	25 ± 3	38 ± 5	1.33 ± 0.03	1.32 ± 0.03	0.51 ± 0.02	—	1.16 ± 0.05	3.1
7	28 ± 2	28 ± 6	1.35 ± 0.02	1.30 ± 0.05	0.37 ± 0.02	0.67 ± 0.04	1.09 ± 0.08	2.75

Table 4.7: Best-fit parameter for ^{40}Ca at $p = 608$ MeV/c ($n_{\text{dof}} = 45 - n_{\text{par}}$). The empty cells are for geometrical parameters forced to be the same in value as the relative one of the real/imaginary part.

We have a shallow-real/deep-imaginary optical potential. However, real and imaginary strengths are closer to each other in value than the previous cases. The values are almost constant in the various cases, apart from the 7-parameter case in which we have $U_0 \simeq W_0$. In previous fits, this equality is compensated by higher or lower values in the respective real or imaginary geometrical parameters. In this case, however, we have $a_R < a_I$ which is also $a_R^{7par} < a_R^{5/6par}$. Apart from these discrepancies, we observe that the values are coherent and among the various fits are quite stable. The values of the reduced χ^2s are close to each other ($\tilde{\chi}^2 \sim 3$) with the lower value for the 7-parameter case. No fit, however, reaches a value $\tilde{\chi}^2 < 2.0$. Looking at Figures 4.8, which show the best-fit lines and relative error bands and data from Ref. [48], the best-fit curves agree with experimental data, except for data in the range $33° - 40°$, which have also small experimental errors. Hence, the higher χ^2 value can be imputed to this behavior at these angles.

Data for $\theta > 40°$ oscillate around the best-fit curve; however, their experimental errors are enough big to include at least the 2-σ error band of the best-fit curve. In general, the fits for the 608 MeV/c antiproton are more reliable than the previous ones for ^{40}Ca. Moreover, the agreement is discretely good.

4.2.3.3 Reaction cross sections

The reaction cross sections for each fit have been calculated and reported in Table 4.8.

Despite the differences in the parameter values, the 303.3 MeV/c cross sections give similar results ($\overline{\sigma}_r^{th} \sim 1021$ mb with an error of about 38 mb). In the 608 MeV/c case, the reaction cross sections are almost identical in values and sufficiently close to the measurement at similar momentum (622 MeV/c). Again, the theoretical calculation underestimates the reaction cross sections, even if the $1/p^2$ scaling is considered.

Differences among the various 300 MeV/c fits can be observed in the reaction cross section plots (Figures 4.9). In the 5-parameter case (Figure 4.9a) some weak

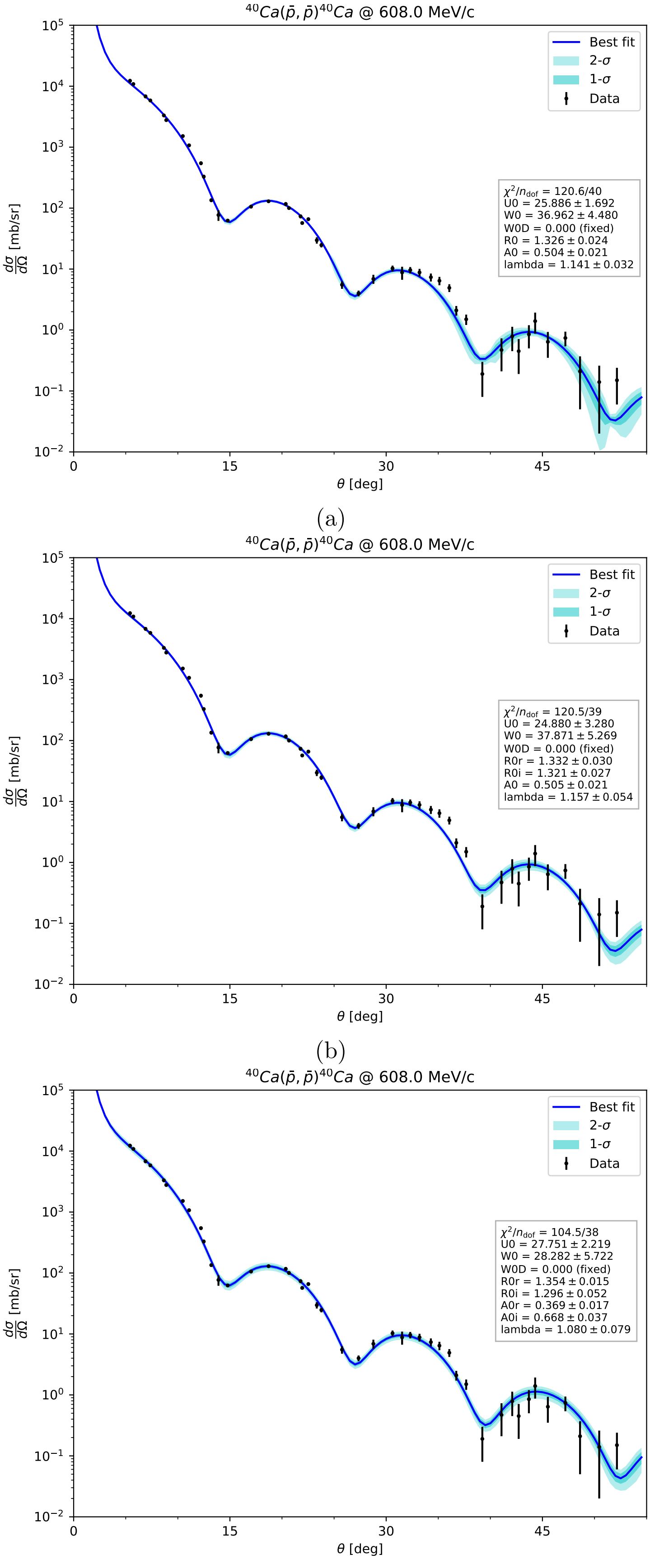

(a)

(b)

(c)

Figure 4.8: 5- (4.8a), 6- (4.8b) and 7- (4.8c) parameter best-fit curve with error bands at 1-σ and 2-σ for ^{40}Ca at $E_{\bar{p}} = 179.8\,\mathrm{MeV}$[?]($p = 608\,\mathrm{MeV/c}$) between $0° - 55°$.

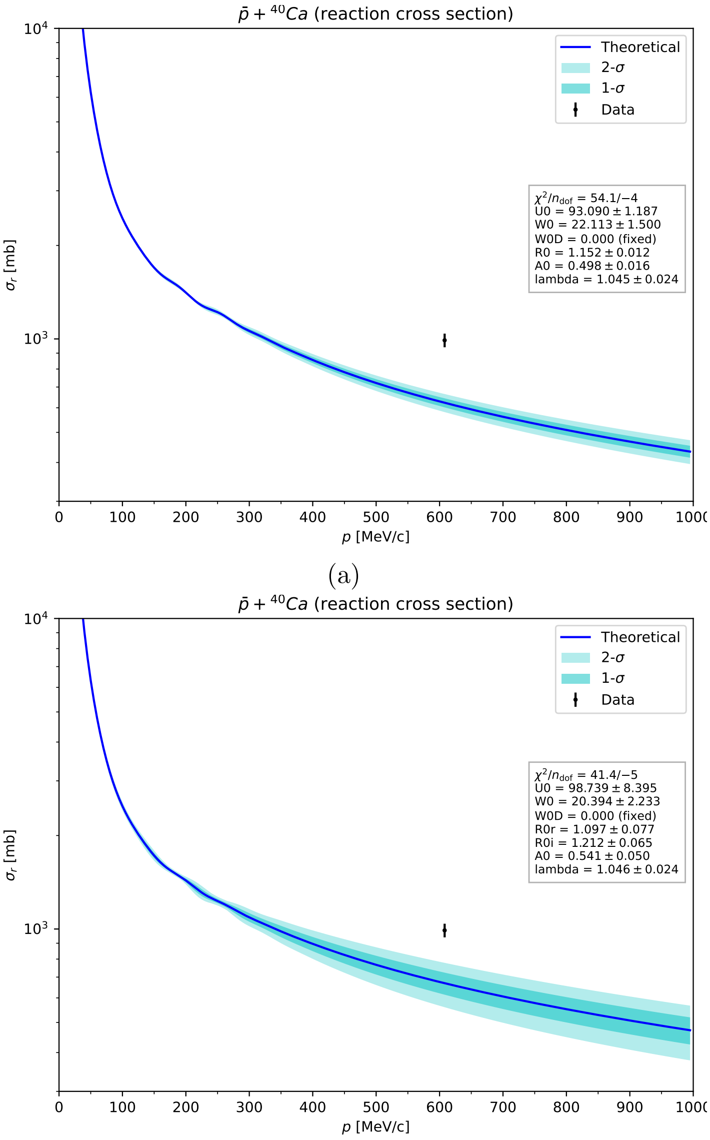

(a)

(b)

Figure 4.9: Theoretical curves of the reaction cross section using best-fit results at 303.3 MeV/c from Table 4.6 for 5- (4.9a) and 6- (4.9b) parameters fits.

p [MeV/c]	$\mathbf{n}_{\text{par}}$	σ_r^{th} [mb]	σ_r^{x} [mb]
303.3	5	1008 ± 16	
	6	1035 ± 35	
	7	—	
608.0	5	874 ± 17	$990 \pm 50^{(*)}$
	6	875 ± 17	
	7	874 ± 20	

(*) $p = 622\,\text{MeV/c}$

Table 4.8: Predicted values of the reaction cross section at for ^{40}Ca, compared with the experimental value in the nearest value of momentum.

oscillations between 100 MeV/c and 300 MeV/c are present. It is difficult to establish something about the quality of these parameters with just one datum for the reaction cross section at $\sim$ 608 MeV/c. The 6-parameter case (Figure 4.9b) shows similar oscillations in the 100–300 MeV/c range.

Another feature of these fits can be seen in Figures 4.10, where the calculation of the reaction cross sections for ^{40}Ca is shown with the datum from Ref. [45]. They agree with the datum at 608 MeV/c, confirming again the possibility that some of the parameters of the optical potential could depend on the momentum of the projectile. The reaction cross section curves do not show the oscillation shown in the 303.3 MeV/c cases, also if the value of W_0 is almost the same as the previous cases. This can be an indication that the higher value of U_0 could be responsible for oscillations in the reaction cross sections at lower momenta.

4.2.4 Lead-208

4.2.4.1 305 MeV/c

The 304.9 MeV/c data [48] are distributed in the range $0° - 40°$ quite homogeneously with $n_{\text{data}} = 19$. The parameter values are summarized in Tables 4.9.

$\mathbf{n}_{\text{par}}$	$\mathbf{U_0}$ [MeV]	$\mathbf{W_0}$ [MeV]	$\mathbf{r}_{0\text{R}}$ [fm]	$\mathbf{r}_{0\text{I}}$ [fm]	$\mathbf{a}_{\text{R}}$ [fm]	$\mathbf{a}_{\text{I}}$ [fm]	λ	$\tilde{\chi}^2$
5	46.5 ± 0.8	11.2 ± 0.8	1.26 ± 0.01	—	0.46 ± 0.03	—	1.19 ± 0.03	4.1
6	276 ± 17	10.4 ± 0.9	0.78 ± 0.04	1.46 ± 0.02	0.42 ± 0.09	—	1.28 ± 0.03	3.6
7	0.3 ± 0.2	22 ± 17	3.9 ± 0.3	1.3 ± 0.1	2 ± 1	0.6 ± 0.2	1.19 ± 0.06	2.9

Table 4.9: Best-fit parameters for ^{208}Pb at $p = 304.9\,\text{MeV/c}$ ($n_{\text{dof}} = 19 - n_{\text{par}}$). The empty cells are for geometrical parameters forced to be the same in value as the relative one of the real/imaginary part.

The parameter values are very unstable in this case. All fits have reduced χ^2 values around $3 - 4$. Again, this high value of $\tilde{\chi}^2$ is probably due to the narrow range of the angles available for the fitting procedure. Some values of geometrical parameters are outside the expected range for 6-parameter ($r_{0R} < 1\,\text{fm}$) and 7-parameter ($r_{0R} > 1\,\text{fm}$, $a_R > 0.5\,\text{fm}$) fits. These values show that more minima exist for these kinds of potentials. However, as mentioned in Chapter 2, we know from

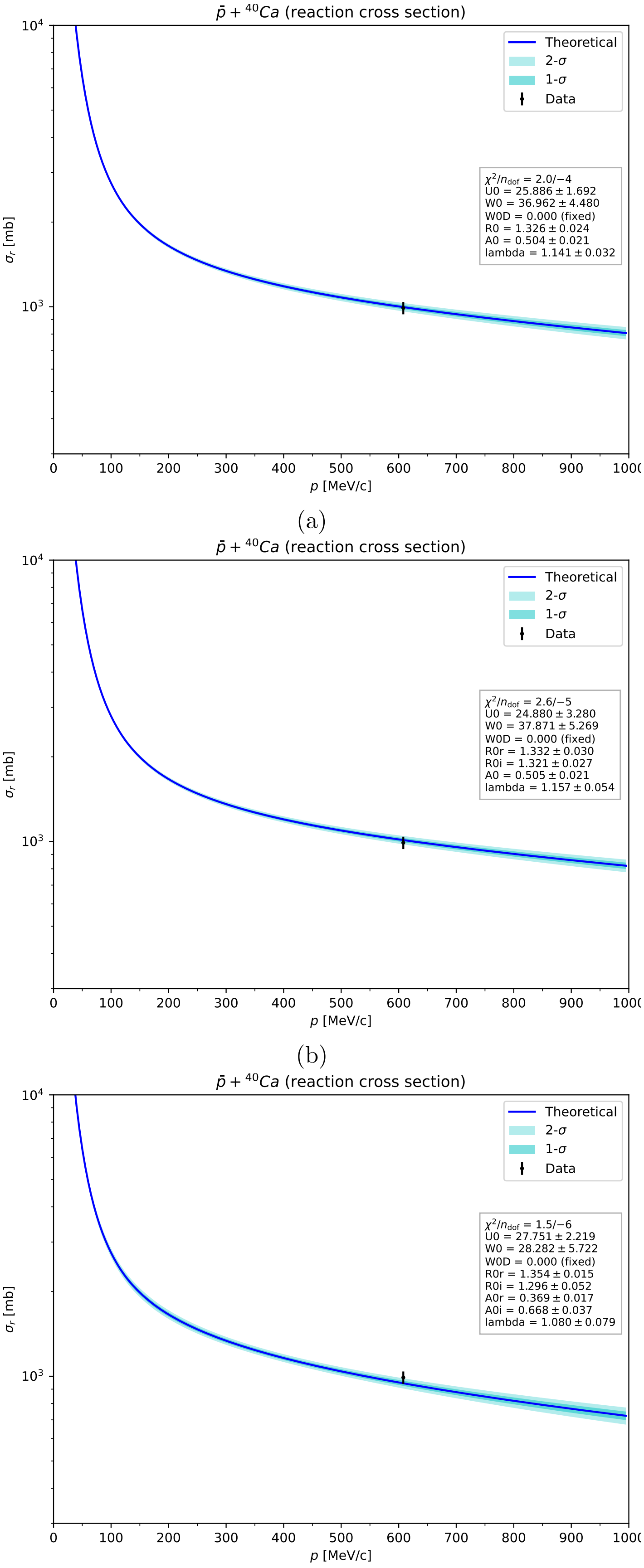

(a)

(b)

(c)

Figure 4.10: Theoretical curves of the reaction cross section using best-fit results at 608 MeV/c from Table 4.7 for 5- (4.10a), 6- (4.10b) and 7- (4.10c) parameters fits.

measurements and estimations which range the geometrical parameters should have. Therefore, we can exclude that, for example, in this case, the 6- and 7-parameter fits are reliable, despite the value of their reduced χ^2. The results in Table 4.9 are the best ones for 304.9 MeV/c fits. Many tries have been made to obtain better results, trying different initial values to explore different regions; however, the results did not converge or the fits give anomalous values of the parameters with higher $\tilde{\chi}^2$.

In Figures 4.11 the results of these fits are shown with data from Ref. [48]. The theoretical curves seem to follow the behavior of the data quite well, with some exceptions around $5° - 10°$, $20°$ and $30°$. The data however cover just a part of the oscillation region and also are not in the neighborhood of the pronounced minima of the diffraction pattern (except for the minimum at $\sim 30°$).

No noticeable difference can be found between the three fits, apart from the 7-parameter curve which seems to pass nearer to the majority of the data – except for the smallest-angle one. However, as we previously commented, this last fit is not reliable.

4.2.4.2 609 MeV/c

The 609 MeV/c data are distributed in the range $0° - 40°$ quite homogeneously with $n_{\text{data}} = 40$ and they are from Ref. [45] (see Figure 4.12). The parameter values are summarized in Tables 4.10. Again, for ^{208}Pb we have a variety of possibilities for the optical potential:

$\mathbf{n}_{\text{par}}$	$\mathbf{U_0}$ [MeV]	$\mathbf{W_0}$ [MeV]	$\mathbf{r}_{0\text{R}}$ [fm]	$\mathbf{r}_{0\text{I}}$ [fm]	$\mathbf{a}_{\text{R}}$ [fm]	$\mathbf{a}_{\text{I}}$ [fm]	λ	$\tilde{\chi}^2$
5	14.9 ± 0.7	8 ± 1	1.374 ± 0.008	—	0.39 ± 0.03	—	0.82 ± 0.06	8.1
6	5.4 ± 0.4	13.1 ± 0.8	1.57 ± 0.03	1.396 ± 0.009	0.37 ± 0.02	—	1.53 ± 0.06	4.9
7	8.1 ± 0.5	8 ± 1	1.393 ± 0.006	1.12 ± 0.03	0.26 ± 0.03	0.5 ± 0.1	1.08 ± 0.07	4.9

Table 4.10: Best-fit parameters for ^{208}Pb at $p = 609$ MeV/c ($n_{\text{dof}} = 40 - n_{\text{par}}$). The empty cells are for geometrical parameters forced to be the same in value as the relative one of the real/imaginary part.

1. "weakly"-absorptive potential ($U_0 > W_0$, 5-parameter)
2. "strongly"-absorptive potential ($U_0 < W_0$, 6-parameter)
3. "equally"-absorptive potential ($U_0 \simeq W_0$, 7-parameter).

All values seem quite reliable and in the expected ranges, apart from a_{0R} of 7-parameter fit, which is a little below the expected 0.5 fm. Moreover, the normalization factor λ in the 5- and 6-parameter fits is respectively a little below and above the value of 1.0 ± 0.1.

The Figures 4.12, together with data from Ref. [48], show another feature. The oscillations of the theoretical curves are quite pronounced (in particular for $\theta > 20°$). However, after 25°, they seem to cross through an "average line" through the oscillations calculated. In $\theta \sim 25°$ there is moreover a "peak" in data that in all calculated curve is not present or at least is shifted slightly forward in angles. Then, the data seems to "flatten" along the "average line" mentioned before. In addition, data at small angles, *i.e.* $\theta \sim 5°$, are above the theoretical line. In the 5-parameter

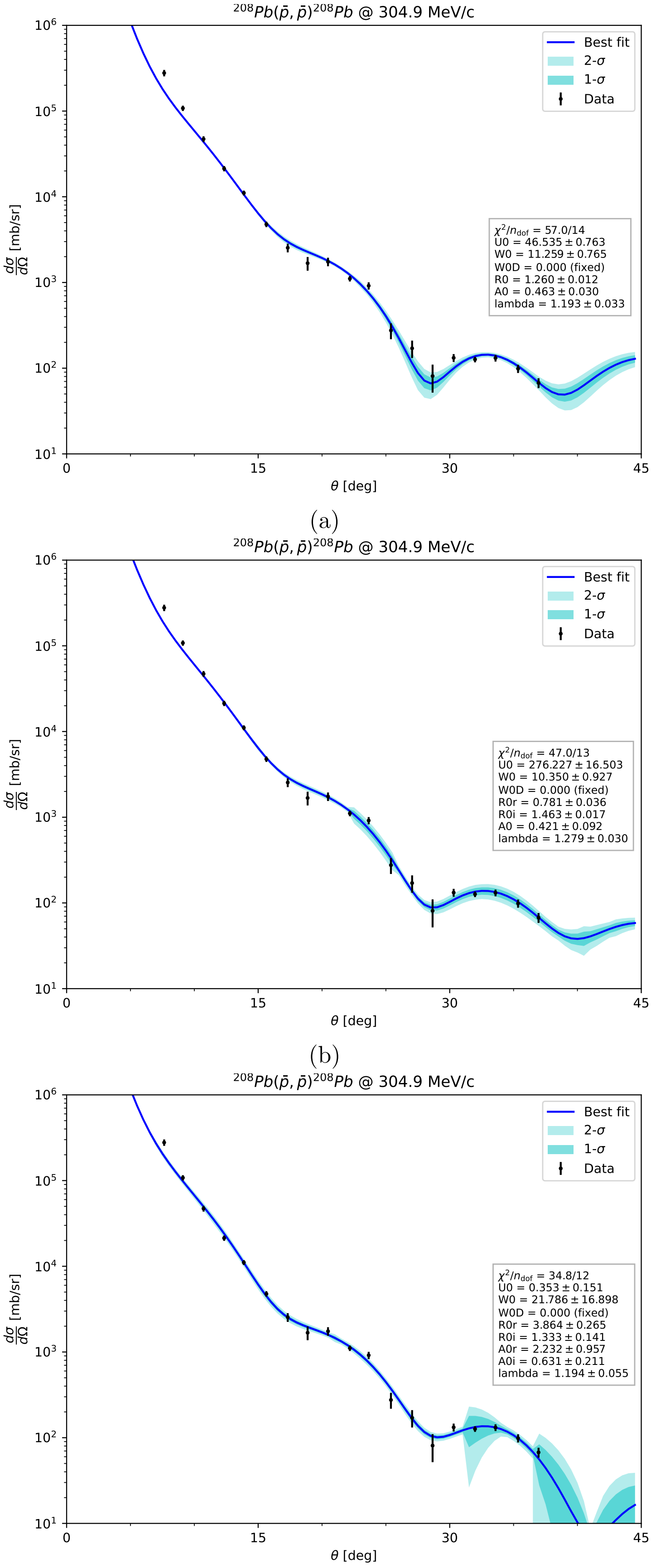

(a)

(b)

(c)

Figure 4.11: 5- (4.11a), 6- (4.11b) and 7- (4.11c) parameters best-fit curve with error bands at 1-σ and 2-σ for ^{208}Pb at $E_{\bar{p}} = 46\,\mathrm{MeV}$[?]($p = 304.9\,\mathrm{MeV/c}$) between $0° - 45°$.

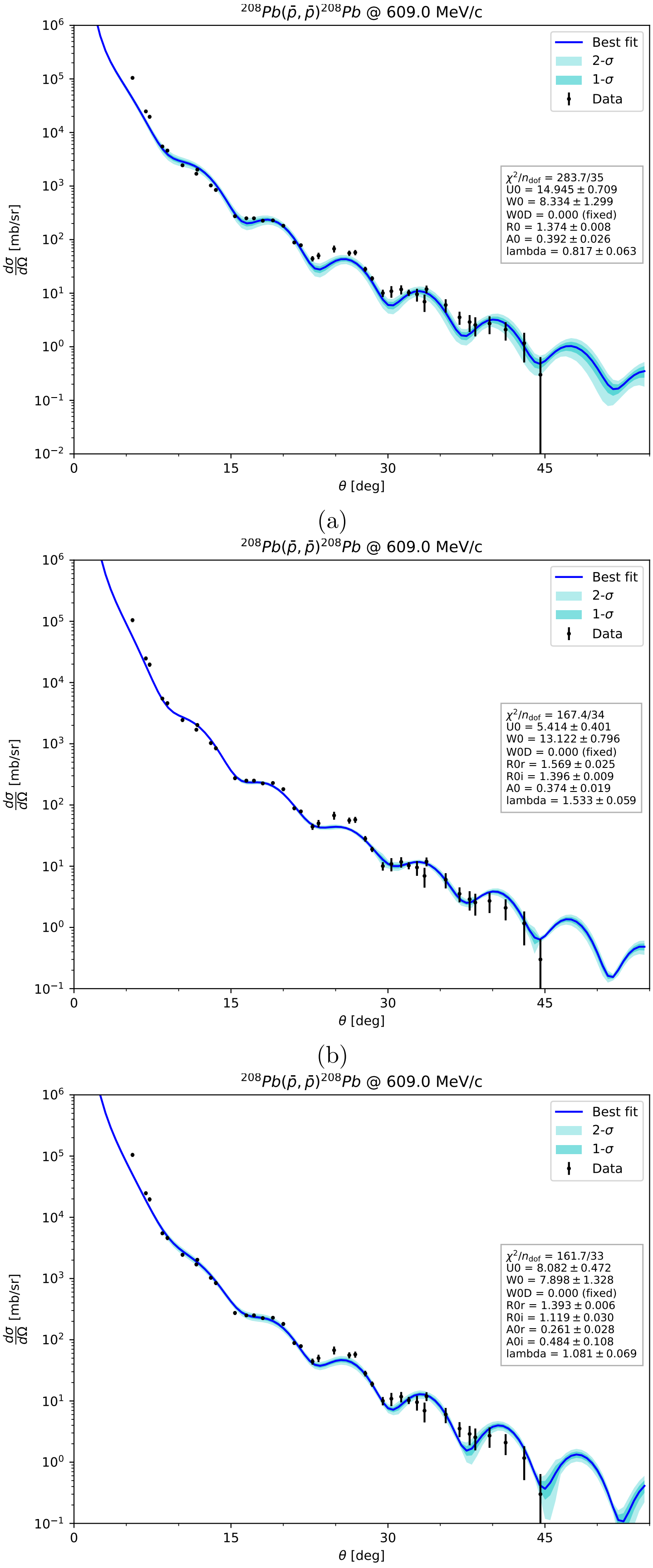

(a)

(b)

(c)

Figure 4.12: 5- (4.12a), 6- (4.12b) and 7- (4.12c) parameters best-fit curve with error bands at 1-σ and 2-σ for ^{208}Pb at $E_{\bar{p}} = 179.8\,\mathrm{MeV}$[?]($p = 609\,\mathrm{MeV/c}$) between $0^\circ - 45^\circ$.

case (Figure 4.12a) the first three data ($\theta \sim 5^\circ - 10^\circ$) are all outside the best-fit line, which explain the higher value in the $\tilde{\chi}^2$ with respect to 6- (Figure 4.12b) and 7-parameter(Figure 4.12c).

4.2.4.3 Reaction cross sections

The previous results, as before, are used to plot the reaction cross sections and compare the behavior with these data. The Figures 4.13 and 4.14 show the theoretical reaction cross sections for antiproton with ^{208}Pb target. The reaction cross section experimental data are from Garreta *et al.* [45] (the central datum at 609 MeV/c) and Ashford *et al.* [51] (the two asides with greater errors).

We also report in Table 4.11 the calculated values of the reaction cross section at 304.9 MeV/c and 609 MeV/c.

p [MeV/c]	$\mathbf{n}_{\text{par}}$	σ_r^{th} [mb]	σ_r^{x} [mb]
304.9	5	2972 ± 42	—
	6	3076 ± 89	
	7	3253 ± 201	
609.0	5	1739 ± 123	$2670 \pm 140^{(*)}$
	6	2120 ± 48	
	7	1053 ± 182	

$^{(*)}p = 609.9$ MeV/c

Table 4.11: Predicted values of the reaction cross section for ^{208}Pb, compared with the experimental value in the nearest value of momentum.

The 5-parameter fit (4.13a) is the best one, both for the $\tilde{\chi}^2$ value and the graphic representation that shows the curve passing near every experimental point. However, we have no data in the region of the elastic scattering momentum (304.9 MeV/c), as in the ^{40}Ca case. In the 6-parameter fit (4.13b) and 7-parameter one (4.13c) the curve passes very close to the 609 MeV/c datum by Garreta *et al.* . In principle, and looking back to the previous targets, this is not expected since the fits were done on a different momentum for differential elastic scattering cross section and we see that in all previous cases, we obtained results depending on momentum. Despite that, the other two data are quite far from the theoretical prediction with these parameters, also the lowest-momentum one which in principle we expect to better agree with the calculations done with $p = 304.9$ MeV/c (as in Figure 4.13a). Finally, we can observe that the error bands are quite wide for the 7-parameter fit, while in the other two cases are narrower.

The 609 MeV/c fits of ^{208}Pb give different results in reaction cross sections with respect to the other targets. The results seem to be worse than the lower momentum fits. The Garreta datum is far away from the curve, while the Ashford ones for the 5- and 7-parameter seem to be nearer. The 6-parameter fit, which is the "strongly"-absorptive one, overestimates the reaction cross section data.

In general, for ^{208}Pb the results are worse than for other targets. A possible explanation of this behavior could be possible surface effects of such a heavy nucleus, or other effects due to the high number of nucleons in the nucleus. Another possibil-

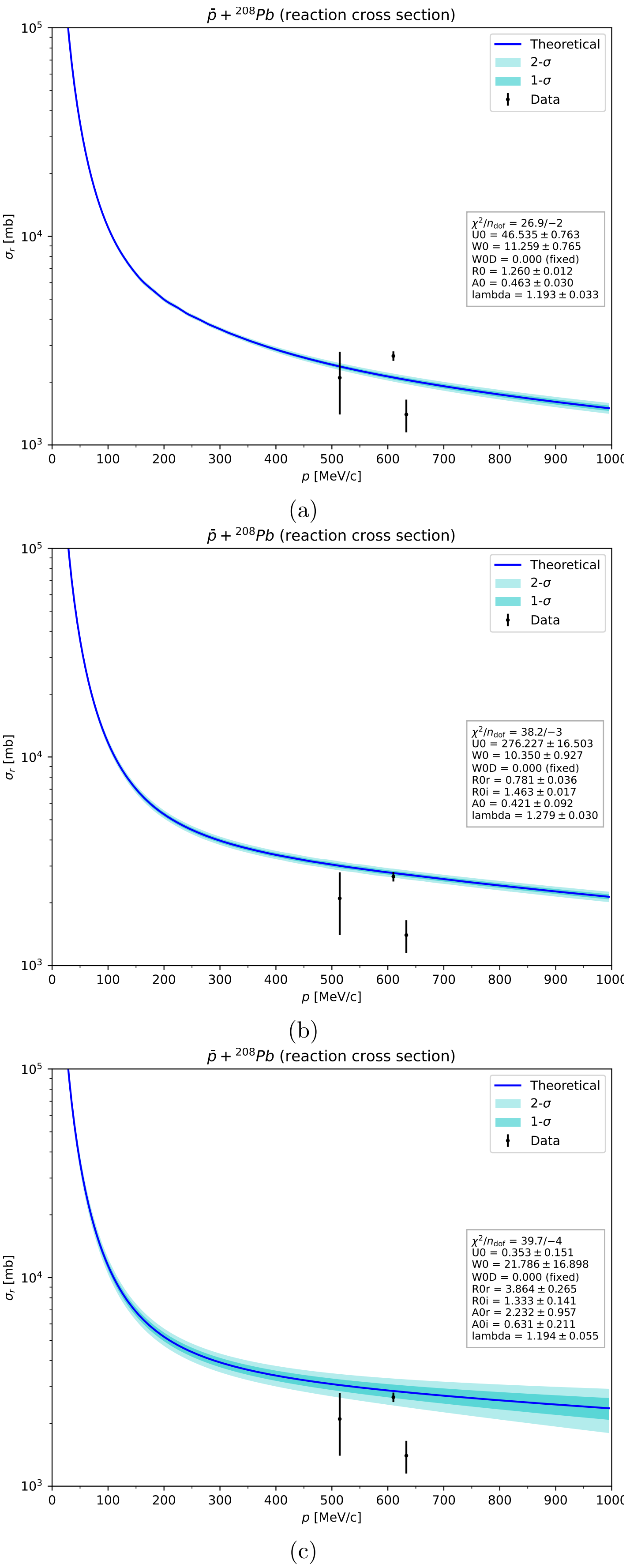

Figure 4.13: Theoretical curves of the reaction cross section using best-fit results at 304.9 MeV/c from Table 4.9 for 5 (4.13a), 6 (4.13b) and 7 (4.13c) parameters fits.

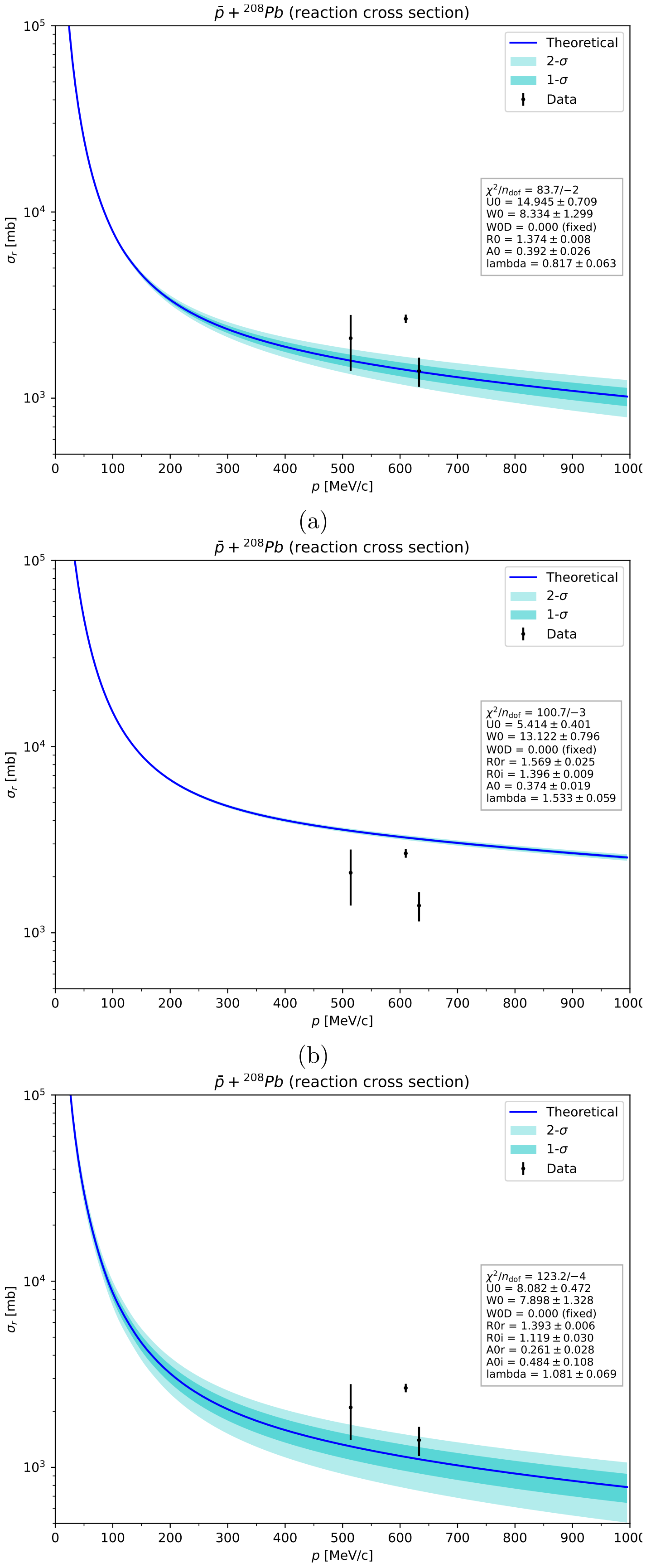

Figure 4.14: Theoretical curves of the reaction cross section using best-fit results at 609 MeV/c from Table 4.10 for 5 (4.14a), 6 (4.14b) and 7 (4.14c) parameters fits.

ity is the failure of the sphericity assumption of the nucleus. However, experimental evidence of the validity of the spherical approximation for ^{208}Pb exists.

4.3 Summary

We determined the best values of the parameters for a Woods-Saxon-shaped optical potential to describe differential elastic scattering and reaction cross sections of antiprotons on four different targets (^{12}C, ^{16}O, ^{40}Ca, ^{208}Pb). Data are from the experiments listed in Chapter 3, Section 3.1. We compared fits with different numbers of free parameters (5, 6, and 7) considering always W_{0D}, the surface absorption term, fixed to zero. In general, for the differential cross section of antiproton elastic scattering, good fits were obtained using the χ^2 minimization, with the addition of a pull term for the normalization parameter λ. Better convergence and precision were obtained for the highest momenta data ($p \sim 600\,\mathrm{MeV/c}$) while the lowest momenta results ($p \sim 300\,\mathrm{MeV/c}$) were slightly worse. In all targets, the 5-parameter Woods-Saxon shape seems to reproduce quite well the experimental data, with some exceptions with slightly better $\tilde{\chi}^2$ for 6- and 7-parameter cases. However, in the majority of cases, the fits with different numbers of parameters are quite indistinguishable by eye – apart from the error bands. The difficulty in convergence seems to be more probable for targets with the highest A values and low-momentum projectiles.

The direct fit to antiproton-nuclei reaction data was too difficult to achieve, due to the scarce measurements present in literature. Therefore, we opted to calculate the theoretical curves for the reaction cross sections. We assumed the parameters to be independent of the momentum of the projectile. The parameters seem to have quite good agreement with data of the reaction cross section. However, this is valid only when the used fit parameters are the ones obtained at energies near those reaction cross section values used for comparisons. If the parameters used are for a different momentum, they do not give the correct value of the reaction cross section near the experimental values. This fact is possible evidence for the dependence on the momentum of the projectile of at least one of the fitting parameters. For low-momentum fits ($p \sim 300\,\mathrm{MeV/c}$) the calculated reaction cross sections seem to underestimate the experimental value for both the highest and lowest values of the momentum. For high-momentum fits ($p \sim 600\,\mathrm{MeV/c}$) the data above this value are very close to the experimental values, while a consistent difference is present for the data below.

In all these cases, no precise family of optical potential, *i.e.* strongly or weakly absorptive, can be excluded. In many cases, we obtained equally satisfying fits using both families.

Chapter 5

Discussion

In the previous chapter, we presented the results, without giving them a proper interpretation. This chapter is dedicated to a deeper discussion of the results obtained through the fit to data and to some of the consequences of such results. In particular, the focus is on the values of the optical potential parameters and their change depending on different factors. Moreover, brief comments on correlation factors are present. Correlation factors are indispensable in multi-variable fitting, providing insights into inter-variable relationships and aiding in identifying issues like multi-collinearity. They contribute to the interpretation of model coefficients, guide variable selection, and play a crucial role in checking assumptions.

5.1 Validation of the theoretical model and the fit procedure

To make proper comments and a complete discussion about data and results, we need a validation of our fitting method. Known methods and algorithms, used in many international research facilities and with complete documentation available online, have been applied. However, the code must be checked to ensure it is working properly, without any errors. Moreover, the `FORTRAN77` code used for the calculation, as mentioned in Chapter 3, was modified many times over the years, and therefore a verification of its operation is due.

To achieve that, random points (from here on, *pseudo-data*) were generated following the theoretical curve calculated using fixed values of the parameters. In that way, the parameter values are under control to check for the fitting procedure to work correctly and if the parameters are in a good neighborhood of the true values. Moreover, the dependence of the fit on some variables in the data available is studied. In particular, this analysis focuses on these aspects:

- the number of data
- the range of the data
- the momentum of the projectile.

These factors could play a role in the quality of the fit. If this is true, the interpretation of the fits can be done more clearly, considering the effect of the experimental data characteristics on the fits.

5.1.1 Pseudo-data generation

The pseudo-data are generated using the `PXS-DataGen` program (see Appendix A). This code generates random angles in the user-defined angle range. Then, the sample of angles is used to calculate the cross sections with the given parameter values, as described in Section 3.3.2. Also, random errors are generated to mimic the experimental errors using the following formula:

$$\delta\sigma_i = \sigma(\theta_i)\left|0.05 + 8\times 10^{-3}(\theta_i - 6^\circ)\right| + 10^{-9}\,\text{mb/sr} \tag{5.1}$$

where σ here is the calculated differential elastic scattering cross section and θ_i is the angle generated randomly. The last term is added to avoid zeros in the denominator of the χ^2 calculation. With the formula 5.1, the relative error at $\theta \sim 6^\circ$ is 5 %. In that way, at $\theta \sim 65^\circ$ the error is around 50 %. This reproduces quite fairly the experimental error in the case of ^{12}C at 607.9 MeV/c.

We applied random "noises" on pseudo-data (in 1-σ error range) to simulate possible underestimation of errors and statistical fluctuations. The random data with fluctuations are extracted with a *Gaussian distribution random generator* $G(\mu, \Delta\sigma)$ such that:

$$\sigma'_i = \sigma(\theta_i)\left[1 + G\left(0, \frac{\delta\sigma_i}{2}\right)\right] \tag{5.2}$$

where $\mu = 0$ and $\Delta\sigma = \delta\sigma_i/2$.

All pseudo-data used for the validation of the fitting procedure were generated with the following parameter values:

- $U_0 = 50\,\text{MeV},\ W_0 = 100\,\text{MeV},\ W_{0D} = 0$
- $r_{0R} = r_{0I} = 1.1\,\text{fm}$ (5-parameter);
  $r_{0R} = 1.1\,\text{fm},\ r_{0I} = 1.3\,\text{fm}$ (6-/7-parameter)
- $a_R = a_I = 0.5\,\text{fm}$ (5-/6-parameter);
  $a_R = 0.6\,\text{fm},\ a_I = 0.5\,\text{fm}$ (7-parameter)
- $\lambda = 1.0$

We used the following momentum values:

- 300 MeV/c
- 600 MeV/c.

These values are near the ones of the available elastic scattering data for most of the targets we used in the analysis. The validation is done only on ^{12}C target, since is the most interesting of our cases, with more data available in both elastic scattering and reaction cross sections and with a larger range in angles.

5.1.2 Fitting to pseudo-data

The same methods and codes reported in Chapter 3 and 4 have been used.

The number of samples and ranges used in the validation are the following:

- 20 samples between $5^\circ - 35^\circ$ (first rows of the Figures 5.1 to 5.6)

- 20 samples between 5° − 65° (second rows of the same figures above)
- 40 samples between 5° − 65° (third rows of the same figures above)

The generated pseudo-data are in the same ranges as the available experimental data and in similar amounts.

In Figures 5.1. 5.2 and 5.3 some examples of fitting to the pseudo-data at 300 MeV/c are shown. In Figures 5.4. 5.5 and 5.6 fits of the pseudo-data at 600 MeV/c are reported.

Generated Data Parameters								
θ	U_0	W_0	r_{0R}	r_{0I}	a_R	a_I	λ	χ^2/n_{dof}
—	50.0	100.0	1.1	—	0.5	—	1.0	—
Fit Results								
5–35	85 ± 130	141 ± 142	1.0 ± 0.5	—	0.5 ± 0.2	—	1.0 ± 0.1	0.14
	23 ± 23	44 ± 27	1.2 ± 0.5	1.4 ± 0.2	0.5 ± 0.1	—	1.00 ± 0.09	0.16
	132 ± 9	42 ± 21	1.34 ± 0.02	1.0 ± 0.4	0.17 ± 0.08	0.0 ± 6	1.00 ± 0.09	0.15
5–65	92 ± 93	137 ± 138	1.0 ± 0.4	—	0.52 ± 0.05	—	0.97 ± 0.07	0.19
	158 ± 112	36 ± 37	0.6 ± 0.3	1.3 ± 0.4	0.55 ± 0.07	—	0.97 ± 0.07	0.19
	193 ± 194	31 ± 32	0.5 ± 0.6	1.4 ± 0.4	0.6 ± 0.2	0.53 ± 0.15	0.97 ± 0.09	0.20
5–65	46 ± 47	262 ± 231	0.9 ± 0.2	—	0.53 ± 0.04	—	1.07 ± 0.03	0.23
	25 ± 16	620 ± 224	1.4 ± 0.2	0.79 ± 0.08	0.45 ± 0.04	—	1.02 ± 0.03	0.22
	23 ± 12	598 ± 196	1.5 ± 0.2	0.80 ± 0.07	0.4 ± 0.2	0.45 ± 0.03	1.03 ± 0.04	0.23

Table 5.1: Table with results of the fits to pseudo-data generated using the 5-parameter model at 300 MeV/C with 5-, 6-, and 7-parameter fits.

Generated Data Parameters								
θ	U_0	W_0	r_{0R}	r_{0I}	a_R	a_I	λ	χ^2/n_{dof}
—	50.0	100.0	1.1	1.3	0.5		1.0	—
Fit Results								
5-35	385 ± 178	966 ± 337	0.80 ± 0.08	—	0.49 ± 0.03	—	1.00 ± 0.02	0.23
	561 ± 323	1209 ± 518	0.7 ± 0.1	0.75 ± 0.09	0.49 ± 0.03	—	1.00 ± 0.02	0.24
	336 ± 193	719 ± 298	0.6 ± 0.1	0.90 ± 0.09	0.60 ± 0.07	0.48 ± 0.04	1.00 ± 0.02	0.26
5-65	3868 ± 1576	4970 ± 2023	0.4 ± 0.1	—	0.50 ± 0.02	—	0.95 ± 0.03	0.29
	11 ± 9	108 ± 38	1.5 ± 0.2	1.32 ± 0.09	0.48 ± 0.05	—	0.99 ± 0.03	0.18
	1763 ± 1166	1925 ± 709	0.6 ± 0.1	0.5 ± 0.1	0.42 ± 0.04	0.54 ± 0.04	0.99 ± 0.03	0.19
5-65	4206 ± 1145	5936 ± 1174	0.31 ± 0.07	—	0.51 ± 0.03	—	0.98 ± 0.03	0.39
	1066 ± 567	1078 ± 260	0.6 ± 0.1	0.69 ± 0.05	0.51 ± 0.02	—	0.98 ± 0.03	0.40
	4206 ± 2184	431 ± 51	0.52 ± 0.05	0.68 ± 0.04	0.43 ± 0.01	0.60 ± 0.02	0.98 ± 0.05	0.36

Table 5.2: Table with results of the fits to pseudo-data generated using the 6-parameter model at 300 MeV/C with 5-, 6-, and 7-parameter fits.

Generated Data Parameters								
θ	U_0	W_0	r_{0R}	r_{0I}	a_R	a_I	λ	χ^2/n_{dof}
—	50.0	100.0	1.1	1.3	0.6	0.5	1.0	—
Fit Results								
5-35	0 ± 30	1163 ± 994	0.5 ± 0.3	—	0.64 ± 0.08	—	1.02 ± 0.05	0.20
	0.1 ± 0.2	634 ± 390	6 ± 2	0.7 ± 0.2	0.61 ± 0.06	—	0.99 ± 0.05	0.18
	42 ± 174	52 ± 53	1 ± 1	1.4 ± 0.7	0 ± 7	0.6 ± 0.3	1.00 ± 0.09	0.25
5-65	10 ± 2	46 ± 3	1.51 ± 0.02	—	0.49 ± 0.02	—	1.00 ± 0.03	0.20
	13 ± 6	76 ± 5	1.4 ± 0.1	1.34 ± 0.02	0.53 ± 0.02	—	1.00 ± 0.03	0.21
	20 ± 7	129 ± 9	1.51 ± 0.09	1.12 ± 0.02	0.31 ± 0.08	0.59 ± 0.02	1.01 ± 0.03	0.24
5-65	143 ± 91	200 ± 85	1.1 ± 0.1	—	0.53 ± 0.04	—	0.95 ± 0.03	0.38
	67 ± 49	583 ± 250	1.3 ± 0.2	0.89 ± 0.09	0.49 ± 0.04	—	0.95 ± 0.03	0.39
	2.0 ± 0.6	44 ± 15	2.5 ± 0.2	1.6 ± 0.1	0 ± 5	0.39 ± 0.07	0.96 ± 0.05	0.38

Table 5.3: Table with results of the fits to pseudo-data generated using the 7-parameter model at 300 MeV/C with 5-, 6-, and 7-parameter fits.

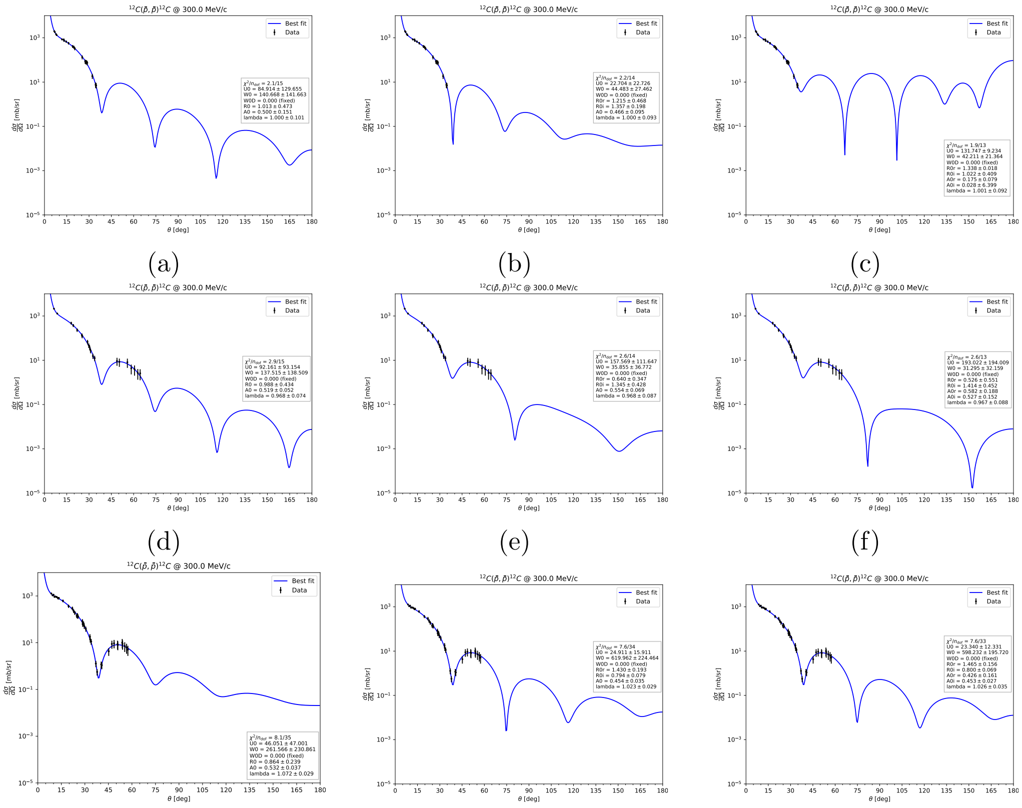

(a) (b) (c)

(d) (e) (f)

(g) (h) (i)

Figure 5.1: Fits to the pseudo-data generated using the 5-parameter model at 300 MeV/C with 5-(5.1a,5.1d,5.1g), 6-(5.1b,5.1e,5.1h), and 7-parameter(5.1c,5.1f,5.1i) fits with 20 samples in $\theta \in (5^\circ - 35^\circ)$ (5.1a,5.1b,5.1c) and $\theta \in (5^\circ - 65^\circ)$ (5.1d,5.1e,5.1f) and 40 samples in $\theta \in (5^\circ - 65^\circ)$ (5.1g,5.1h,5.1i).

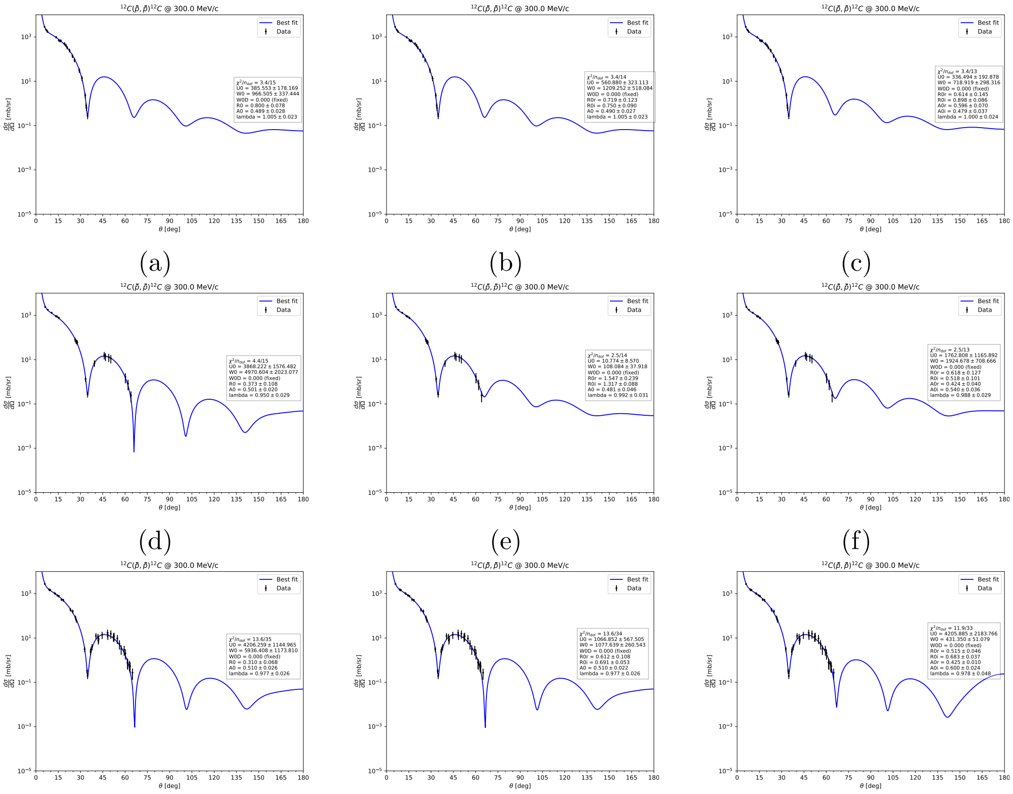

(a) (b) (c)

(d) (e) (f)

(g) (h) (i)

Figure 5.2: Same as Figure 5.1 with pseudo-data generated using the 6-parameter model.

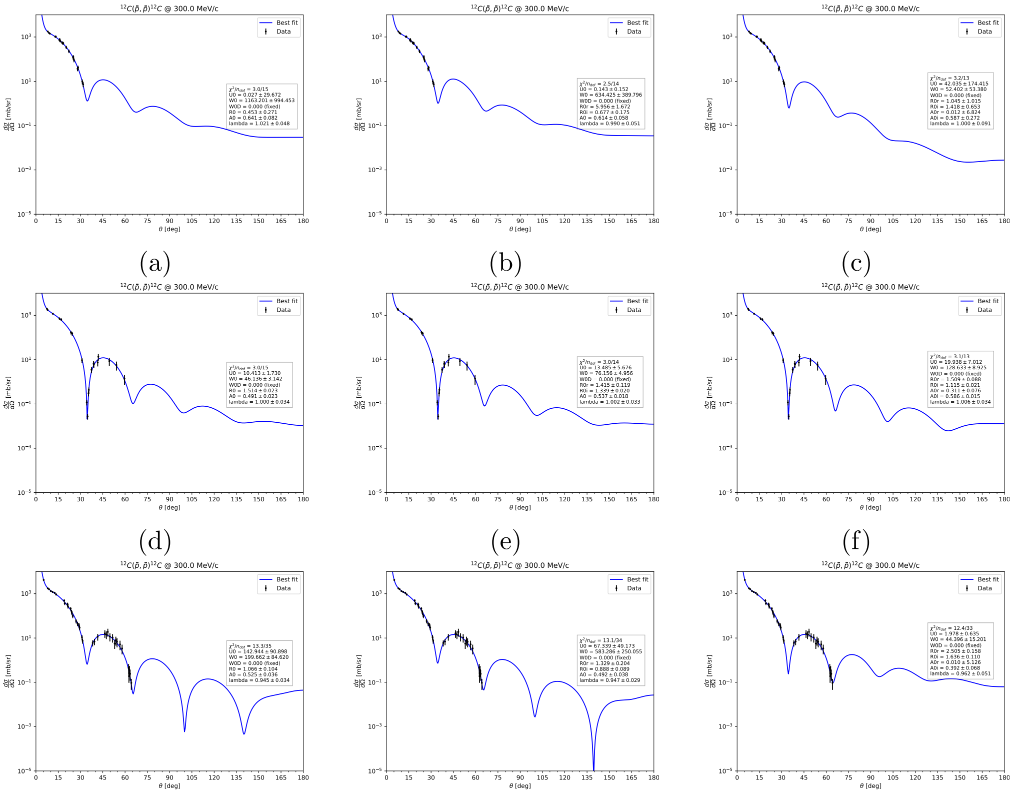

(a) (b) (c)

(d) (e) (f)

(g) (h) (i)

Figure 5.3: Same as Figure 5.1 with pseudo-data generated using the 7-parameter model.

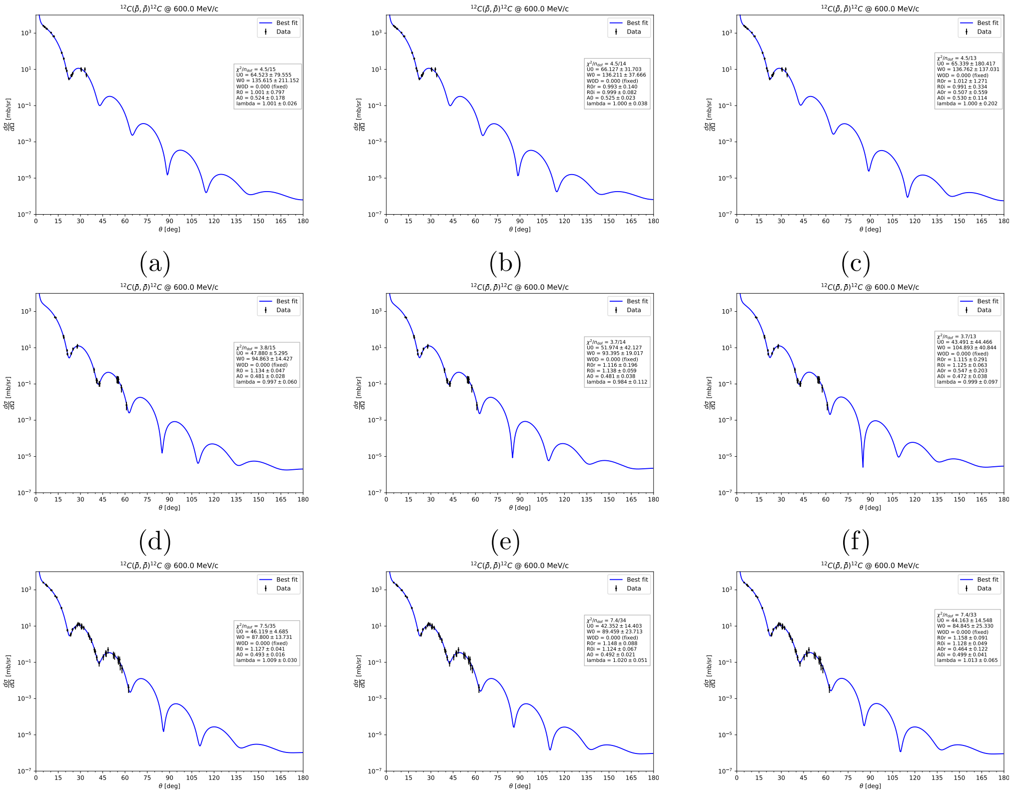

(a) (b) (c)

(d) (e) (f)

(g) (h) (i)

Figure 5.4: Fits to the pseudo-data generated using the 5-parameter model at 600 MeV/C with 5-(5.4a,5.4d,5.4g), 6-(5.4b,5.4e,5.4h), and 7-parameter(5.4c,5.4f,5.4i) fits with 20 samples in $\theta \in (5^\circ - 35^\circ)$ (5.4a,5.4b,5.4c) and $\theta \in (5^\circ - 65^\circ)$ (5.4d,5.4e,5.4f) and 40 samples in $\theta \in (5^\circ - 65^\circ)$ (5.4g,5.4h,5.4i).

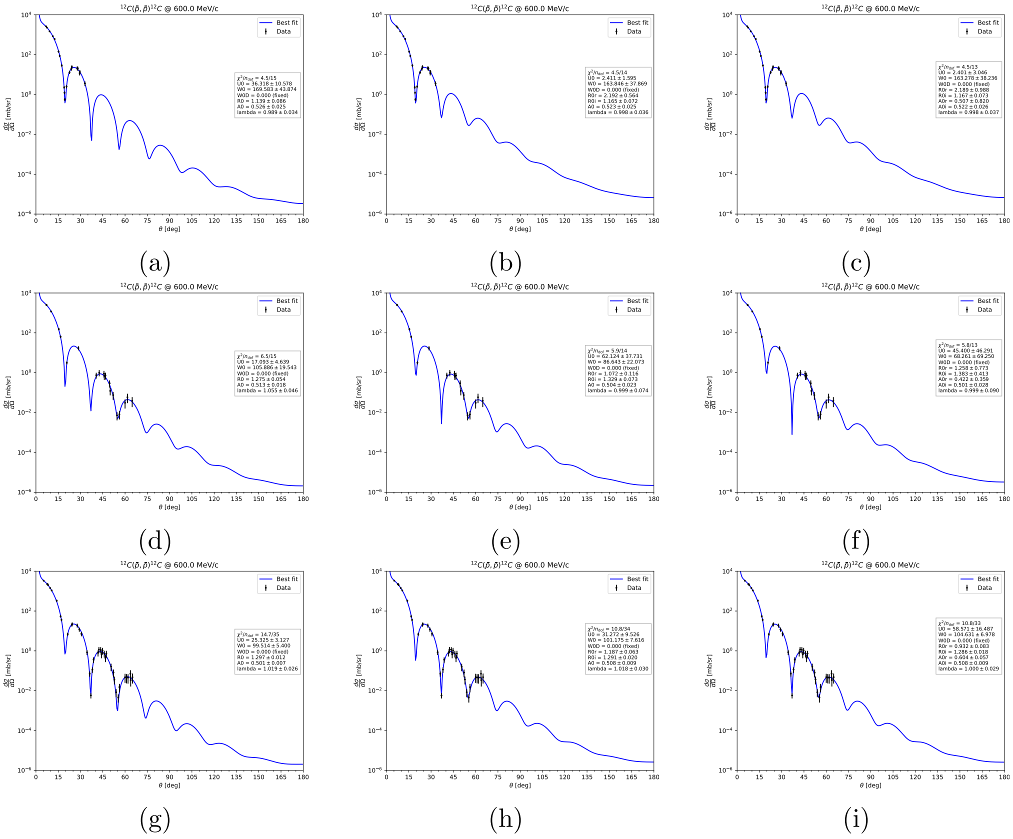

(a) (b) (c)

(d) (e) (f)

(g) (h) (i)

Figure 5.5: Same as Figure 5.4 with pseudo-data generated using the 6-parameter model.

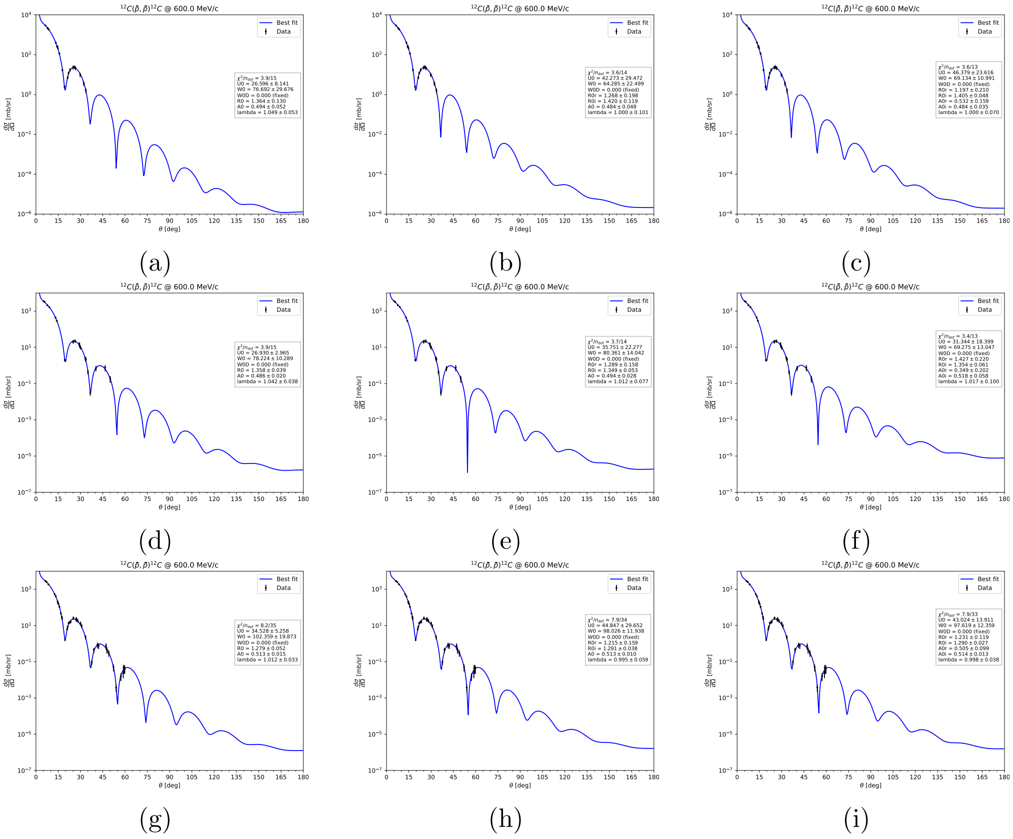

(a) (b) (c)

(d) (e) (f)

(g) (h) (i)

Figure 5.6: Same as Figure 5.4 with pseudo-data generated using the 7-parameter model.

Generated Data Parameters								
θ	U_0	W_0	r_{0R}	r_{0I}	a_R	a_I	λ	χ^2/n_{dof}
—	50.0	100.0	1.1	—	0.5	—	1.0	—
Fit Results								
	64 ± 80	135 ± 211	1.0 ± 0.8	—	0.5 ± 0.2	—	1.00 ± 0.03	0.30
5–35	66 ± 32	136 ± 38	0.99 ± 0.1	1.00 ± 0.08	0.53 ± 0.02	—	1.00 ± 0.04	0.32
	65 ± 180	137 ± 137	1 ± 1	1.0 ± 0.3	0.5 ± 0.6	0.5 ± 0.1	1.0 ± 0.2	0.35
	48 ± 5	95 ± 14	1.13 ± 0.05	—	0.48 ± 0.03	—	1.00 ± 0.06	0.25
5–65	52 ± 42	93 ± 19	1.1 ± 0.2	1.14 ± 0.06	0.48 ± 0.04	—	1.0 ± 0.1	0.26
	43 ± 44	105 ± 41	1.1 ± 0.3	1.1 ± 0.06	0.5 ± 0.2	0.47 ± 0.04	1.0 ± 0.1	0.28
	46 ± 5	88 ± 14	1.13 ± 0.04	—	0.49 ± 0.02	—	1.01 ± 0.03	0.21
5–65	42 ± 14	89 ± 24	1.15 ± 0.09	1.12 ± 0.07	0.49 ± 0.02	—	1.02 ± 0.05	0.22
	44 ± 14	85 ± 25	1.16 ± 0.09	1.13 ± 0.05	0.5 ± 0.1	0.50 ± 0.04	1.01 ± 0.07	0.22

Table 5.4: Table with results of the fits to pseudo-data generated using the 5-parameter model at 600 MeV/C with 5-, 6-, and 7-parameter fits.

Generated Data Parameters								
θ	U_0	W_0	r_{0R}	r_{0I}	a_R	a_I	λ	χ^2/n_{dof}
—	50.0	100.0	1.1	1.3	0.5		1.0	—
Fit Results								
	36 ± 11	170 ± 44	1.14 ± 0.09	—	0.53 ± 0.03	—	0.99 ± 0.03	0.30
5-35	2 ± 2	164 ± 38	2.2 ± 0.6	1.17 ± 0.07	0.52 ± 0.03	—	1.00 ± 0.04	0.32
	2 ± 3	163 ± 38	2 ± 1	1.17 ± 0.07	0.5 ± 0.8	0.52 ± 0.03	1.00 ± 0.04	0.35
	17 ± 5	106 ± 20	1.28 ± 0.05	—	0.51 ± 0.02	—	1.06 ± 0.05	0.43
5-65	62 ± 38	87 ± 22	1.1 ± 0.1	1.33 ± 0.07	0.50 ± 0.02	—	1.00 ± 0.07	0.42
	45 ± 46	68 ± 69	1.3 ± 0.8	1.4 ± 0.4	0.4 ± 0.4	0.50 ± 0.03	1.00 ± 0.09	0.45
	25 ± 3	100 ± 5	1.30 ± 0.01	—	0.501 ± 0.007	—	1.02 ± 0.03	0.42
5-65	31 ± 10	101 ± 8	1.19 ± 0.06	1.29 ± 0.02	0.508 ± 0.009	—	1.02 ± 0.03	0.32
	59 ± 16	105 ± 7	0.93 ± 0.08	1.3 ± 0.02	0.60 ± 0.06	0.508 ± 0.009	1.00 ± 0.03	0.33

Table 5.5: Table with results of the fits to pseudo-data generated using the 6-parameter model at 600 MeV/C with 5-, 6-, and 7-parameter fits.

Generated Data Parameters								
θ	U_0	W_0	r_{0R}	r_{0I}	a_R	a_I	λ	χ^2/n_{dof}
—	50.0	100.0	1.1	1.3	0.6	0.5	1.0	—
Fit Results								
	27 ± 8	77 ± 30	1.4 ± 0.1	—	0.49 ± 0.05	—	1.05 ± 0.05	0.26
5-35	42 ± 29	64 ± 22	1.3 ± 0.2	1.4 ± 0.1	0.48 ± 0.05	—	1.0 ± 0.1	0.26
	46 ± 23	69 ± 11	1.2 ± 0.2	1.41 ± 0.05	0.5 ± 0.2	0.48 ± 0.04	1.00 ± 0.07	0.28
	27 ± 3	78 ± 10	1.36 ± 0.04	—	0.49 ± 0.02	—	1.04 ± 0.04	0.26
5-65	36 ± 22	80 ± 14	1.3 ± 0.2	1.35 ± 0.05	0.49 ± 0.03	—	1.01 ± 0.08	0.26
	31 ± 18	69 ± 13	1.4 ± 0.2	1.35 ± 0.06	0.4 ± 0.2	0.52 ± 0.06	1.0 ± 0.1	0.26
	35 ± 5	102 ± 20	1.28 ± 0.05	—	0.51 ± 0.02	—	1.01 ± 0.03	0.23
5-65	45 ± 30	98 ± 12	1.2 ± 0.2	1.29 ± 0.04	0.51 ± 0.01	—	1.00 ± 0.06	0.23
	43 ± 14	98 ± 12	1.2 ± 0.1	1.29 ± 0.03	0.5 ± 0.1	0.51 ± 0.01	1.00 ± 0.04	0.24

Table 5.6: Table with results of the fits to pseudo-data generated using the 7-parameter model at 600 MeV/C with 5-, 6-, and 7-parameter fits.

Not all the results are satisfying, and some of them are out of the range of the fixed values or have important errors in the evaluation. In particular, the 300 MeV/c case is imprecise. A different number of parameters used for the fitting procedure with respect to the data generation is expected to lead to worse results. This is partially true, and it can be seen, for example, in the values of χ^2, which is better when the number of parameters used for the fit is the same as the one used for generating the data. However, the values found in the fitting procedure are not always in agreement with the true ones that generated the pseudo-data. This disagreement could be attributed to the fluctuations around the theoretical curve since, as mentioned before, the calculation is very sensible with a minimal change in some parameter values – in particular, the geometrical ones. Another possibility is the ambiguity of this model mentioned in Chapter 2. Probably, there exist many minima of the defined χ^2, and the algorithm, being a local minima search one, cannot explore the others. The discrepancy can also be due to the effect of the initial values for the fitting, which seems to be important to individuate the correct minima. In the present work, the parameters are chosen randomly in a specific range (the ones physically accepted) to not have the same initial values, so that the algorithm is free from the user choice. Nonetheless, the results did not quite change.

Another aspect that seems important in the fitting is the distribution of the data. In the previous chapter, the homogeneity of the data distribution in the angles was highlighted in every fit. However, what seems to affect the fit quality is the range where the data are distributed.

First, in Figure 5.1, the first row has data in the narrower range in angle. These data cover a part of the curve and do not see the oscillations of the pattern. Therefore, the obtained results are far from being clear and precise about the values of the parameters. Wider ranges, like the second row of the plots, give better results. However, the third row seems to give worse results sometimes. This effect could be attributed to the proximity or overlapping of data in some points – a feature present also in some experimental data. Data were generated randomly to not choose peculiar points, but no attention was paid to this overlapping problem.

We can conclude that the fitting procedure seems to work satisfyingly on 600 MeV/c pseudo-data, determining the parameter values that generated the pseudo-data quite well. On the contrary, the 300 MeV/c case seems to give some problems, finding very different minima far away from the original values. Therefore, we expect that results for the lowest momentum are less reliable than the ones with the highest momentum.

5.2 Discussion of the results

The results showed in Chapter 4, in the light of the verification made in the previous section, show us some important features of the WSOP. As already commented in that chapter. we see that changing the momentum of the projectile, no value of the parameters remains constant. In particular, this is clearly shown by the reaction cross section estimations, calculated assuming the constancy of the WSOP parameters. This behavior can be explained if we suppose one (or more) of the parameters to be energy-dependent, and therefore, they need some sort of functional dependence of the energy (or equivalently momentum) of the projectile. In the Lee and Wong work [36], one of the parameters of the Woods-Saxon model (U_0) was considered momentum-dependent. However, that model was exclusively applied to annihilation cross sections and mainly to antineutron data.

In the present thesis, no conclusion can be made about the functional form or propose an alternative to the Lee and Wong one. Our observations are limited to the variations of the values of the parameters of the optical potential in the two projectile momentum we have available (around 300 MeV/c and 600 MeV/c).

The parameters values for 5-, 6- and 7-parameters fits for ^{12}C at the mentioned momentum values are plotted in Figures 5.7a, 5.7b and 5.7c.

In the ^{12}C fits we can see that the real and imaginary strengths rise with the increase of the projectile momentum. In particular, W_0 seems to have a rapid increase passing from 300 MeV/c to 608 MeV/c, while the "slope" of U_0 is lower. Moreover,

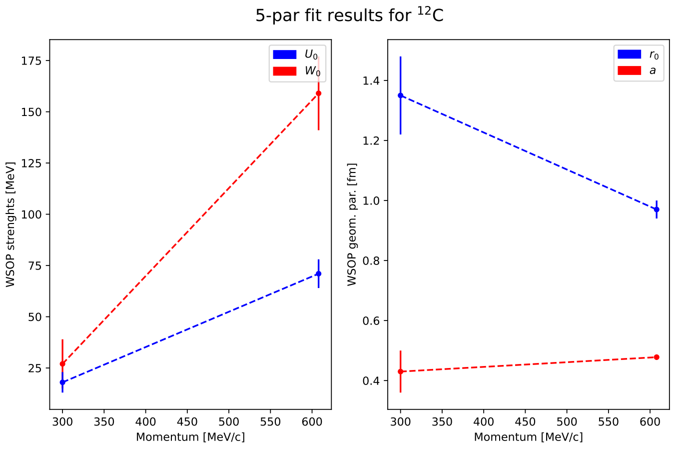

(a)

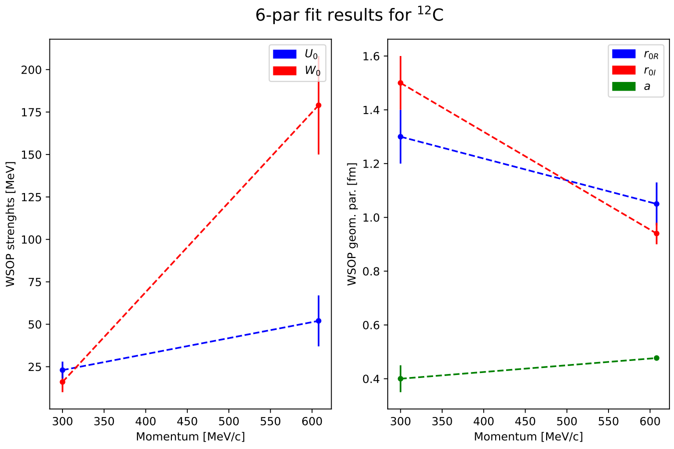

(b)

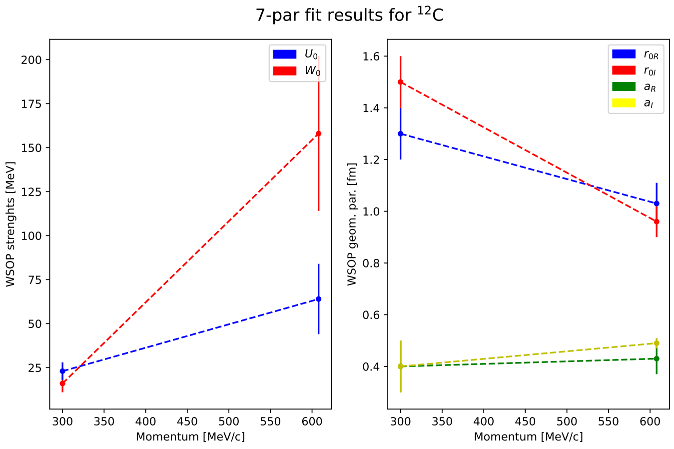

(c)

Figure 5.7: 5- (5.7a), 6- (5.7b), and 7- (5.7c)best-fit parameters for the WSOP for ^{12}C. The dashed lines are just for reference.

we can see that in the lower-momentum value $U_0 \gtrsim W_0$; however, in the higher-momentum value, this trend is inverted and $W_0 \gg U_0$. We might expect something different since for lower-momentum projectile we have a higher probability of the projectile being absorbed by the target. Therefore a greater imaginary strength is expected. However, we cannot look only at the strength values without considering the geometrical parameters. The geometrical parameters values (right panels in the figures) seem to be constant (a, a_R, a_I) or slightly decrease (r_0, r_{0R}, r_{0I}). This behavior of the radii may cause an "over-evaluation" of the corresponding strength to "compensate" the effect. In addition, one can notice that these parameters are exactly the opposite concerning the strengths: when the real radius is higher than the imaginary radius, the real strength is lower than the imaginary one, and vice versa. We need also to consider that the diffuseness values, even though they are quite constant with respect to the momentum, may have some effects with small differences since the cross section curves seem to be sensitive to these parameters in particular. To better see this effect, see Supplementary Figures B.9.

Similar features are present for ^{40}Ca and ^{208}Pb targets.

As we stated in the previous chapter, for ^{40}Ca we do not have a 7-parameter fit at 303.3 MeV/c due to failure of convergence. Despite the presence of a 7-parameters fit at 608 MeV/c, we cannot compare the behavior of the parameters at different projectile momentum, therefore we do not plot these values. Instead, we plot the two available 5-parameter fits values (Figures 5.8a and 5.8b) and the 6-parameter ones (Figure 5.8c). In all cases, we notice that U_0 is predominant on W_0 for lower momenta, while for higher momenta the magnitude is inverted, even if the difference in value is slighter than at 303.3 MeV/c. The geometrical parameters in the 5-parameter fit increase with momentum. For r_0 this increase is more rapid and we can notice comparing Figures 5.8a and 5.8b that for U_0 the relation with r_0 observed in the ^{12}C case is still present. Moreover, we can see that for higher values of r_0, we have much lower values for U_0. In the 6-parameters fit, a is constant in momentum, as mentioned in the previous chapter.

For W_0 and r_0 or r_{0I}, the situation is quite the opposite. These parameters seem to be positively correlated and with a similar slope.

The ^{208}Pb cases are similar to the ^{40}Ca ones. As before, in all cases, the potential is a weakly absorptive one in the 300 MeV/c region, while becoming more absorptive at 600 MeV/c. The geometrical parameters in the 5-parameter fit have no sensible changes in momentum. The slightly higher change in the value of r_0 could influence the values since as stated before the shape of the pattern is sensible to the geometrical parameters. The 6-parameters fit is quite constant in momentum for a, r_{0I}, while a non-negligible increase for r_{0R} – around a factor 2 – is present. In this case, a drop in the value of U_0 is correlated to this change in r_{0R}, as observed in the other cases. W_0 is left unvaried with the increase of momentum unless a slight increase, which seems to mirror the slight decrease in r_{0I}. The 7-parameters case has similar behaviors. The main difference is the higher value in a_R, which reflects – together with $r_{0R} \gg 1\,\mathrm{fm}$ – that this is the unique case of ^{208}Pb where $U_0 < W_0$ at 300 MeV/c – not considering the large error of W_0. Moreover, at 300 MeV/c $U_0 \simeq 0$, that represents the only case in our analysis of a *highly absorptive potential.* At 600 MeV/c the situation is more "as expected", with the values in the expected ranges. The real diffuseness (a_{0R}) and the real radius (r_{0R}) drop drastically with respect to the 300 MeV/c, while imaginary diffuseness and radius (a_{0I}, r_{0I}) are

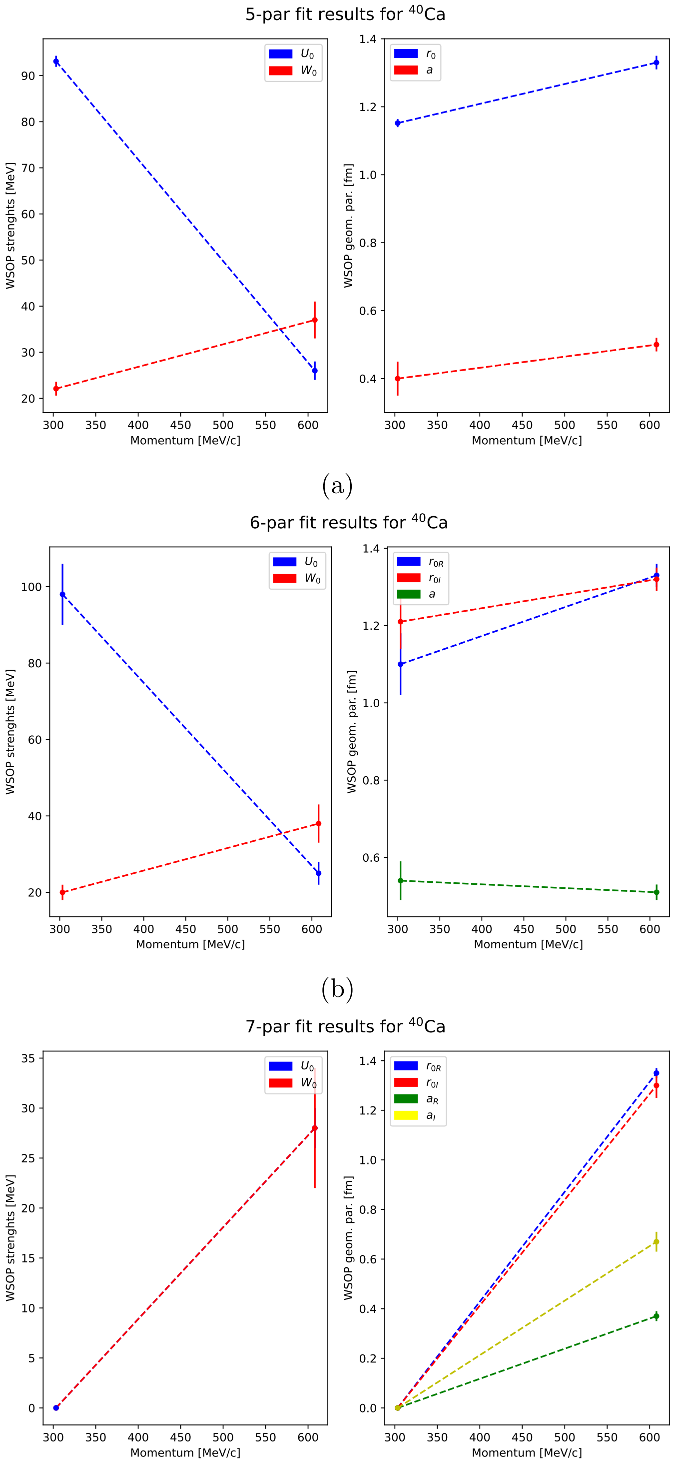

(a)

(b)

(c)

Figure 5.8: Same as Figure 5.7 for ^{40}Ca. Here the 7-parameters case is absent, as specified in Section 4.2.

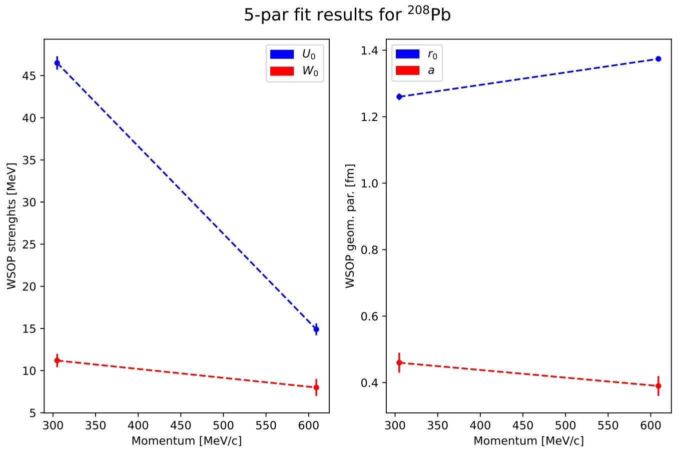

(a)

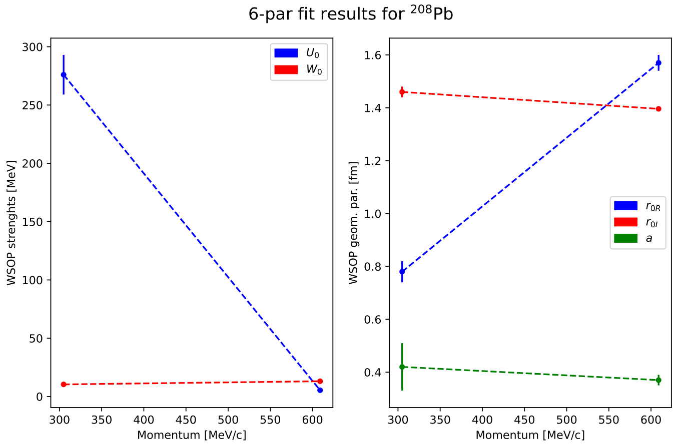

(b)

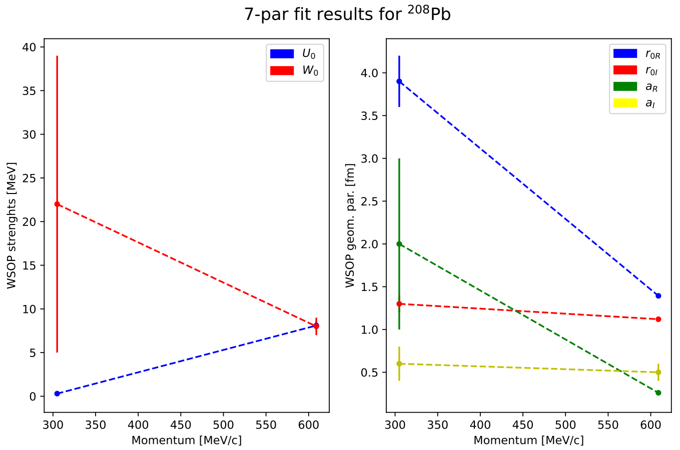

(c)

Figure 5.9: Same as Figure 5.7 for ^{208}Pb.

constant. Around 600 MeV/c $U_0 \simeq W_0$, which is interesting.

It seems, at least in ^{40}Ca and ^{208}Pb cases, that $U_0 \gg W_0$ at 300 MeV/c and $U_0 \gtrsim W_0$ at 600 MeV/c. The diffusenesses are constant in all the analysed cases, apart from ^{208}Pb 7-parameters fit. The radii instead vary their behavior, which however seems to be linked with the increase or decrease of the strengths.

These parameters' behavior can also be analysed by looking at the *correlation factors* of the fits for each target and projectile momentum. The Tables are reported in the Supplementary Tables Appendix C. In Tables C.1, C.2 and C.3 we show the values of these correlation factors for ^{12}C. In Tables C.4, **??** and C.5 the ^{40}Ca data analysis correlation factors are present. Finally, in Tables C.6, C.7 and C.8 the correlations for the ^{208}Pb case are reported.

One can notice immediately that the majority of parameters are correlated to others with strong correlation factors ($|C(p_1, p_2)| > 0.5$), and this is evident in the 5-parameter case, while in 7- and 7-parameters these factors are slightly smaller for some pairs, in particular for 608 MeV/c momentum.

5.3 Low-energy projections

As mentioned in Chapter 1, the main interest of the present work is to study the antiproton-nuclei interactions at low-energy regime, which is poorly explored both experimentally and theoretically. To study these interactions, measurements of the processes cross section for antiproton below 50 MeV (∼300 MeV/c) must be performed. However, going too low in the projectile energy can hide the nuclear interaction effects on cross section measurements, since the Coulomb contribution becomes dominant and all the nuclear diffraction patterns disappear. This condition does not give useful information about the interactions. Projections at low energies can help to understand which is the projectile lowest energy necessary to see measurable nuclear interaction effects. The parameters are assumed independent from momentum, despite, as previously stated, this is probably not the case.

The predictions are calculated for 10, 20, 50, 100, 200, 300 and 600 MeV/c (kinetic energy: 0.05, 0.2, 1.3, 5.3, 21.1, 46.8 and 175.4 MeV). The 300 MeV/c parameters are used as reference. In addition, we have used also the 600 MeV/c case just for comparison. Figures 5.10, 5.11, 5.12 and 5.13 show the projections at the momenta listed above.

We can notice two main features that all the projections have in common:

1. below 50 MeV/c the differential elastic scattering cross section is very similar in behavior and values to the Rutherford one (see the dashed curves in Figures 5.10 to 5.13)

2. the 300 MeV/c fits (Figures 5.10a, 5.12a and 5.13a) show very irregular patterns for large angles ($\theta \gtrsim 90^\circ$) and high momenta ($p > 300$ MeV/c).

The second item above could be simply because the 300 MeV/c fits are used at higher momenta; therefore, as seen previously, the calculations are not precise. Using the 600 MeV/c best-fit values and plot the calculated curve on 300 MeV/c the results for ^{12}C are quite fair ($\tilde{\chi}^2 \sim 4.6 - 5.6$). This is not the case for ^{40}Ca ($\tilde{\chi}^2 \sim 20 - 40$) and ^{208}Pb ($\tilde{\chi}^2 \sim 20 - 30$), also improving the results tuning the values of λ (since it is a normalization which in principle could vary changing the fit).

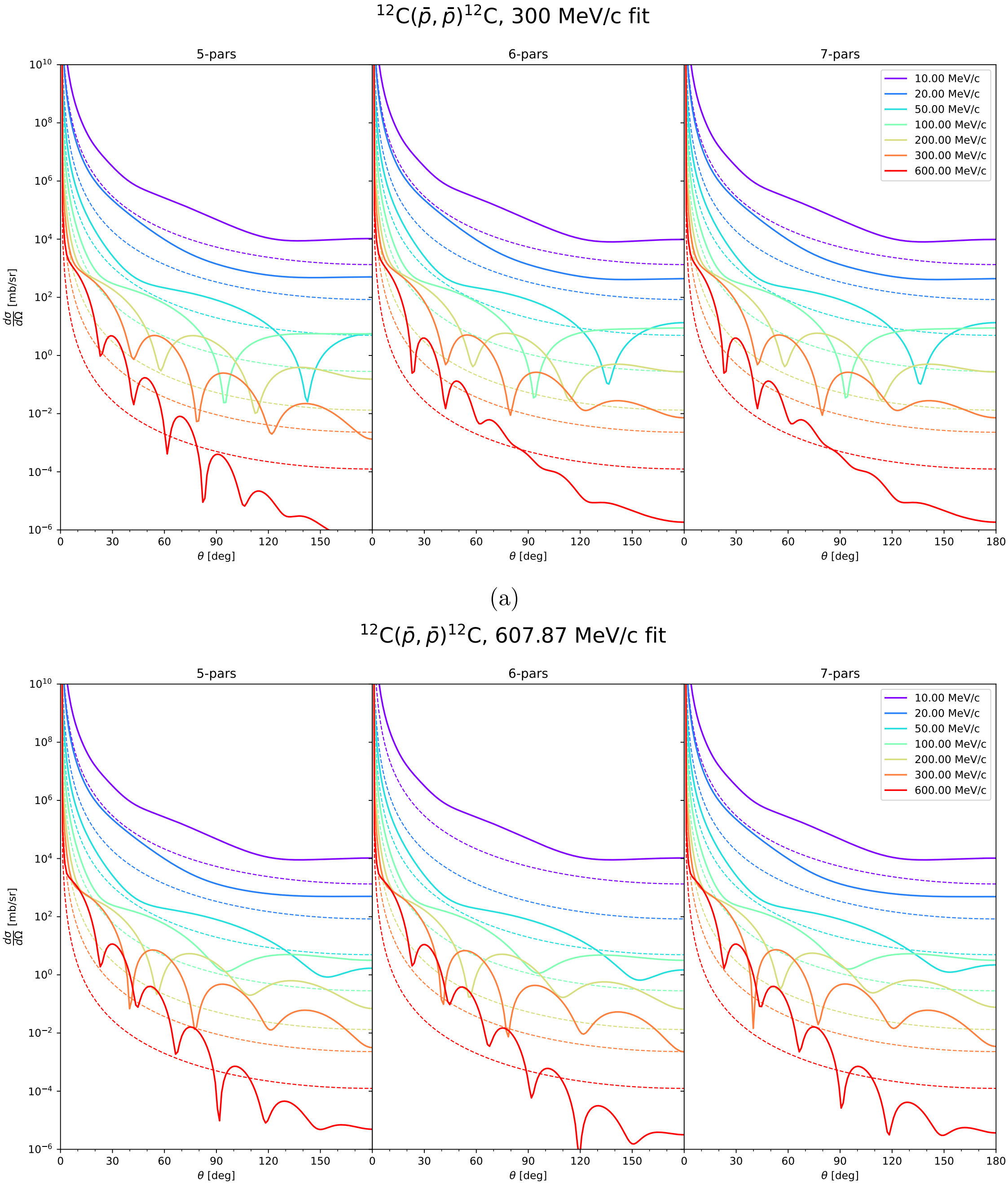

(a)

(b)

Figure 5.10: Predictions of ^{12}C elastic scattering differential cross sections using the parameter fits obtained at 300 MeV/c (5.10a) and 608 MeV/c (5.10b) fits. In dashed lines: the Rutherford cross section at the corresponding momentum.

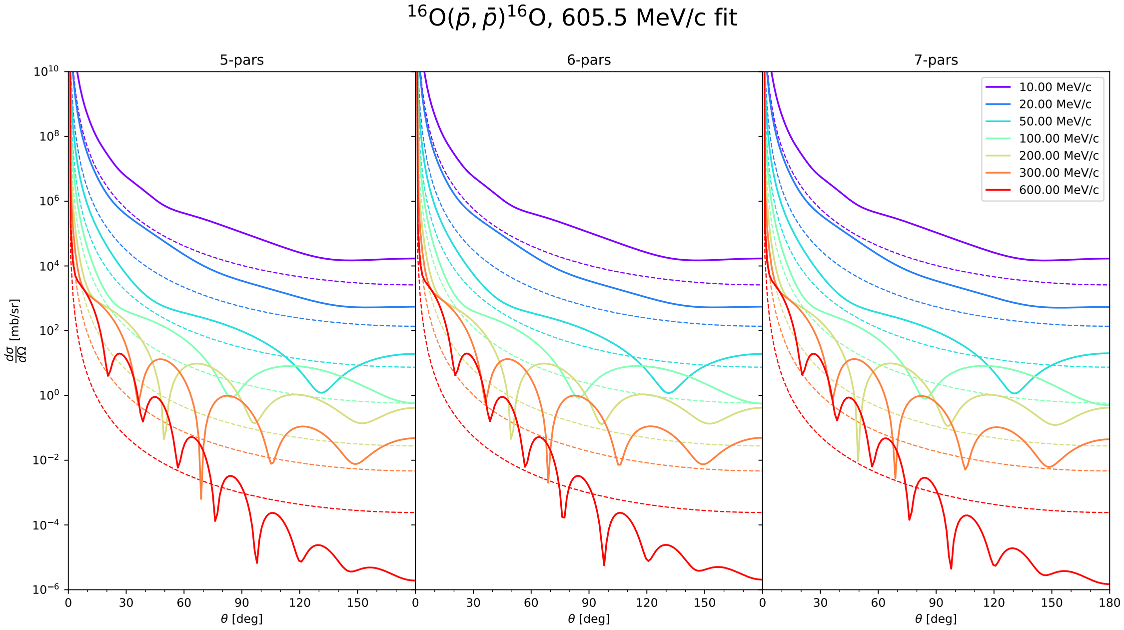

Figure 5.11: Predictions of ^{16}O elastic scattering differential cross sections using the parameter fits obtained at 605.5 MeV/c fits. In dashed lines: the Rutherford cross section at the corresponding momentum.

The first aspect mentioned before, about the proximity to the Rutherford cross section below a certain momentum, is of fundamental interest. To study the nuclear elastic scattering, its effects must be distinguishable from the Coulomb ones. Hence, if we want to perform experiments to measure the nuclear potential parameters, based on these predictions, we need to use antiprotons with momenta above 50 MeV/c, which corresponds to a value of kinetic energy $K_{\bar{p}} \sim 1.33$ MeV.

Another characteristic is the regularity of the pattern in dependence on the number of parameters used. As stated previously in Chapter 4, the 5-parameter fits are sufficient to reproduce quite fairly every data set. In Figure 5.10a a regular pattern is present only for the 5-parameter case, despite the low momentum. The hypothesis, therefore, is still that 5 parameters are sufficient to determine the values of the Woods-Saxon optical potential parameters satisfyingly, regardless of the momentum value. This can be seen also by the fact that at very low momenta ($p < 50$ MeV/c) the curves are almost identical in the three different numbers of the parameters. The main problem here is that the parameters are more correlated in this case. This could be another clue for some hidden dependencies of this model on other parameters (*e.g.* $U_0 = U_0(r_0)$, which could represent also the fact the Woods-Saxon function leaks of some dependencies).

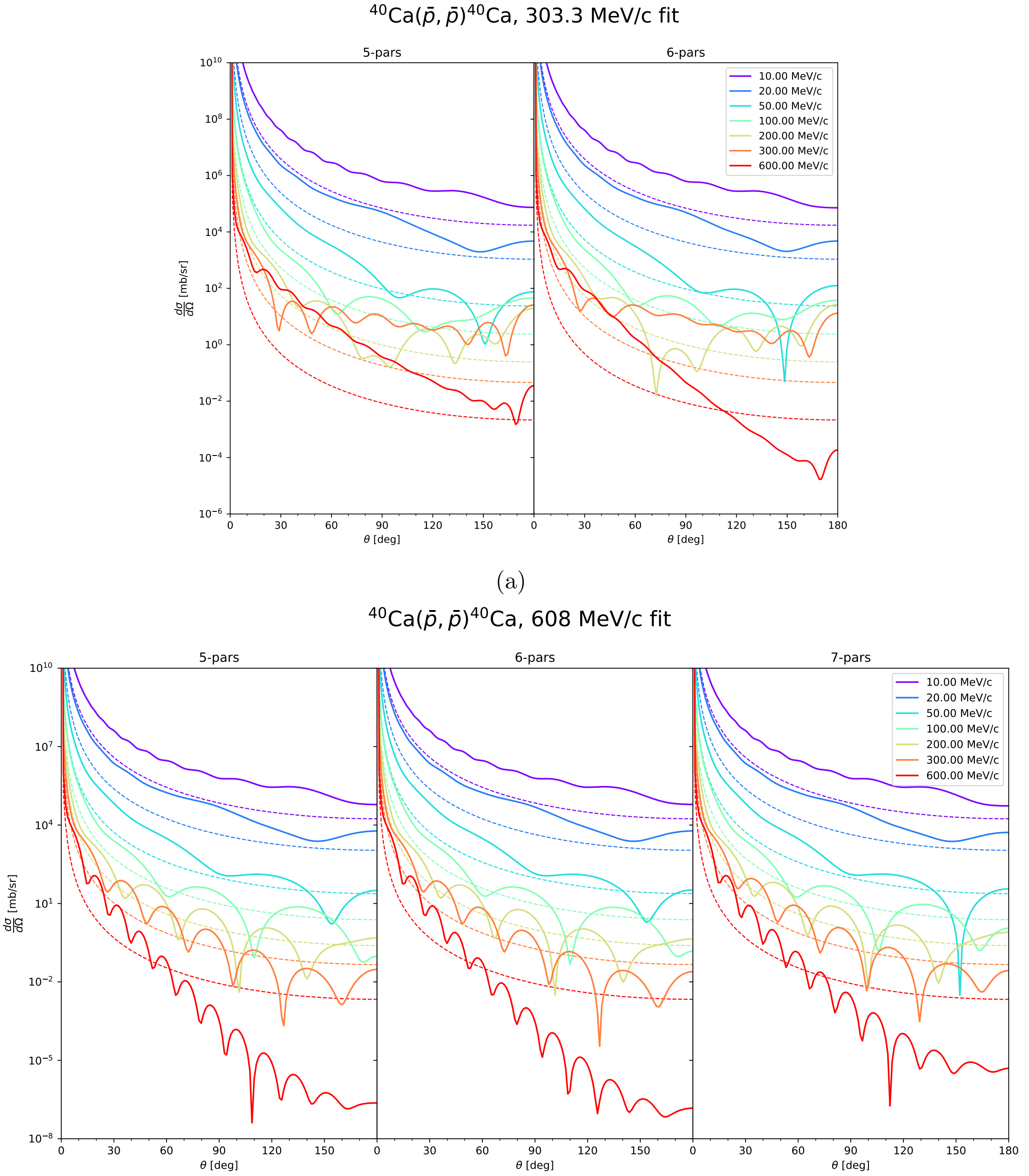

(a)

(b)

Figure 5.12: Predictions of ^{40}Ca elastic scattering differential cross sections using the parameter fits obtained at 303.3 MeV/c (5.12a) and 608 MeV/c (5.12b) fits. In dashed lines: the Rutherford cross section at the corresponding momentum.

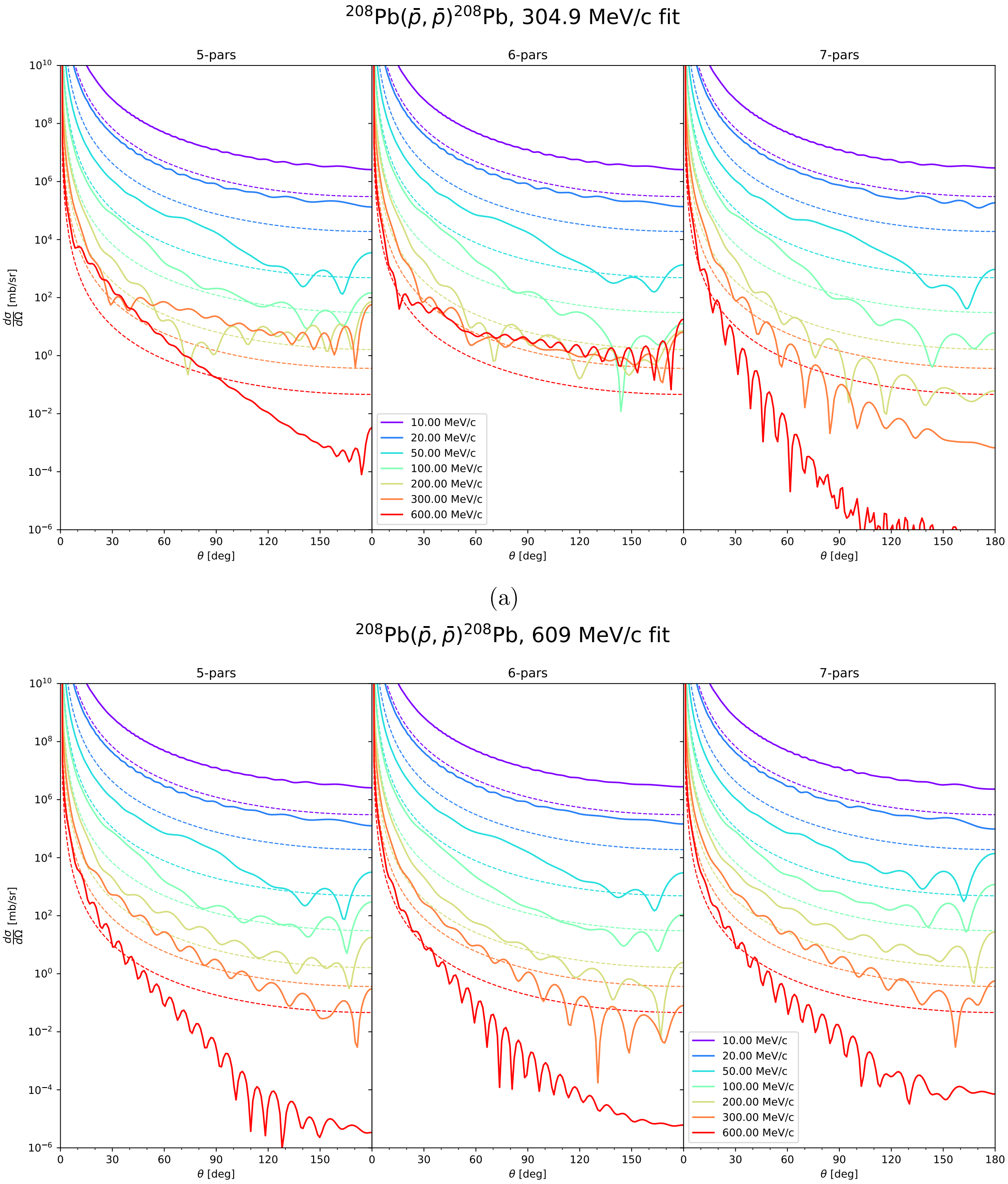

(a)

(b)

Figure 5.13: Predictions of ^{208}Pb elastic scattering differential cross sections using the parameter fits obtained at 304.9 MeV/c (5.13a) and 609 MeV/c (5.13b) fits. In dashed lines: the Rutherford cross section at the corresponding momentum.

5.4 Antineutron annihilation prediction and n̄-n oscillations

As mentioned in Chapter 2, the interest in these potentials is also due to the possibility of making predictions about $\bar{n} - n$ *oscillations*, a hypothetical phenomenon that needs specific experimental setups to be observed properly [34]. The observation of the antineutron-neutron oscillation implies the violation of the baryon number conservation, a fundamental law that underlies all the matter processes that take place in the universe [60]. This discovery could shed light on the absence of primordial antimatter in the universe, which at present is mainly made by baryonic matter, and it would suggest a direction for the extension of the Standard Model.

To design such experiments, an estimation of the $\bar{n} - n$ *oscillation time* is required. Using Equation 2.31, the lower limit of the oscillation time can be estimated[1]:

$$\tau_{\bar{n}n} = \sqrt{\frac{2\tau_A \hbar W_{\bar{n}}}{(V_{\bar{n}} - V_n)^2 + W_{\bar{n}}^2}}. \tag{5.3}$$

The following assumptions are made:

1. as usual the parameters do not depend on the projectile momentum
2. the parameters for $\bar{n}$ are equal to the ones obtained for $\bar{p}$
3. the values from the fits and not their mean on the nuclear density distribution are used.
4. the considered V_n values were $V_n = 26\,\mathrm{MeV}$ (from an average of Ref. [61]) and $V_n = 60\,\mathrm{MeV}$ (from Ref. [60])
5. for the values of τ_A which is the *effective neutron mean lifetime for annihilation in nuclear matter*, we use the estimated values for ^{16}O in Ref. [62], which are $\tau_A = 1.7 \times 10^{31}\,\mathrm{yr}$ and $\tau_A = 2.4 \times 10^{31}\,\mathrm{yr}$.

The results of these calculations are represented graphically (for all τ_A and V_n values) in Figures 5.14 to 5.16 and the explicit values can be found in Supplementary Tables C.9. We also make calculations for $\tau_{\bar{n}n}$ using the τ_A value for ^{56}Fe, obtained in 2002 by Chung *et al.* [63], since this element is the most stable.

The results are in agreement with previous estimations [49, 62] and also with the best experimental limit of recent years [64], which is $\tau_{\bar{n}n} \geq 0.86 \times 10^8\,\mathrm{s}$. We must underline that our estimation is quite rough since we do not consider the distribution mean of the nuclear matter in the calculation with Equation 5.3. We hence obtain that $\tau_{\bar{n}n} \gtrsim (0.8\text{–}1.1) \times 10^8\,\mathrm{s}$ and $\tau_{\bar{n}n} \gtrsim (0.9\text{–}1.3) \times 10^8\,\mathrm{s}$ (with $V_n = 26\,\mathrm{MeV}$ and $V_n = 60\,\mathrm{MeV}$ respectively).

The results for $\tau_A = \tau_{Fe}$ from Ref. [63] give us other limits higher than the previous ones, *i.e.* $\tau_{\bar{n}n} \gtrsim (1.6\text{–}2.3) \times 10^8\,\mathrm{s}$.

The value of $\tau_{\bar{n}n}$ is fundamental for the calculation of the probability of antineutron-neutron oscillations in time starting from a pure neutron state at $t = 0$:

$$P_{\bar{n}}(t) = \left(\frac{2\hbar}{\tau_{\bar{n}n}\Delta E}\right)^2 \sin^2\left(\frac{\Delta E t}{2\hbar}\right) e^{-t/\tau_n} \xrightarrow{\Delta E t/\hbar \ll 1} \left(\frac{t}{\tau_{\bar{n}n}}\right)^2 e^{-t/\tau_n} \tag{5.4}$$

---

[1] This quantity is a lower limit due to the derivation of the Equation (2.31) (see Ref. [60])

where $\tau_n = 879\,\mathrm{s}$ is the decay time of a free-neutron[2] and $\Delta E = E_1 - E_2 = \sqrt{(\Delta M)^2 + 4(\delta m)^2}$, with $E_{1,2} = 1/2\left[M_{11} + M_{22} \pm \sqrt{(\Delta M)^2 + 4(\delta m)^2}\right]$, where the elements M_{ii} and δm are from the matrix $\mathcal{M}$

$$\mathcal{M} = \begin{pmatrix} M_{11} & \delta m \\ \delta m & M_{22} \end{pmatrix}$$

which is the matrix of the effective Hamiltonian H_{eff} for the description of antineutron-neutron oscillation in the $(n, \bar{n})$ basis [65]. In Figure B.11 we show the curves for $P_{\bar{n}}(t)$ calculated with the four lower limits found in the previous calculation. The peaks for all cases are at $t = 2\tau_n = 1758\,\mathrm{s}$.

The search for free neutron-antineutron oscillations is still of interest in nuclear physics research. Recently it has been proposed an experiment [34] and theoretical calculations [33] for the search of this phenomenon. The values of the optical potential from antineutron data are extremely important to make these predictions and to design correctly the experimental setup. As already underlined, the absence of antineutron data requires focusing on antiproton data and extrapolating the possible values of the oscillation time (or the scattering length).

---

[2] We are considering also the decay of the neutron since we are assuming the free-neutron case.

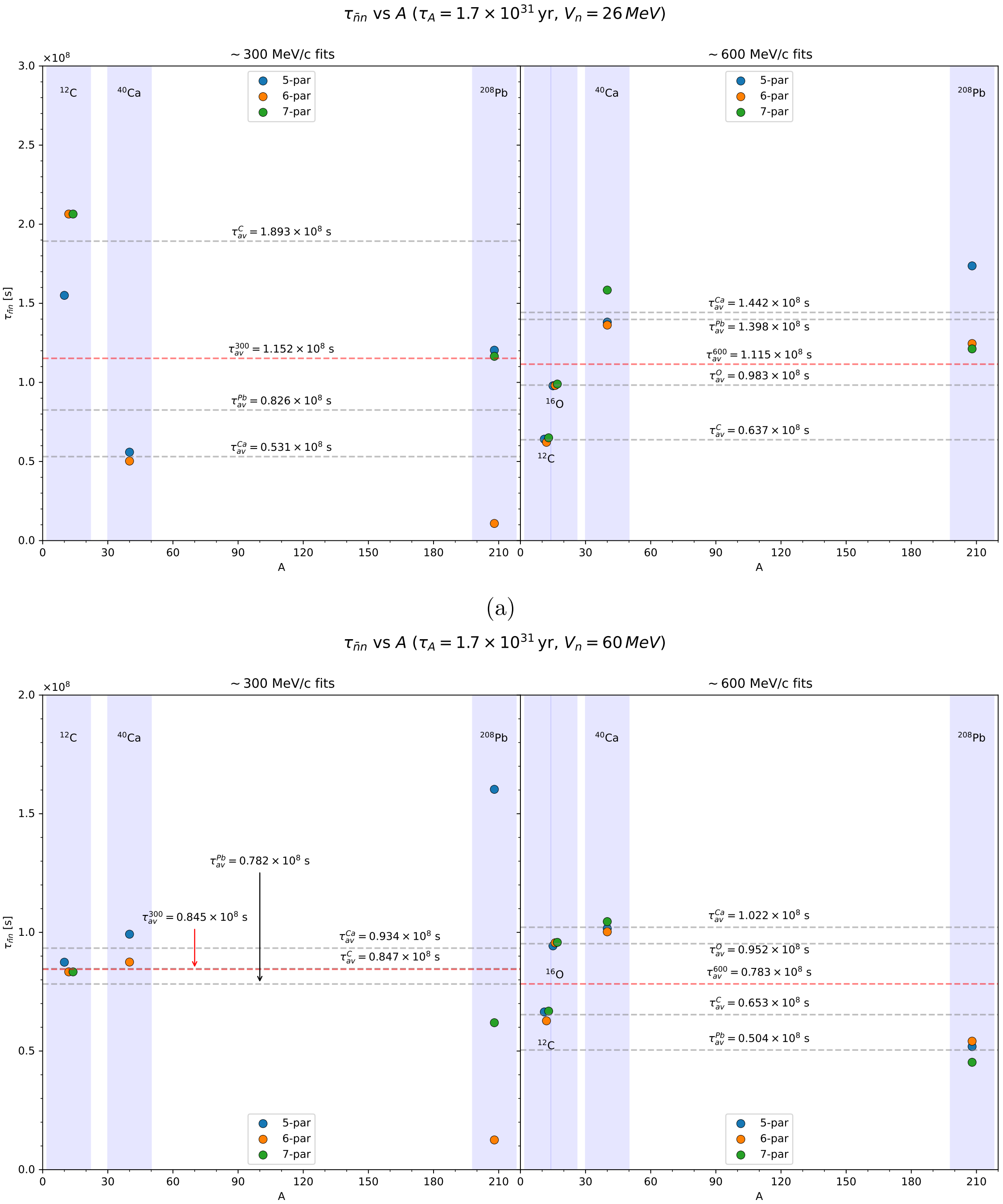

Figure 5.14: Predictions for lifetime for $\bar{n} - n$ oscillations in dependence of atomic mass with $\tau_A = 1.7\times10^{31}$ yr, $V_n = 26\,\text{MeV}$ (5.14a) and $V_n = 60\,\text{MeV}$ (5.14b).

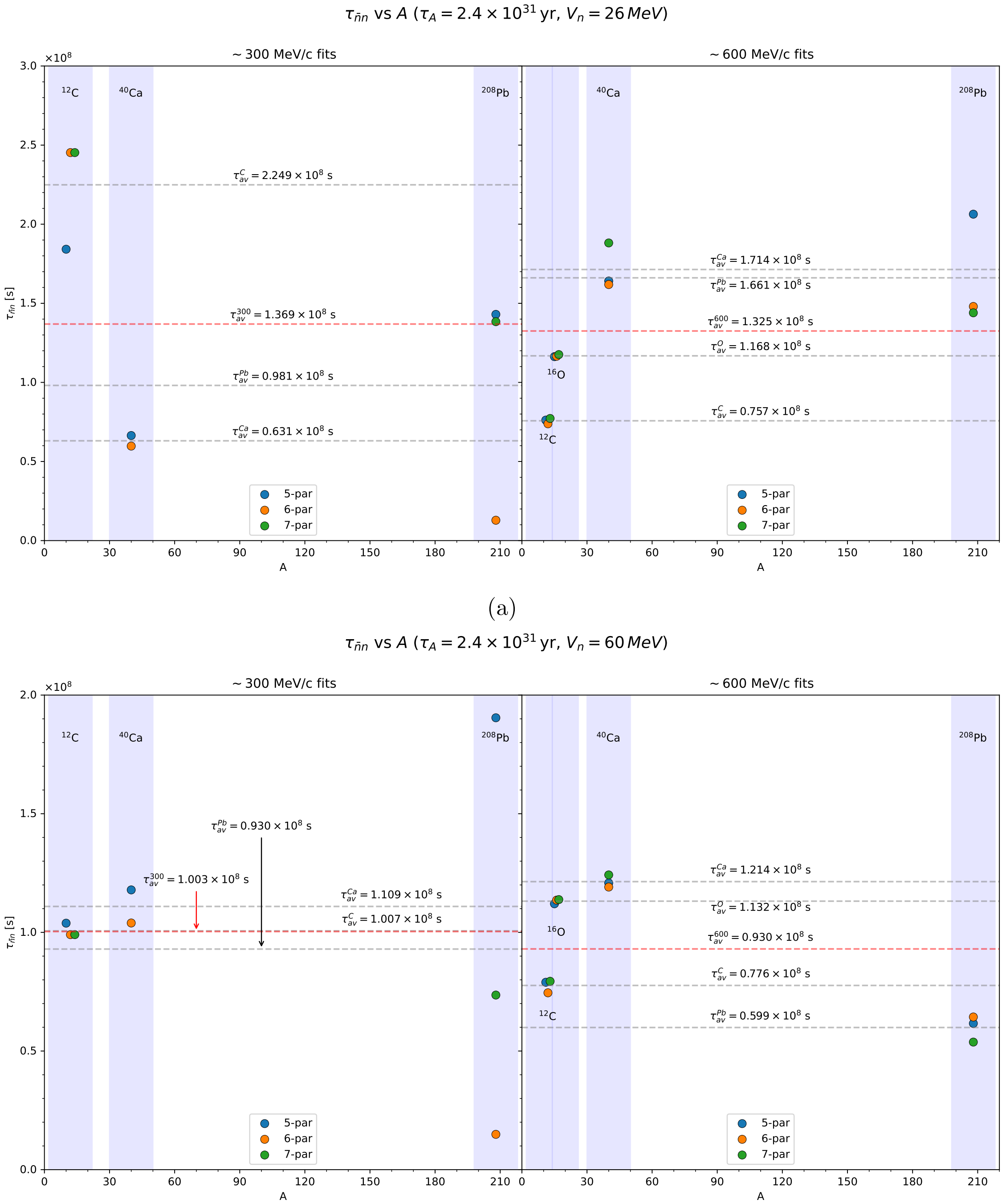

(a)

(b)

Figure 5.15: Predictions for lifetime for $\bar{n} - n$ oscillations in dependence of atomic mass with $\tau_A = 2.4 \times 10^{31}\,\text{yr}$, $V_n = 26\,\text{MeV}$ (5.15a) and $V_n = 60\,\text{MeV}$ (5.15b).

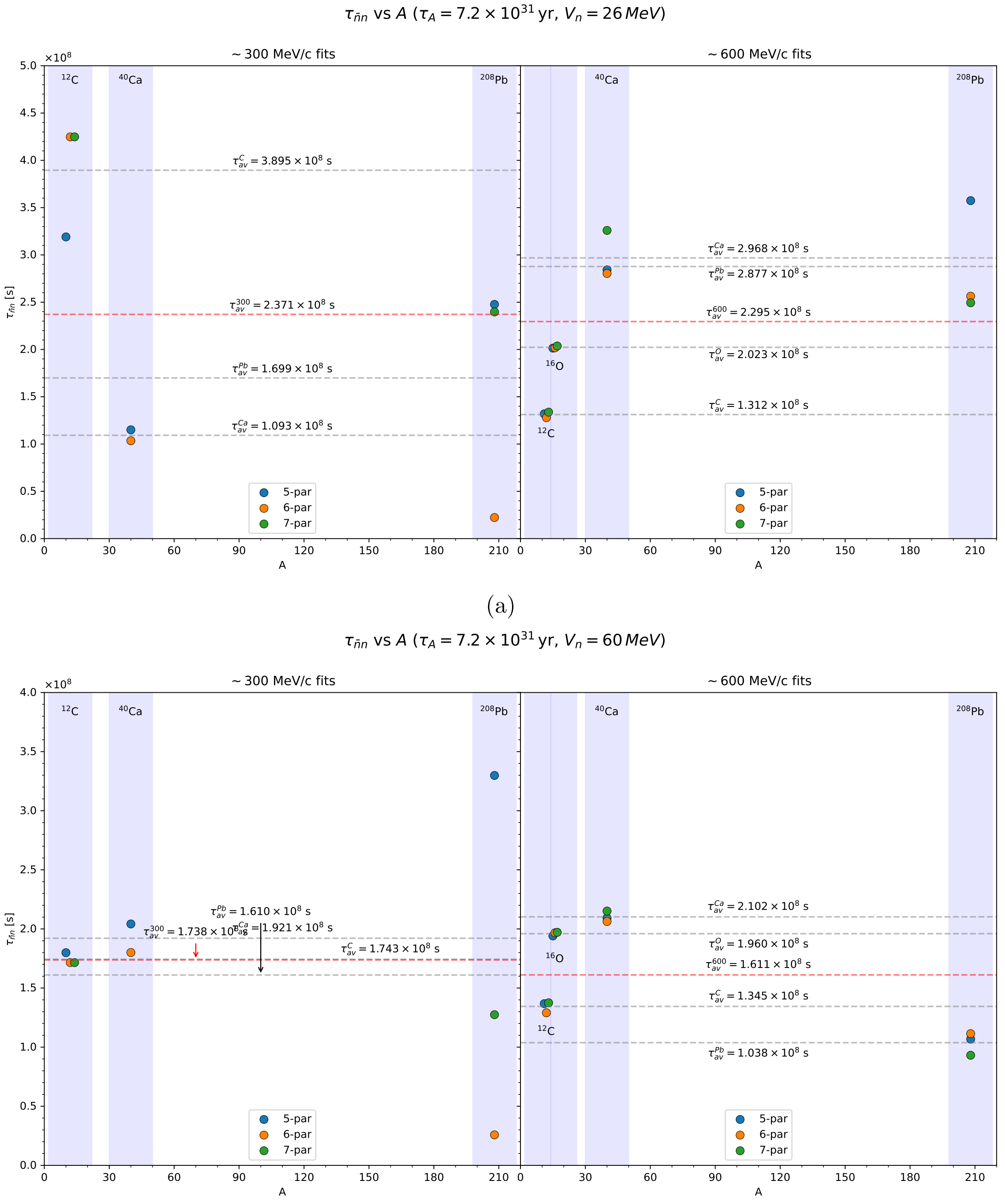

(b)

Figure 5.16: Predictions for lifetime for $\bar{n} - n$ oscillations in dependence of atomic mass with $\tau_A = 7.2 \times 10^{31}$ yr, $V_n = 26\,\text{MeV}$ (5.16a) and $V_n = 60\,\text{MeV}$ (5.16b).

5.5 Summary

In this chapter, the results presented in Chapter 4 and some aspects of parameter correlations were discussed. In general, the obtained fits are good to represent the data, in particular at momenta around 600 MeV/c. However, the correlations of the parameters, in all cases, seem quite high. This could mean that the parameters depend on other parameters or projectile energy or again the model could not be the most adequate for this case.

Predictions of differential elastic scattering cross section for low projectile-momenta were made. The results indicate that for momenta below 50 MeV/c the Coulomb scattering dominates over the strong nuclear one, resulting in cross sections very similar to the Rutherford scattering ones. Therefore, measurements performed at these momenta give no additional information about strong interaction. To extrapolate significant information for the antinucleon-nucleus interaction the experiments must be performed with a projectile above 50 MeV/c.

Finally, some estimations about the lower limit of the antineutron-neutron oscillation time $\tau_{\bar{n}n}$ were made. The obtained values for the oscillation time are $\tau_{\bar{n}n} \gtrsim (0.8\text{–}2.3) \times 10^8\,\mathrm{s}$, depending on the value choices of other quantities (τ_A and V_n). These results are in line with previous predictions.

Chapter 6

Conclusions

6.1 Summary of the results

Some of the available data for antiproton elastic scattering and reaction cross sections were analysed in the present work. In particular, four nuclear species were considered: ^{12}C, ^{16}O, ^{40}Ca and ^{208}Pb. The analysis used an optical potential approach with a Woods-Saxon potential, a complex potential to take into account absorptive (imaginary part) and non-absorptive (real part) processes. The defined potential had a variable number of free parameters (from 5 to 7). The parameters are:

- the potential strengths: U_0, W_0;
- the geometrical parameters: r_0 (r_{0R} and r_{0I} for 6 and 7-parameter models), which is the *nuclear radius parameter*; a (a_R and a_I for 7-parameter models), which is the *diffuseness* of the nuclear surface;
- the normalization parameter λ.

The geometrical parameters define the shape of the potential through the function in Equation 2.13.

The calculations were made using the partial-wave formalism, where the incoming particle is treated as a matter-wave that interacts with an obstacle – the nucleus target – and generates diffraction and interference, similar to the optical picture. The non-relativistic Schrödinger equation was then solved using the Woods-Saxon potential to obtain the wave functions and therefore to calculate the cross sections of the processes we are interested in – elastic scattering and reactions.

A fitting procedure was performed to find the best values of the parameters of the potential to reproduce the data. We performed the minimization of a standard χ^2 with the addition of a pull term to constrain the normalization parameter around 1. We used only antiproton cross section data for the elastic scattering process.

The fits for ^{12}C and ^{16}O are quite good and reproduce very precisely the available data. However, many different values could reproduce such data – due to the *continuous-parameter ambiguity*, well known in this kind of analysis. Nonetheless, we obtained good fits and precise parameter values, which on some occasions reproduce the reaction cross sections satisfyingly. The ^{40}Ca and ^{208}Pb cases were more complicated to evaluate since not always converge, and the results were quite good but worse than the previous ones. Globally, our calculations fit quite well with the data of these two targets. With the increase of the atomic weight A of the target, the potential seems to change in the strengths values, passing from non-absorptive ($U_0 > W_0$) to "equally-absorptive" ($U_0 \simeq W_0$). In very few cases we had slightly-absorptive potentials ($W_0 \gtrsim U_0$) or strongly-absorptive ($W_0 \gg U_0$). Again, this fact could be linked to the continuous-parameters ambiguity, since the strengths and the geometrical parameters in many cases are strongly correlated (as can be seen from the supplementary tables in Section C). The model cannot fit easily the reaction cross sections due to the scarcity of data, and therefore the same values of the differential elastic scattering cross sections were used, which show a clear dependence of some parameters on the momentum.

Some tries were done to extrapolate other information from these fits, for both antiproton and antineutron. The low-energy predictions for the antiproton differential elastic scattering cross sections were calculated. Above the 50 MeV/c, the pattern due to the nuclear potential is visible and experimentally feasible to detect. Below this threshold, it is hardly possible to distinguish the pattern from the Rutherford cross section, *i.e.* the pure electromagnetic scattering. Therefore, supposing the parameters are constant in the momentum, these projections show that experiments need for antiproton at least of 50 MeV/c to determine useful information on the nuclear potential and its parameters.

The data available for antineutrons are less than the ones for antiprotons. Assuming the parameters for antineutrons to be the same as antiprotons, rough estimations for antineutron-neutron oscillation were made. The focus was on the antineutron-neutron oscillation time, which is the fundamental quantity to predict the oscillation probability. Our estimations give $\tau_{\bar{n}n} = (0.8\text{–}2.3) \times 10^8$ s which is in agreement with previous results.

6.2 Possible future developments

The analysis made in the present work is far from being complete. However, not many other works made research in this direction, to include all the data available and analyse them in a clear framework with all details on the algorithms used for calculations. Moreover, the first and greatest problem of this work is the absence of available data. In addition, some of the existing data are not accessible online to everyone. The databases for nuclear data have no information about antinucleon data, except from Nakamura data [57]. These databases must be updated with precise values from the original articles, which were mainly passed via "private communications" and similar. This is the first step to allow more analyses in the future and to compare these analyses and obtain new results.

Accessibility of data apart, the present work weaknesses are the following

1. absence of direct fits on the reaction cross section data;
2. absence of fits on antineutrons data.

These analyses are fundamental to have precise predictions about the oscillation time of antineutron-neutron oscillations. Moreover, the comparison between reaction cross sections of antiproton and antineutron shows an anomalous behavior, as highlighted by Friedman *et al.* [66], resulting in equal or lower values for antiproton reaction cross sections than the antineutron ones at low momenta. At the moment, this is not understood. In particular, due to Coulomb focusing, one expects higher reaction cross sections at low momenta for antiprotons with respect to the antineutrons case, since they are electrically neutral and are not attracted by the electrically positive nucleus. These analyses could shed some light on this unexpected phenomenon. Furthermore, using a modified version of the Woods-Saxon model, including dependence on the projectile momentum in the parameters, with the reaction cross sections one can determine which is the closest functional form to represent this dependence.

A global fit regarding both reaction and elastic scattering cross sections would be desirable since a unique model should describe both processes. This could also be an easy first step to make and in the next years, we will proceed in that direction.

Once a reliable model is found, one could make some predictions at low energy - as we made in Section 5.3 - which are of interest for low-energy facilities to design future experiments to test the models and also to investigate nuclear interactions of antimatter with matter. These interactions are of primary interest to many other experiments in progress nowadays. Facilities like ELENA [67] or the future FLAIR [68, 69] are in continuous development to host new experiments of this kind, to investigate new phenomena at poorly explored energies. As indicated in this work – and anticipated in Ref. [70] – these experiments could explore only regions with antiproton momentum above 50 MeV/c ($K_{cm} \simeq 1.3\,\mathrm{MeV}$).

These calculations could be helpful also to present experiments at low energies to determine the entity of these phenomena and have more precise analyses.

Appendix A

The Graphical User Interface P̄XS

To automatize the procedures in the fitting to data, a Graphical User Interface (GUI) to access data and fit-results files and to check the validity of the fits rapidly and straightforwardly has been realized. The GUI is realized with the `Python` package `PySimpleGUI` [71] and it consists of five programs:

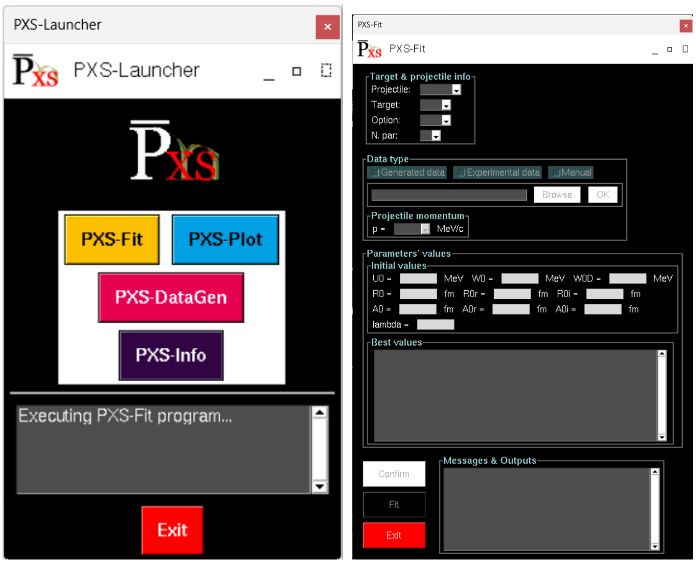

Executing PXS-Fit program...

(a) (b)

Figure A.1: (a): the `P̄XS-Launcher` window; (b): the `P̄XS-Fit` window.

- `P̄XS Launcher` (Figure A.1a):
  main window, all the other GUI programs can be opened rapidly
- `P̄XS Fit` (Figure A.1b):
  program to do the fitting
- `P̄XS Plot` (Figure A.2a):
  program to plot the cross sections (from a fit-result file or from given parameters)
- `P̄XS DataGen` (Figure A.2b):
  program to generate data from given parameters (to validate the fitting)

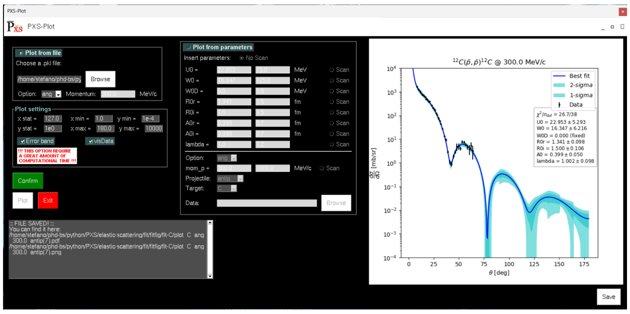

Choose a .pkl file: /home/stefano/phd-bs/py

Option: ang Momentum: 300.0 MeV/c

Plot settings

x stat = 127.0 x min = 1.0 y min = 1e-4

y stat = 1e0 x max = 180.0 y max = 10000

☑ Error band ☑ visData

Insert parameters: ● No Scan

U0 = 22.953 75.0 MeV ○ Scan

W0 = 16.347 125.0 MeV ○ Scan

W0D = 0.0 5.0 MeV ○ Scan

R0r = 1.341 1.5 fm ○ Scan

R0i = 1.5 1.5 fm ○ Scan

A0r = 0.399 0.7 fm ○ Scan

A0i = 0.399 0.7 fm ○ Scan

lambda = 1.0 1.2 ○ Scan

Option: ang

mom_p = 300.0 1000.0 MeV/c ○ Scan

Projectile: antip

Target: C

Data:

```
::: FILE SAVED! :::
You can find it here:
/home/stefano/phd-bs/python/PXS/elastic-scattering/fit/fitfig/fit-C/plot  C  ang
  300.0  antip(7).pdf
/home/stefano/phd-bs/python/PXS/elastic-scattering/fit/fitfig/fit-C/plot  C  ang
  300.0  antip(7).png
```

$\chi^2/n_{\rm dof}$ = 26.7/38
U0 = 22.953 ± 5.293
W0 = 16.347 ± 6.216
W0D = 0.000 (fixed)
R0r = 1.341 ± 0.098
R0i = 1.500 ± 0.106
A0 = 0.399 ± 0.050
lambda = 1.002 ± 0.098

(a)

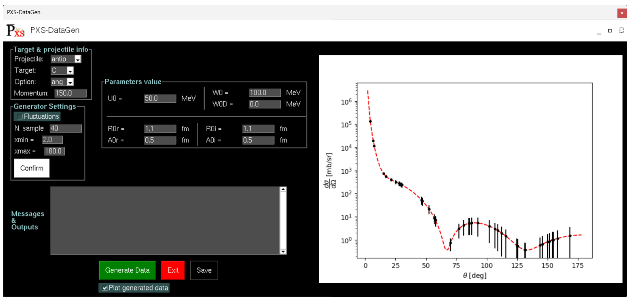

Target & projectile info

Projectile: antip

Target: C

Option: ang

Momentum: 150.0

Generator Settings

☐ Fluctuations

N. sample 40

xmin = 2.0

xmax = 180.0

Parameters value

U0 = 50.0 MeV

W0 = 100.0 MeV

W0D = 0.0 MeV

R0r = 1.1 fm

R0i = 1.1 fm

A0r = 0.5 fm

A0i = 0.5 fm

☑ Plot generated data

(b)

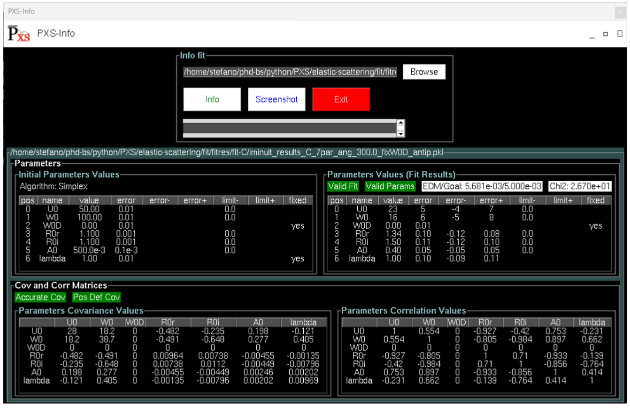

/home/stefano/phd-bs/python/PXS/elastic-scattering/fit/fitr

/home/stefano/phd-bs/python/PXS/elastic-scattering/fit/fitres/fit-C/iminuit_results_C_7par_ang_300.0_fixW0D_antip.pkl

Initial Parameters Values

Algorithm: Simplex

pos	name	value	error	error-	error+	limit-	limit+	fixed
0	U0	50.00	0.01			0.0		
1	W0	100.00	0.01			0.0		
2	W0D	0.00	0.01					yes
3	R0r	1.100	0.001			0.0		
4	R0i	1.100	0.001			0.0		
5	A0	500.0e-3	0.1e-3			0.0		
6	lambda	1.00	0.01					yes

Parameters Values (Fit Results)

EDM/Goal: 5.681e-03/5.000e-03 Chi2: 2.670e+01

pos	name	value	error	error-	error+	limit-	limit+	fixed
0	U0	23	5	-4	7	0.0		
1	W0	16	6	-5	8	0.0		
2	W0D	0.00	0.01					yes
3	R0r	1.34	0.10	-0.12	0.08	0.0		
4	R0i	1.50	0.11	-0.12	0.10	0.0		
5	A0	0.40	0.05	-0.05	0.05	0.0		
6	lambda	1.00	0.10	-0.09	0.11			

Parameters Covariance Values

	U0	W0	W0D	R0r	R0i	A0	lambda
U0	28	18.2	0	-0.482	-0.235	0.198	-0.121
W0	18.2	38.7	0	-0.491	-0.648	0.277	0.405
W0D	0	0	0	0	0	0	0
R0r	-0.482	-0.491	0	0.00964	0.00738	-0.00455	-0.00135
R0i	-0.235	-0.648	0	0.00738	0.0112	-0.00449	-0.00796
A0	0.198	0.277	0	-0.00455	-0.00449	0.00246	0.00202
lambda	-0.121	0.405	0	-0.00135	-0.00796	0.00202	0.00969

Parameters Correlation Values

	U0	W0	W0D	R0r	R0i	A0	lambda
U0	1	0.554	0	-0.927	-0.42	0.753	-0.231
W0	0.554	1	0	-0.805	-0.984	0.897	0.662
W0D	0	0	0	0	0	0	0
R0r	-0.927	-0.805	0	1	0.71	-0.933	-0.139
R0i	-0.42	-0.984	0	0.71	1	-0.856	-0.764
A0	0.753	0.897	0	-0.933	-0.856	1	0.414
lambda	-0.231	0.662	0	-0.139	-0.764	0.414	1

(c)

Figure A.2: From the top to the bottom: `P̄XS-Plot`, `P̄XS-DataGen` and `P̄XS-Info` windows.

- `P̄XS Info` (Figure A.2c):
  program to visualize the validity, covariance matrix, and correlation matrix of the fit.

`P̄XS Fit`, `P̄XS Plot`, and `P̄XS DataGen` calculate the cross sections calling the `FORTRAN77` code, using potential parameters and other variables inserted by the user.

`P̄XS Fit` is the main software used in the analysis. Selecting the desired target, projectile, the type of data the user is interested in analysing, and the number of free parameters, the interface opens a window for selecting the experimental data (text files) available in the directory `data`. Data are organized by type: elastic scattering (`ang` in GUI, `es` in the directory) and reaction (`mom` in GUI, `reac` in the directory). Each type is organized by targets, where each directory contains many files with different projectile momenta. Once the dataset is selected, the momentum is automatically set (but it can be modified) and the potential parameters can be fixed. Then, the initial values can be fixed or a random choice can be done until the χ^2 is below 700 to facilitate the search of minima. Then the fit is executed via `iMinuit` [58] and a popout window shows the variation in values and χ^2 during the procedure until the procedure is finished. The resulting file, a `pickle` file containing all the information about the fit, is saved automatically and can be retrieved by the other software.

`P̄XS Plot` is dedicated to the making of graphs with dataset visualization, the cross section curves, and their relative error bands. This can be done by the selection of the `pickle` file from the fitting procedure, which automatically retrieves all the information for the plots, or from parameters and a dataset passed manually by the user. The error bands are calculated by the use of the `jacobi` package [72]. The image file is saved both in `png` and `pdf` formats.

`P̄XS DataGen` is the software used for the validation. This GUI, given the parameters of the potential, the number of samples to extract, and the momentum of the projectile, randomly selects a set of pseudo-data that follow the cross section curve selected. A random fluctuation inside the error assigned to the pseudo-data (see Equation (5.1)) can be added to the data to reproduce possible statistical and experimental fluctuations. The data produced are saved in a text file containing in the first lines also the potential parameters used, the type of data generated, the presence of fluctuations, the number of samples generated, and the range of the independent variable used (angle or momentum). An example of this information is shown in Figure A.3.

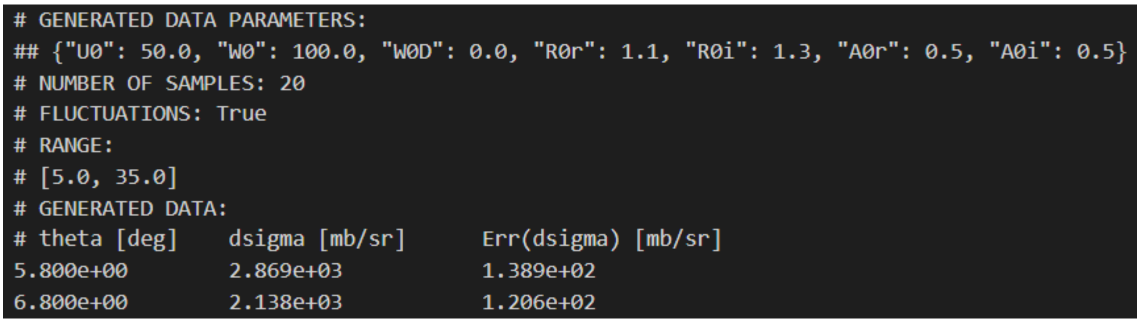

```
# GENERATED DATA PARAMETERS:
## {"U0": 50.0, "W0": 100.0, "W0D": 0.0, "R0r": 1.1, "R0i": 1.3, "A0r": 0.5, "A0i": 0.5}
# NUMBER OF SAMPLES: 20
# FLUCTUATIONS: True
# RANGE:
# [5.0, 35.0]
# GENERATED DATA:
# theta [deg]    dsigma [mb/sr]      Err(dsigma) [mb/sr]
5.800e+00        2.869e+03           1.389e+02
6.800e+00        2.138e+03           1.206e+02
```

Figure A.3: An example of a `P̄XS DataGen` file heading. The lines that start with # are not used by the codes.

`P̄XS` Info prints on tables the information about the fitting procedure, which includes the initial values of the parameters, the final values after the fit to the data, the estimated parameter errors, and the χ^2 value at minimum. Moreover, also the correlation and covariance matrices are printed. See Figure A.2c for an example.

The usual procedure for fitting to the data is the following:

1. Fitting to the data using `P̄XS-Fit`
2. Check if the fit is valid using `P̄XS-Info`. In the case the fit is invalid or is not precise, repeat point 1).
3. If the fit is valid, plot the curve and the information of the fit using `P̄XS-Plot`.

To test the changes in the code, one can use the `P̄XS-DataGen` program to generate pseudo-data controlling the parameter values.

Appendix B

Supplementary figures

B.1 Projection for 0°–180° range

The elastic scattering experimental data, as mentioned in Section 4.1, are limited in the angle range $\theta \sim 0^\circ - 60^\circ$. We have no information about the behavior of the differential elastic cross sections for angles above 60° – and in particular for large angles ($\theta > 90^\circ$). For this reason, predictions of what could be the behavior of the cross sections for these angles are made. The best-fit curve for all the targets and momenta for the complete range $0^\circ - 180^\circ$ are shown in Figures B.1 to B.7. The experimental data in the following plots are from Ref. [48].

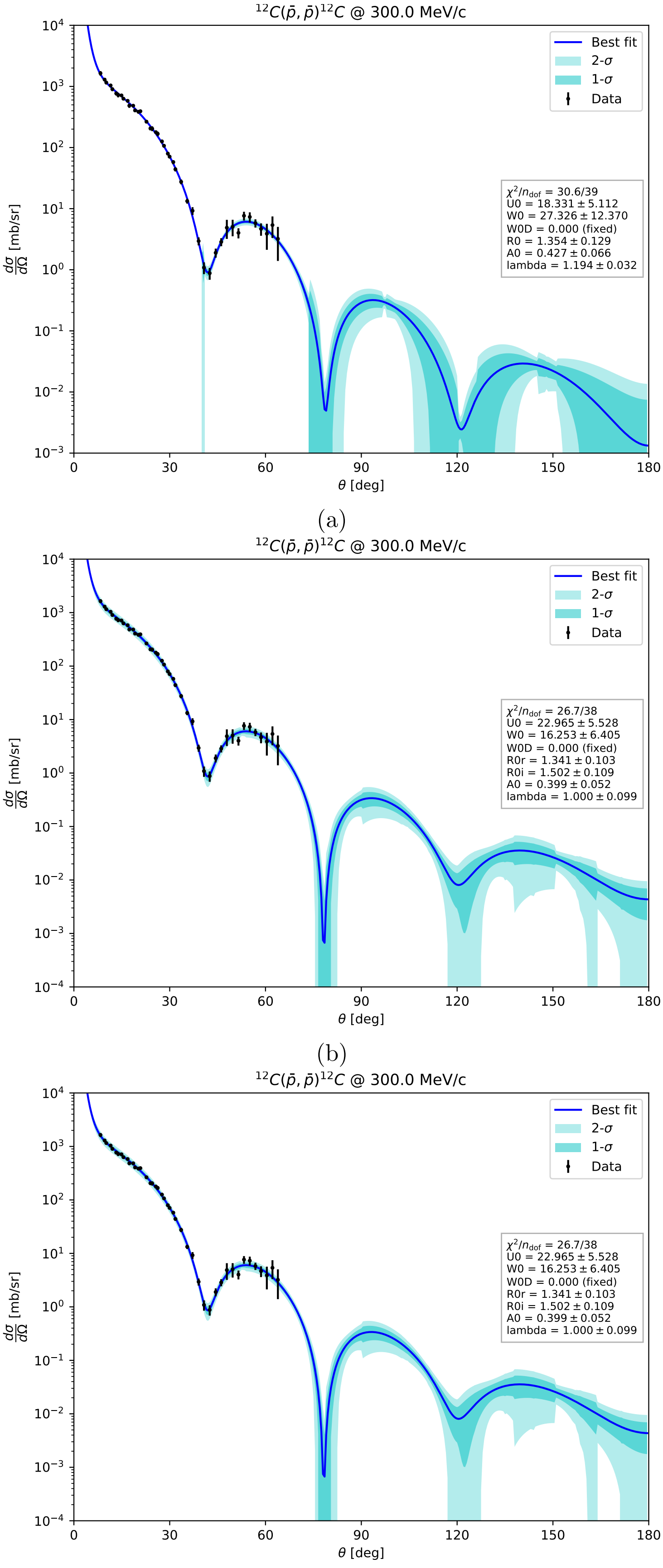

(a)

(b)

(c)

Figure B.1: 6- (B.1a), 7- (B.1b) and 8- (B.1c) parameters best-fit curve with error bands at 1-σ and 2-σ for ^{12}C at $E_{\bar{p}} = 46.8\,\text{MeV}$ ($p = 300\,\text{MeV/c}$) between $0^\circ - 180^\circ$.

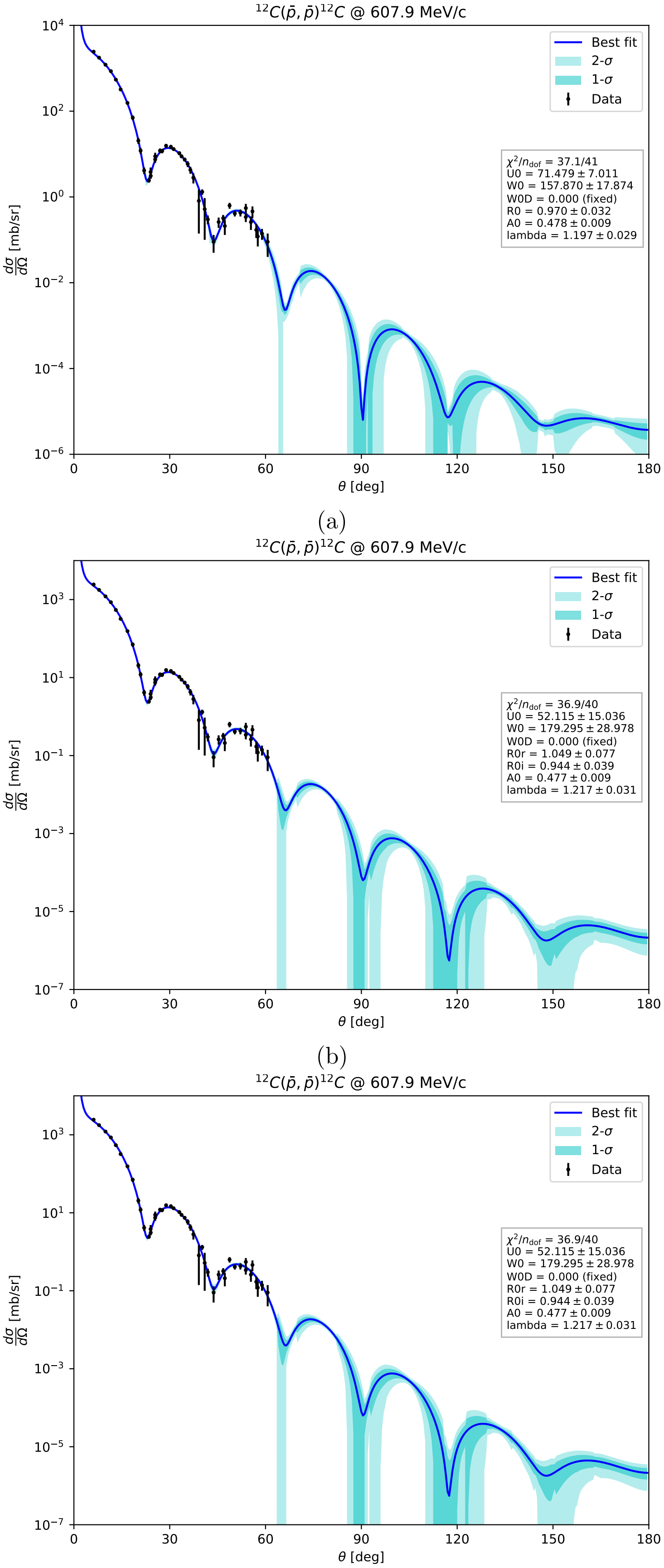

(c)

Figure B.2: 6- (B.2a), 7- (B.2b) and 8- (B.2c) parameters best-fit curve with error bands at 1-σ and 2-σ for ^{12}C at $E_{\bar{p}} = 179.7\,\text{MeV}$ ($p = 607.9\,\text{MeV/c}$) between $0° - 180°$.

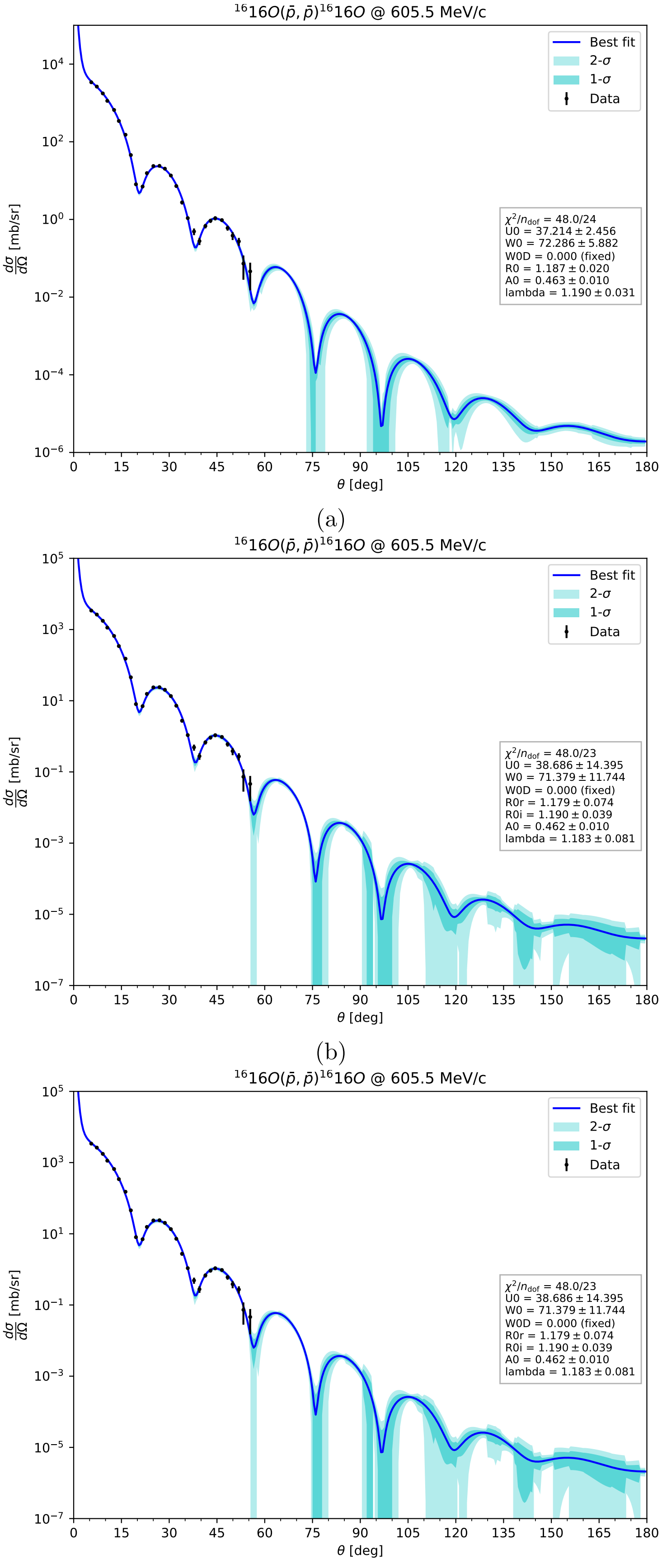

Figure B.3: 6- (B.3a), 7- (B.3b) and 8- (B.3c) parameters best-fit curve with error bands at 1-σ and 2-σ for ^{12}O at $E_{\bar{p}} = 178.4\,\mathrm{MeV}$ ($p = 605.5\,\mathrm{MeV/c}$) between $0^\circ - 180^\circ$.

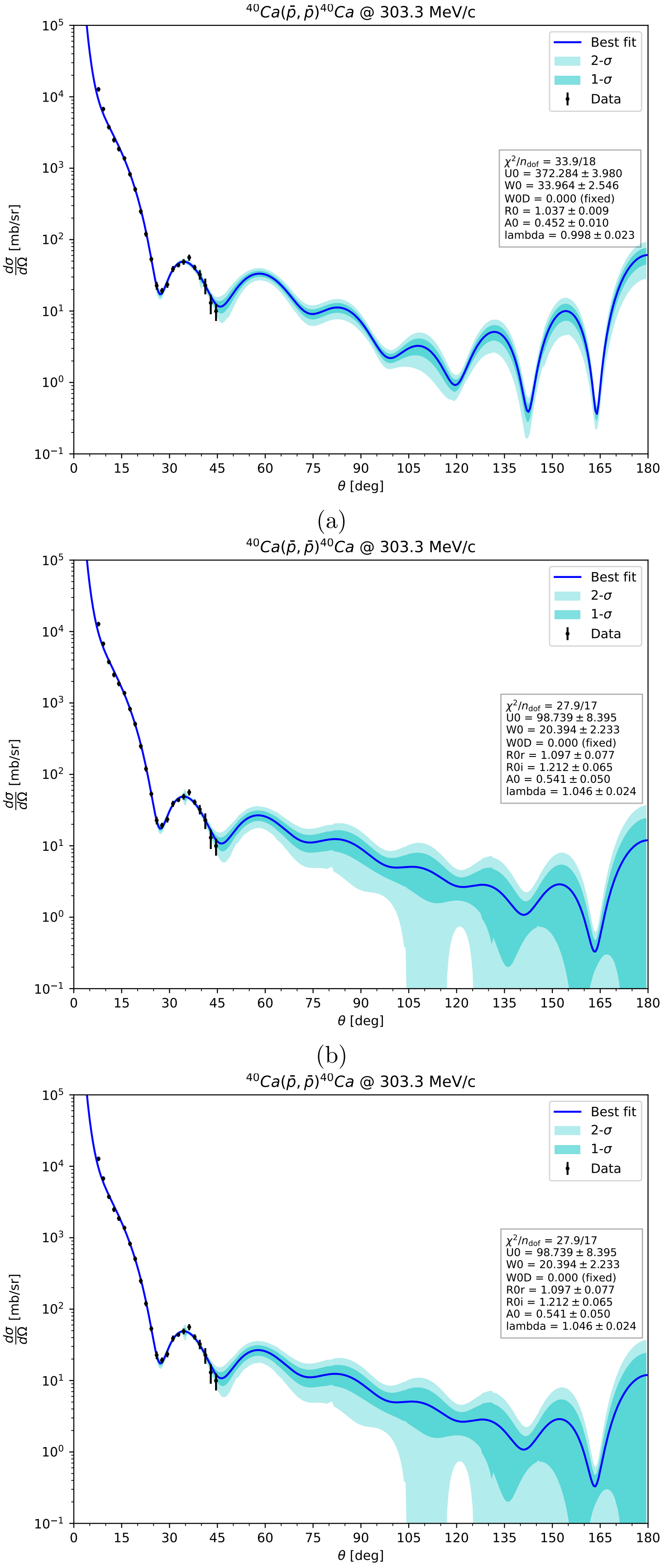

(a)

(b)

(c)

Figure B.4: 6- (B.4a), 7- (B.4b) and 8- (B.4c) parameters best-fit curve with error bands at 1-σ and 2-σ for ^{40}Ca at $E_{\bar{p}} = 46.8\,\mathrm{MeV}$[?]($p = 303.3\,\mathrm{MeV/c}$) between $0^\circ - 180^\circ$.

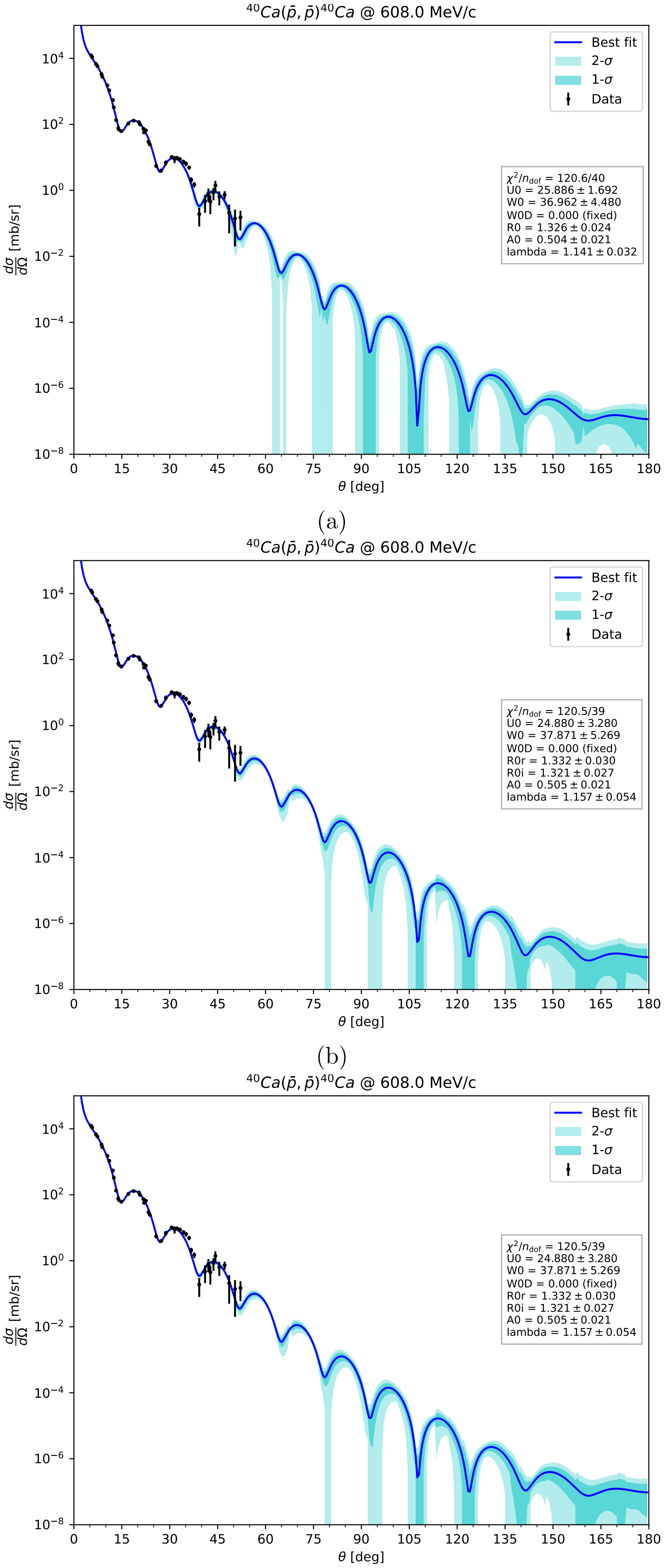

(a)

(b)

(c)

Figure B.5: 6- (B.5a), 7- (B.5b) and 8- (B.5c) parameters best-fit curve with error bands at 1-σ and 2-σ for ^{40}Ca at $E_{\bar{p}} = 179.7\,\mathrm{MeV}$ ($p = 608\,\mathrm{MeV/c}$) between $0^\circ - 180^\circ$.

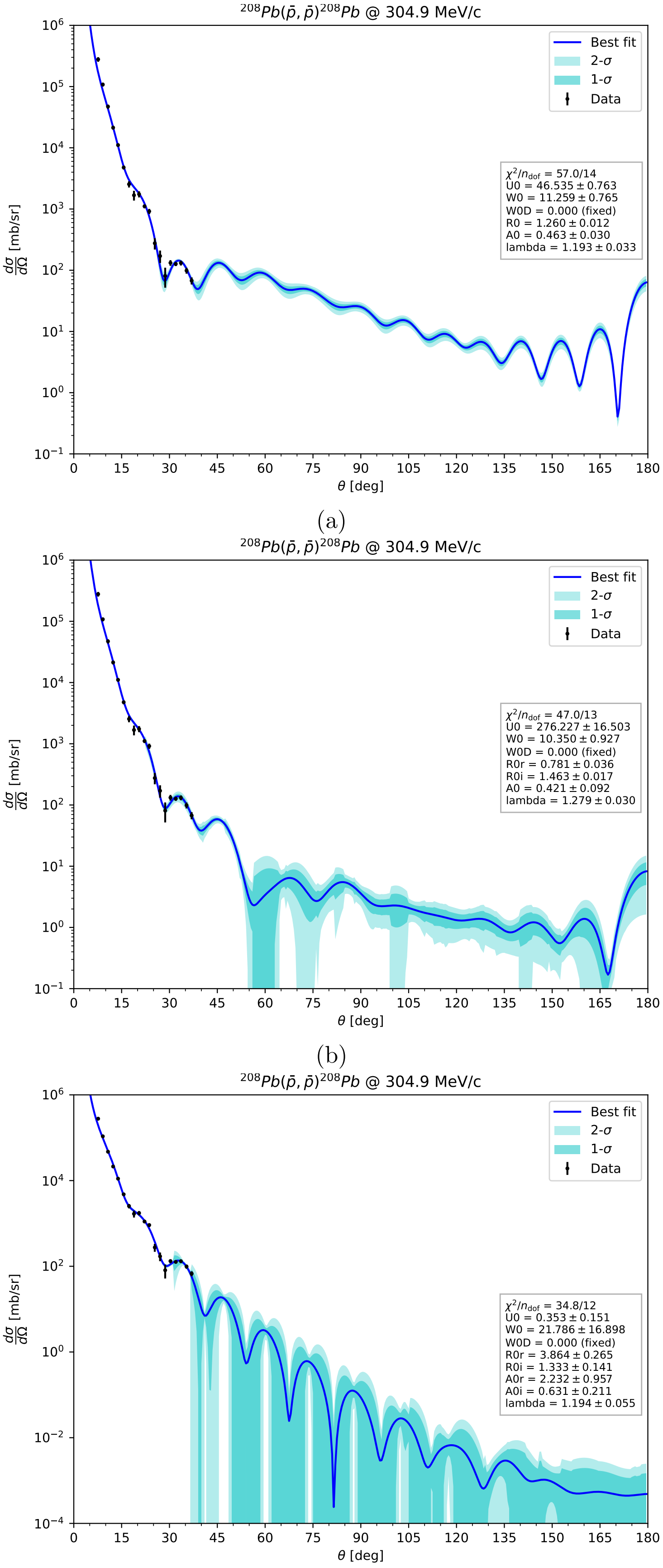

(a)

(b)

(c)

Figure B.6: 6- (B.6a), 7- (B.6b) and 8- (B.6c) parameters best-fit curve with error bands at 1-σ and 2-σ for ^{208}Pb at $E_{\bar{p}} = 46.8\,\mathrm{MeV}$[?]($p = 304.9\,\mathrm{MeV/c}$) between $0° - 180°$.

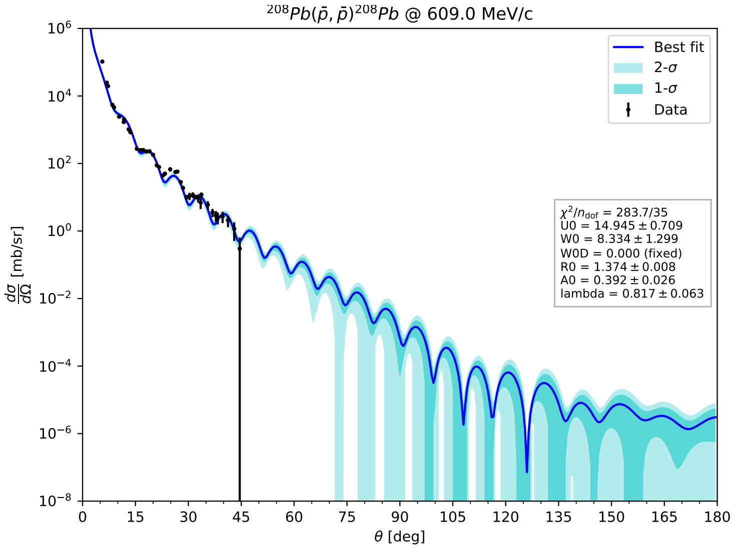

(a)

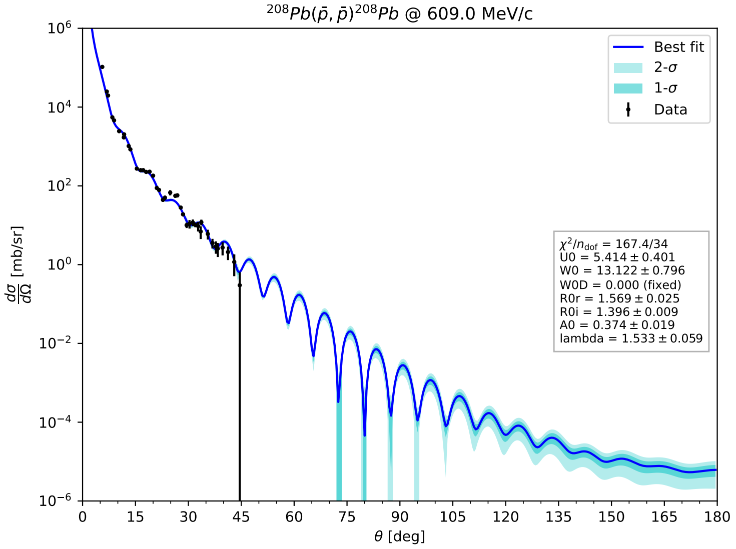

(b)

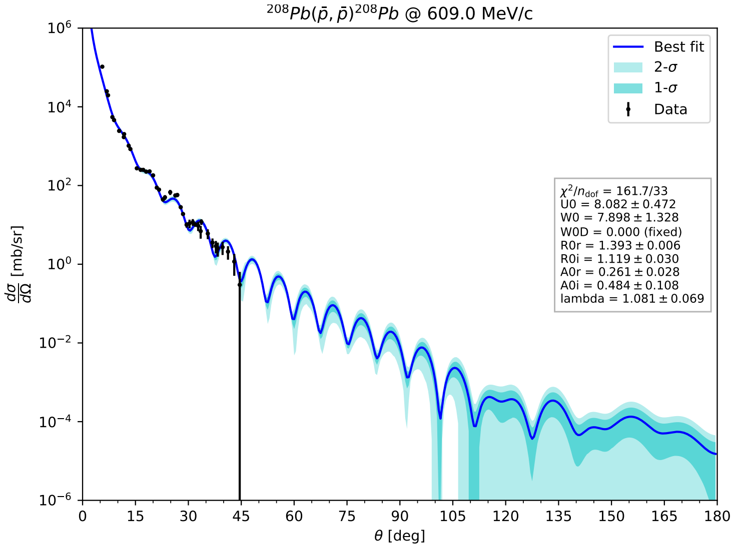

(c)

Figure B.7: 6- (B.7a), 7- (B.7b) and 8- (B.7c) parameters best-fit curve with error bands at 1-σ and 2-σ for ^{208}Pb at $E_{\bar{p}} = 179.8\,\mathrm{MeV}$[?]$(p = 609\,\mathrm{MeV/c})$ between $0° - 180°$.

B.2 Effects of the parameter changes on the cross section values

Figures B.8 and B.9 are exemplifications of the possible effect of variation of the values of the parameters. In particular, in Figure B.8, the variations are in the potential strengths (U_0 and W_0). In Figure B.9, the variations are in the diffusenesses (a_R and a_I). Variations in strengths cause slight changes in the cross section curves, while minimal changes in the diffuseness values may result in big changes in the cross section values.

The Figure B.10 shows a scan over all the parameters, leaving the others unvaried. It can be noted that in the region where experimental data are present, no appreciable changes in cross sections are observed. This is done for $p = 466\,\mathrm{MeV/c}$ to see specifically the case of ^{12}C data mentioned in Section 4.2.

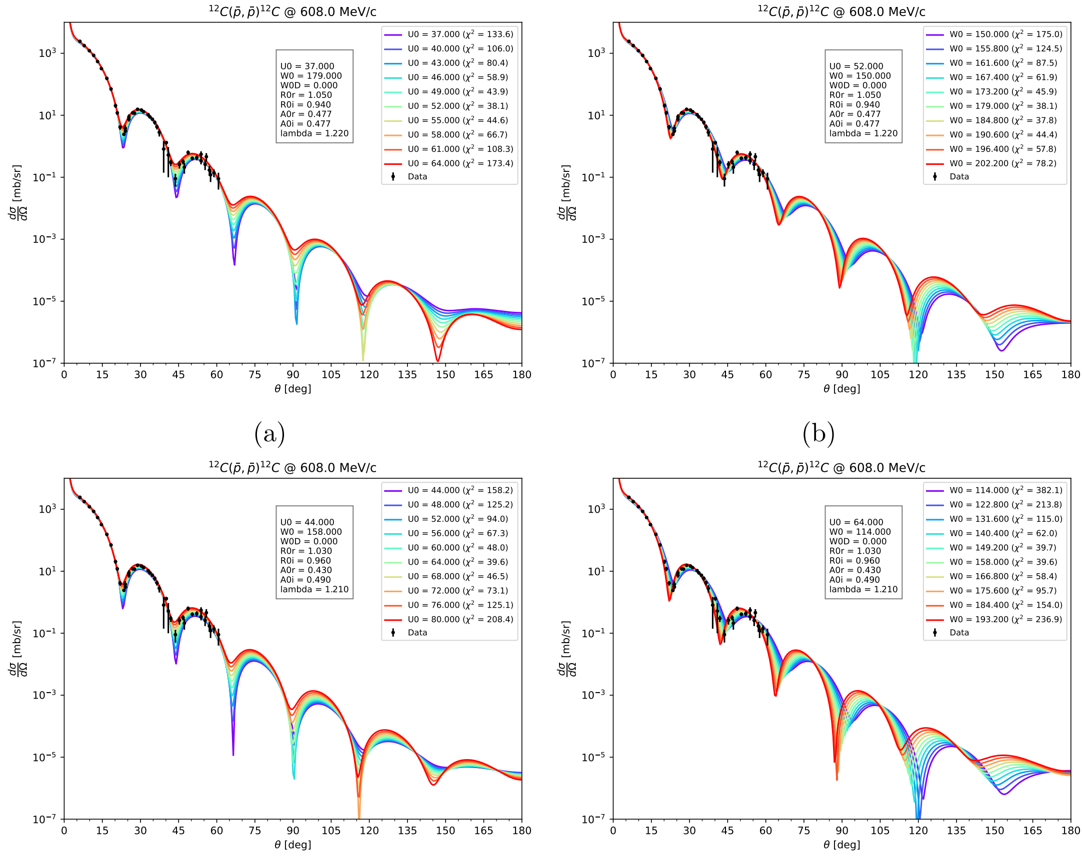

(a)

(b)

(c)

(d)

Figure B.8: Scan of real (B.8a, B.8c) and imaginary (B.8b,B.8d) strengths (U_0, W_0) with the other parameters fixed with the values of 6- and 7-parameter fit results from Table 4.2. The variations of the parameters are the minimum and maximum values considering the estimation errors of the fitting procedure.

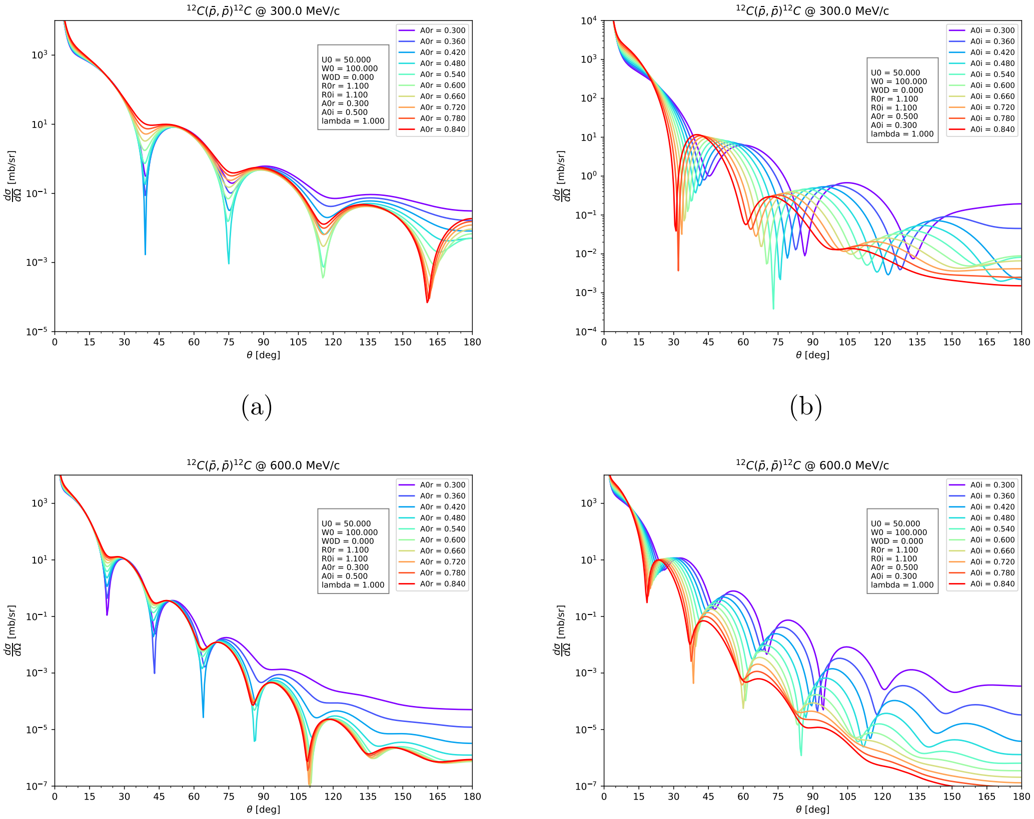

(a)

(b)

(c)

(d)

Figure B.9: Scan of real (B.9a, B.9c) and imaginary (B.9b,B.9d) diffuseness (a_R, a_I) with the other parameters fixed and different momenta ($p = 300\,\mathrm{MeV/c}$ first row, $p = 600\,\mathrm{MeV/c}$ second row). The choice of the parameter values is arbitrary since the figure is meant to show only the effect of variation of these variables. The parameter values are: $U_0 = 50\,\mathrm{MeV}$, $W_0 = 100\,\mathrm{MeV}$, $r_{0R} = r_{0I} = 1.1\,\mathrm{fm}$, $a_R = a_I = 0.5\,\mathrm{fm}$. λ is kept fixed to 1.

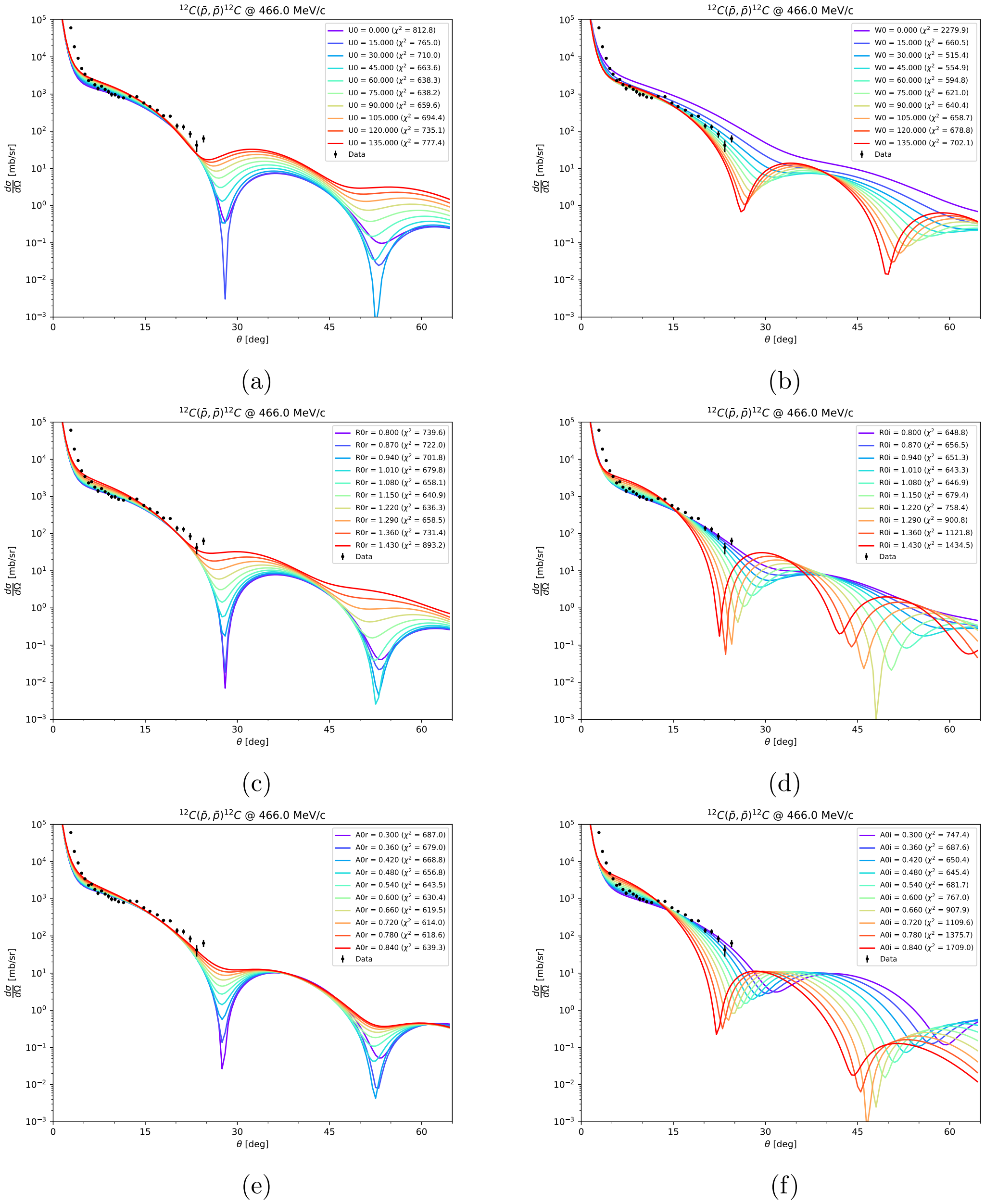

Figure B.10: Scan of all parameters for the ^{12}C case at 466 MeV/c: (B.10a) variation in U_0 between 0–135 MeV; (B.10b) variation in W_0 between 0–135 MeV; (B.10c) variation in r_{0R} between 0.8–1.43 fm; (B.10d) variation in r_{0I} between 0.8–1.43 fm; (B.10e) variation in a_R between 0.3–0.84 fm; (B.10f) variation in a_I between 0.3–0.84 fm. When they are not varied, the parameters are fixed to the same values of Figure B.9.

B.3 Probability of antineutron-neutron oscillation in time

From Equation (5.4), the probability of antineutron-neutron oscillation in dependence of time can be calculated. In Figure B.11 a graphical representation of this probability using the different values of $\tau_{\bar{n}n}$ is shown. As specified in Section 5.4, since the $\tau_{\bar{n}n}$ is a lower limit, $P_{\bar{n}}(t)$ is an upper limit and we must consider the colored region under the curve. In the figure, we called the lower limits of the antineutron-neutron oscillation time τ to distinguish it from the true value $\tau_{\bar{n}n}$ (therefore $\tau_{\bar{n}n} > \tau$).

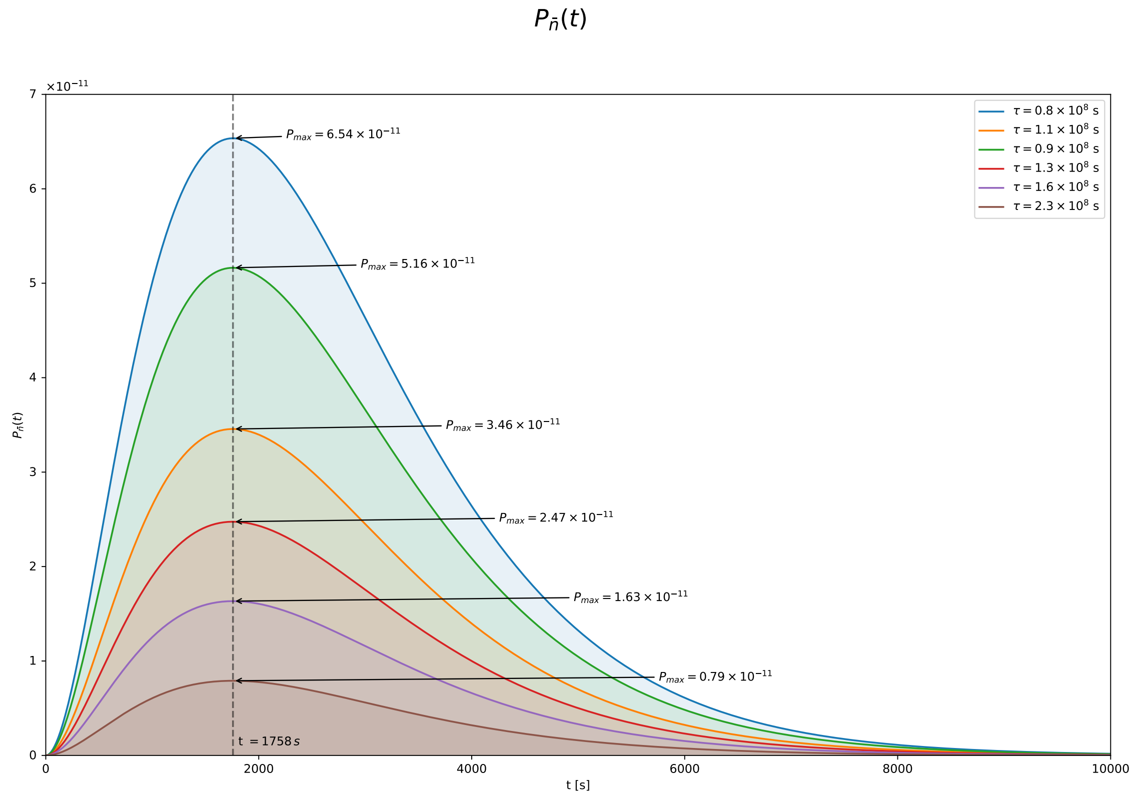

Figure B.11: Probability of $\bar{n} - n$ oscillations in time (between 0 and 10 000 s) with the six lower-limit mean values obtained in Section 5.4. The colored areas highlight the regions where $\tau_{\bar{n}n} > \tau$.

Appendix C

Supplementary tables

C.1 Correlation matrices

In this section, the correlation matrices of the fits presented in Chapters 4 and 5 are shown. The colors of the cells indicate the proximity to the extreme of the correlation values (1 = red, -1 = blue).

	U_0	W_0	r_0	a	λ
U_0	1	0.987	-0.985	0.954	-0.28
W_0	0.987	1	-0.996	0.973	-0.155
r_0	-0.985	-0.996	1	-0.986	0.131
a	0.954	0.973	-0.986	1	-0.042
λ	-0.28	-0.155	0.131	-0.042	1

(a)

	U_0	W_0	r_0	a	λ
U_0	1	0.935	-0.941	0.722	-0.152
W_0	0.935	1	-0.979	0.776	0.025
r_0	-0.941	-0.979	1	-0.862	-0.084
a	0.722	0.776	-0.862	1	0.316
λ	-0.152	0.025	-0.084	0.316	1

(b)

Table C.1: Correlation values for 5-parameters fit of ^{12}C at 300 MeV/c (C.1a) and 608 MeV/c (C.1b).

	U_0	W_0	r_{0R}	r_{0I}	a	λ
U_0	1	0.584	-0.933	-0.452	0.771	-0.21
W_0	0.584	1	-0.818	-0.984	0.904	0.653
r_{0R}	-0.933	-0.818	1	0.725	-0.938	-0.147
r_{0I}	-0.452	-0.984	0.725	1	-0.863	-0.757
a	0.771	0.904	-0.938	-0.863	1	0.411
λ	-0.21	0.653	-0.147	-0.757	0.411	1

(a)

	U_0	W_0	r_{0R}	r_{0I}	a	λ
U_0	1	-0.403	-0.99	0.211	0.421	-0.427
W_0	-0.403	1	0.333	-0.967	0.434	0.214
r_{0R}	-0.99	0.333	1	-0.131	-0.514	0.347
r_{0I}	0.211	-0.967	-0.131	1	-0.63	-0.204
a	0.421	0.434	-0.514	-0.63	1	0.168
λ	-0.427	0.214	0.347	-0.204	0.168	1

(b)

Table C.2: Same as Table C.1 with 6-parameters correlation coefficients.

	U_0	W_0	r_{0R}	r_{0I}	a_R	a_I	λ
U_0	1	0.489	-0.862	-0.19	0.314	0.178	-0.366
W_0	0.489	1	-0.597	-0.787	0.137	0.429	0.54
r_{0R}	-0.862	-0.597	1	0.074	-0.7	0.155	-0.039
r_{0I}	-0.19	-0.787	0.074	1	0.486	-0.862	-0.379
a_R	0.314	0.137	-0.7	0.486	1	-0.779	0.233
a_I	0.178	0.429	0.155	-0.862	-0.779	1	-0.057
λ	-0.366	0.54	-0.039	-0.379	0.233	-0.057	1

(a)

	U_0	W_0	r_{0R}	r_{0I}	a_R	a_I	λ
U_0	1	-0.573	-0.808	0.491	-0.08	0.266	-0.729
W_0	-0.573	1	0.169	-0.917	0.492	-0.127	0.635
r_{0R}	-0.808	0.169	1	-0.288	-0.515	0.173	0.487
r_{0I}	0.491	-0.917	-0.288	1	-0.153	-0.268	-0.616
a_R	-0.08	0.492	-0.515	-0.153	1	-0.74	0.17
a_I	0.266	-0.127	0.173	-0.268	-0.74	1	-0.022
λ	-0.729	0.635	0.487	-0.616	0.17	-0.022	1

(b)

Table C.3: Same as Table C.1 with 7-parameters correlation coefficients.

	U_0	W_0	r_0	a	λ
U_0	1	0.987	-0.985	0.954	-0.28
W_0	0.987	1	-0.996	0.973	-0.155
r_0	-0.985	-0.996	1	-0.986	0.131
a	0.954	0.973	-0.986	1	-0.042
λ	-0.28	-0.155	0.131	-0.042	1

(a)

	U_0	W_0	r_0	a	λ
U_0	1	0.935	-0.941	0.722	-0.152
W_0	0.935	1	-0.979	0.776	0.025
r_0	-0.941	-0.979	1	-0.862	-0.084
a	0.722	0.776	-0.862	1	0.316
λ	-0.152	0.025	-0.084	0.316	1

(b)

Table C.4: Correlation values for 5-parameters fit of ^{40}Ca at 303.3 MeV/c (C.4a) and 608 MeV/c (C.4b).

	U_0	W_0	r_{0R}	r_{0I}	a	λ
U_0	1	-0.706	-0.995	0.947	0.978	0.212
W_0	-0.706	1	0.712	-0.656	-0.813	-0.282
r_{0R}	-0.995	0.712	1	-0.939	-0.979	-0.215
r_{0I}	0.947	-0.656	-0.939	1	0.909	0.324
a	0.978	-0.813	-0.979	0.909	1	0.182
λ	0.212	-0.282	-0.215	0.324	0.182	1

(a)

	U_0	W_0	r_{0R}	r_{0I}	a	λ
U_0	1	-0.002	-0.878	-0.023	0.342	-0.765
W_0	-0.002	1	-0.427	-0.982	0.84	0.447
r_{0R}	-0.878	-0.427	1	0.458	-0.708	0.417
r_{0I}	-0.023	-0.982	0.458	1	-0.881	-0.431
a	0.342	0.84	-0.708	-0.881	1	0.226
λ	-0.765	0.447	0.417	-0.431	0.226	1

(b)

Table C.5: Same as Table C.4 with 6-parameters correlation coefficients.

	U_0	W_0	r_0	a	λ
U_0	1	0.495	-0.847	0.557	-0.426
W_0	0.495	1	-0.35	-0.152	-0.286
r_0	-0.847	-0.35	1	-0.439	0.43
a	0.557	-0.152	-0.439	1	-0.453
λ	-0.426	-0.286	0.43	-0.453	1

(a)

	U_0	W_0	r_0	a	λ
U_0	1	0.998	-0.997	0.984	0.863
W_0	0.998	1	-0.999	0.986	0.877
r_0	-0.997	-0.999	1	-0.991	-0.876
a	0.984	0.986	-0.991	1	0.87
λ	0.863	0.877	-0.876	0.87	1

(b)

Table C.6: Correlation values for 5-parameters fit of ^{208}Pb at 304.9 MeV/c (C.6a) and 609 MeV/c (C.6b).

	U_0	W_0	r_{0R}	r_{0I}	a	λ
U_0	1	0.155	-0.987	-0.142	0.385	0.115
W_0	0.155	1	-0.128	-0.808	0.322	-0.061
r_{0R}	-0.987	-0.128	1	0.16	-0.494	-0.107
r_{0I}	-0.142	-0.808	0.16	1	-0.45	0.128
a	0.385	0.322	-0.494	-0.45	1	0.168
λ	0.115	-0.061	-0.107	0.128	0.168	1

(a)

	U_0	W_0	r_{0R}	r_{0I}	a	λ
U_0	1	0.109	-0.83	-0.67	0.033	-0.605
W_0	0.109	1	-0.010	-0.347	0.691	-0.494
r_{0R}	-0.83	-0.010	1	0.829	0.156	0.235
r_{0I}	-0.67	-0.347	0.829	1	-0.213	0.331
a	0.033	0.691	0.156	-0.213	1	-0.228
λ	-0.605	-0.494	0.235	0.331	-0.228	1

(b)

Table C.7: Same as Table C.6 with 6-parameters correlation coefficients.

	U_0	W_0	r_{0R}	r_{0I}	a_R	a_I	λ
U_0	1	0.63	-0.378	-0.589	0.57	0.559	-0.456
W_0	0.63	1	-0.429	-0.996	0.156	0.979	0.209
r_{0R}	-0.378	-0.429	1	0.426	-0.109	-0.389	0.116
r_{0I}	-0.589	-0.996	0.426	1	-0.129	-0.986	-0.256
a_R	0.57	0.156	-0.109	-0.129	1	0.171	-0.212
a_I	0.559	0.979	-0.389	-0.986	0.171	1	0.334
λ	-0.456	0.209	0.116	-0.256	-0.212	0.334	1

(a)

	U_0	W_0	r_{0R}	r_{0I}	a_R	a_I	λ
U_0	1	0.0766	-0.021	0.489	0.462	0.294	-0.561
W_0	0.0766	1	0.201	0.492	-0.342	0.876	0.497
r_{0R}	-0.021	0.201	1	0.316	-0.473	0.38	0.208
r_{0I}	0.489	0.492	0.316	1	-0.105	0.684	0.358
a_R	0.462	-0.342	-0.473	-0.105	1	-0.37	-0.534
a_I	0.294	0.876	0.38	0.684	-0.37	1	0.465
λ	-0.561	0.497	0.208	0.358	-0.534	0.465	1

(b)

Table C.8: Same as Table C.6 with 7-parameters correlation coefficients.

C.2 Antineutron-neutron oscillation time

In Tables C.9a and C.9b, we report the values of the $\tau_{\bar{n}n}$ calculated with the different values of V_n and τ_A. The graphic representations of the tables are in Figures 5.14 and 5.15. Two averages are calculated: for target (row) and momentum (column).

$\bar{n} - n$ oscillation time with $\tau_A = 1.7 \times 10^{31}$ yr

		$V_n = 26\,\mathrm{MeV}$			$V_n = 60\,\mathrm{MeV}$		
Target	n_{par}	$\tau_{\bar{n}n}$ $[\times 10^8$ s]		τ_{av} $[\times 10^8$ s]	$\tau_{\bar{n}n}$ $[\times 10^8$ s]		τ_{av} $[\times 10^8$ s]
		300 MeV/c	600 MeV/c		300 MeV/c	600 MeV/c	
^{12}C	6	1.550	0.641	1.265	0.874	0.665	0.750
	7	2.064	0.621		0.834	0.627	
	8	2.064	0.650		0.834	0.668	
^{16}O	6	—	0.979	0.983	—	0.943	0.952
	7	—	0.981		—	0.956	
	8	—	0.990		—	0.958	
^{40}Ca	6	0.141	1.381	0.922	0.156	1.017	0.848
		0.559	—		0.992	—	
	7	0.503	1.362		0.875	1.002	
	8	—	1.584		—	1.045	
^{208}Pb	6	1.204	1.737	1.112	1.603	0.519	0.643
	7	0.108	1.246		0.125	0.542	
	8	1.165	1.212		0.619	0.453	
τ_{av} $[\times 10^8$ s]		1.040	1.115	1.071 1.078	0.768	0.783	0.798 0.776

(a)

$\bar{n} - n$ oscillation time with $\tau_A = 2.4 \times 10^{31}$ yr

		$V_n = 26\,\mathrm{MeV}$			$V_n = 60\,\mathrm{MeV}$		
Target	n_{par}	$\tau_{\bar{n}n}$ $[\times 10^8$ s]		τ_{av} $[\times 10^8$ s]	$\tau_{\bar{n}n}$ $[\times 10^8$ s]		τ_{av} $[\times 10^8$ s]
		300 MeV/c	600 MeV/c		300 MeV/c	600 MeV/c	
^{12}C	6	1.842	0.762	1.503	1.039	0.790	0.892
	7	2.453	0.738		0.991	0.745	
	8	2.453	0.772		0.991	0.794	
^{16}O	6	—	1.163	1.168	—	1.121	1.132
	7	—	1.165		—	1.136	
	8	—	1.176		—	1.138	
^{40}Ca	6	0.167	1.641	1.095	0.185	1.208	1.008
		0.664	—		1.179	—	
	7	0.597	1.619		1.040	1.191	
	8	—	1.882		—	1.242	
^{208}Pb	6	1.430	2.063	1.321	1.904	0.616	0.764
	7	0.129	1.480		0.149	0.643	
	8	1.384	1.440		0.736	0.538	
τ_{av} $[\times 10^8$ s]		1.235	1.325	1.272 1.280	0.913	0.930	0.949 0.922

(b)

Table C.9: Calculations of lower limit of $\tau_{\bar{n}n}$ for the different fits obtained and mean values concerning the target (last column) and concerning the momentum (last row) for $\tau_A = 1.7 \times 10^{31}$ yr (C.9a) and $\tau_A = 2.4 \times 10^{31}$ yr (C.9b).

Bibliography

[1] R. Bizzarri, P. Guidoni, F. Marcelja, F. Marzano, E. Castelli, and M. Sessa, “Antiproton-deuteron low-energy cross-sections”, Il Nuovo Cimento A (1965-1970) **22**, 225–250 (1974).

[2] B. Gunderson, J. Learned, J. Mapp, and D. Reeder, “Measurement of the antineutron-proton cross section at low energy”, Physical Review D **23**, 587 (1981).

[3] F. Balestra, Y. A. Batusov, G. Bendiscioli, M. Bussa, L. Busso, I. Falomkin, L. Ferrero, V. Filippini, G. Fumagalli, G. Gervino, et al., “P4he reaction cross section at 610 mev/c”, Physics Letters B **149**, 69–72 (1984).

[4] F. Balestra, S. Bossolasco, M. Bussa, L. Bussa, L. Ferrero, D. Panzieri, G. Piragino, F. Tosello, C. Guaraldo, A. Maggiora, et al., “Inelastic interaction of antiprotons with 4he nuclei between 200 and 600 mev/c”, Physics Letters B **165**, 265–269 (1985).

[5] M. Agnello, F. Iazzi, B. Minetti, L. Cugusi, M. Macciotta, S. Marcello, A. Masoni, G. Puddu, A. Raimondi, S. Serci, et al., “Measurement of the annihilation cross-section for antineutrons on fe from 100 to 531 mev/c”, EPL (Europhysics Letters) **7**, 13 (1988).

[6] F. Balestra, R. Barbieri, Y. A. Batusov, G. Bendiscioli, S. Bossolasco, F. Breivik, M. Bussa, L. Busso, C. Guaraldo, I. Falomkin, et al., “Antiproton-helium annihilation around 45 mev/c”, Physics Letters B **230**, 36–40 (1989).

[7] W. Brückner, B. Cujec, H. Döbbeling, K. Dworschak, F. Güttner, H. Kneis, S. Majewski, M. Nomachi, S. Paul, B. Povh, et al., “Measurements of the antiproton-proton annihilation cross-section in the beam momentum range between 180 and 600 mev/c”, Zeitschrift für Physik A Atomic Nuclei **335**, 217–229 (1990).

[8] V. Ableev, A. Adamo, M. Agnello, F. Balestra, G. Belli, G. Bendiscioli, A. Bertin, P. Boccaccio, G. Bonazzola, E. Botta, et al., “Annihilation cross-sections of antineutrons on c, al, cu, sn and pb at low momenta (180–280 mev/c) with the obelix spectrometer”, Il Nuovo Cimento A (1965-1970) **107**, 943–953 (1994).

[9] C. Barbina, A. Ahmidouch, R. Birsa, F. Bradamante, A. Bressan, S. Dalla Torre-Colautti, M. Giorgi, R. Hess, F. Iazzi, R. Kunne, et al., “Measurement of the $\bar{n}$-fe absorption cross section between 125 and 780 mev/c”, Nuclear Physics A **612**, 346–358 (1997).

[10] A. Benedettini, A. Bertin, M. Bruschi, M. Capponi, A. Collamati, I. D'Antone, S. De Castro, R. Dona, A. Ferretti, D. Galli, et al., "$\bar{p}p$ Partial cross sections at low energy", Nuclear Physics B-Proceedings Supplements **56**, 58–65 (1997).

[11] A. Zenoni, A. Bianconi, F. Bocci, G. Bonomi, M. Corradini, A. Donzella, E. Lodi Rizzini, L. Venturelli, A. Bertin, M. Bruschi, et al., "New measurements of the pp annihilation cross section at very low energy", Physics Letters B **461**, 405–412 (1999).

[12] A. Zenoni, A. Bianconi, G. Bonomi, M. Corradini, A. Donzella, E. Lodi Rizzini, L. Venturelli, A. Bertin, M. Bruschi, M. Capponi, et al., "$\bar{p}$D and $\bar{p}^4$he annihilation cross sections at very low energy", Physics Letters B **461**, 413–416 (1999).

[13] A. Bianconi, G. Bonomi, M. Bussa, E. Lodi Rizzini, L. Venturelli, A. Zenoni, G. Pontecorvo, C. Guaraldo, F. Balestra, L. Busso, et al., "Antiproton–neon annihilation at 57 mev/c", Physics Letters B **481**, 194–198 (2000).

[14] A. Bianconi, G. Bonomi, M. Bussa, E. Lodi Rizzini, L. Venturelli, A. Zenoni, G. Pontecorvo, C. Guaraldo, F. Balestra, L. Busso, et al., "Antiproton–helium 3 annihilation at 55 mev/c", Physics Letters B **492**, 254–258 (2000).

[15] F. Iazzi, A. Feliciello, M. Agnello, M. Astrua, E. Botta, T. Bressani, D. Calvo, S. Costa, F. D'Isep, A. Filippi, et al., "Antineutron–proton total cross section from 50 to 400 mev/c", Physics Letters B **475**, 378–385 (2000).

[16] M. Astrua, E. Botta, T. Bressani, D. Calvo, C. Casalegno, A. Feliciello, A. Filippi, S. Marcello, M. Agnello, and F. Iazzi, "Antineutron–nucleus annihilation cross sections below 400 mev/c", Nuclear Physics A **697**, 209–224 (2002).

[17] A. Bianconi, M. Corradini, M. Hori, M. Leali, E. Lodi Rizzini, V. Mascagna, A. Mozzanica, M. Prest, E. Vallazza, L. Venturelli, et al., "Measurement of the antiproton–nucleus annihilation cross section at 5.3 mev", Physics Letters B **704**, 461–466 (2011).

[18] H. Aghai-Khozani, A. Bianconi, M. Corradini, R. Hayano, M. Hori, M. Leali, E. Lodi Rizzini, V. Mascagna, Y. Murakami, M. Prest, E. Vallazza, L. Venturelli, and H. Yamada, "Measurement of the antiproton–nucleus annihilation cross-section at low energy", en, Nuclear Physics A **970**, 366–378 (2018).

[19] M. Corradini, R. Hayano, M. Hori, M. Leali, E. Lodi Rizzini, V. Mascagna, A. Mozzanica, M. Prest, K. Todoroki, E. Vallazza, L. Venturelli, N. Zurlo, C. Baratto, M. Ferroni, and A. Vomiero, "Experimental apparatus for annihilation cross-section measurements of low energy antiprotons", Nuclear Instruments and Methods in Physics Research Section A: Accelerators, Spectrometers, Detectors and Associated Equipment **711**, 12–20 (2013).

[20] K. Todoroki, D. Barna, R. Hayano, H. Aghai-Khozani, A. SÃ³tÃ©r, M. Corradini, M. Leali, E. Lodi-Rizzini, V. Mascagna, L. Venturelli, V. Prest, L. Vallazza, D. De Salvador, and M. Hori, "Instrumentation for measurement of in-flight annihilations of 130 kev antiprotons on thin target foils", Nuclear Instruments and Methods in Physics Research Section A: Accelerators, Spectrometers, Detectors and Associated Equipment **835**, 110–118 (2016).

[21] M. Corradini, M. Leali, E. L. Rizzini, V. Mascagna, M. Prest, E. Vallazza, and L. Venturelli, “Scintillating bar detector for antiproton annihilations measurements”, Hyperfine Interactions **233**, 53–58 (2015).

[22] H. Aghai-Khozani, D. Barna, M. Corradini, D. De Salvador, R. Hayano, M. Hori, M. Leali, E. Lodi-Rizzini, V. Mascagna, M. Prest, D. Seiler, A. Sótér, K. Todoroki, E. Vallazza, and L. Venturelli, “Limits on antiproton-nuclei annihilation cross sections at $\sim 125\,keV$”, Nuclear Physics A **1009**, 122170 (2021).

[23] A. G. Cohen, A. De Rújula, and S. L. Glashow, “A Matter-Antimatter Universe?”, en, The Astrophysical Journal **495**, 539–549 (1998).

[24] H. Kurki-Suonio and E. Sihvola, “Constraining antimatter domains in the early universe with big bang nucleosynthesis”, Phys. Rev. Lett. **84**, 3756–3759 (2000).

[25] K. Abe, H. Fuke, S. Haino, T. Hams, A. Itazaki, K. Kim, T. Kumazawa, M. Lee, Y. Makida, S. Matsuda, K. Matsumoto, J. Mitchell, A. Moiseev, Z. Myers, J. Nishimura, M. Nozaki, R. Orito, J. Ormes, M. Sasaki, E. Seo, Y. Shikaze, R. Streitmatter, J. Suzuki, Y. Takasugi, K. Takeuchi, K. Tanaka, T. Yamagami, A. Yamamoto, T. Yoshida, and K. Yoshimura, “Measurement of the cosmic-ray low-energy antiproton spectrum with the first bess-polar antarctic flight”, Physics Letters B **670**, 103–108 (2008).

[26] T. Aramaki, S. Boggs, P. von Doetinchem, H. Fuke, C. Hailey, S. Mognet, R. Ong, K. Perez, and J. Zweerink, “Potential for precision measurement of low-energy antiprotons with gaps for dark matter and primordial black hole physics”, Astroparticle Physics **59**, 12–17 (2014).

[27] L. Gray and T. E. Kalogeropoulos, “Possible biomedical applications of antiproton beams: focused radiation transfer”, Radiation Research **97**, 246–252 (1984).

[28] M. H. Holzscheiter, N. Bassler, N. Agazaryan, G. Beyer, E. Blackmore, J. J. DeMarco, M. Doser, R. E. Durand, O. Hartley, K. S. Iwamoto, H. V. Knudsen, R. Landua, C. Maggiore, W. H. McBride, S. P. Møller, J. Petersen, L. D. Skarsgard, J. B. Smathers, T. D. Solberg, U. I. Uggerhøj, S. Vranjes, H. R. Withers, M. Wong, and B. G. Wouters, “The biological effectiveness of antiproton irradiation”, Radiotherapy and Oncology **81**, 233–242 (2006).

[29] N. Bassler, M. Holzscheiter, and H. Knudsen, “Cancer therapy with antiprotons”, AIP Conference Proceedings **796**, 423–430 (2005).

[30] H. Feshbach, “The Optical Model and Its Justification”, en, Annu. Rev. Nucl. Sci. **8**, 49–104 (1958).

[31] P. E. Hodgson, “The nuclear optical model”, Rep. Prog. Phys. **34**, 765–819 (1971).

[32] C. Batty, E. Friedman, and A. Gal, “Unified optical-model approach to low-energy antiproton annihilation on nuclei and to antiprotonic atoms”, en, Nuclear Physics A **689**, 721–740 (2001).

[33] K. V. Protasov, V. Gudkov, E. A. Kupriyanova, V. V. Nesvizhevsky, W. M. Snow, and A. Y. Voronin, “Theoretical analysis of antineutron-nucleus data needed for antineutron mirrors in neutron-antineutron oscillation experiments”, en, Phys. Rev. D **102**, 075025 (2020).

[34] V. V. Nesvizhevsky, V. Gudkov, K. V. Protasov, W. M. Snow, and A. Y. Voronin, “Experimental Approach to Search for Free Neutron-Antineutron Oscillations Based on Coherent Neutron and Antineutron Mirror Reflection”, en, Phys. Rev. Lett. **122**, 221802 (2019).

[35] A. D. Sakharov, “Violation of cp invariance, c asymmetry, and baryon asymmetry of the universe”, Soviet Physics Uspekhi **34**, 392 (1991).

[36] T.-G. Lee and C.-Y. Wong, “Optical model potential analysis of $\bar{n}$-A and n-A interactions”, en, Phys. Rev. C **97**, 054617 (2018).

[37] W. Dickhoff and R. Charity, “Recent developments for the optical model of nuclei”, en, Progress in Particle and Nuclear Physics **105**, 252–299 (2019).

[38] J. W. Holt and T. R. Whitehead, *Modern approaches to optical potentials*, arXiv:2201.13404 [nucl-th], June 2022.

[39] C. D. Anderson, “The positive electron”, Phys. Rev. **43**, 491–494 (1933).

[40] O. Chamberlain, E. Segrè, C. Wiegand, and T. Ypsilantis, “Observation of antiprotons”, Phys. Rev. **100**, 947–950 (1955).

[41] B. Cork, G. Lambertson, O. Piccioni, and W. Wenzel, “Antineutrons produced from antiprotons in charge-exchange collisions”, Phys. Rev. **104**, 1193–1197 (1956).

[42] M. Hori, A. Sótér, D. Barna, A. Dax, R. Hayano, S. Friedreich, B. Juhász, T. Pask, E. Widmann, D. Horváth, L. Venturelli, and N. Zurlo, “Two-photon laser spectroscopy of antiprotonic helium and the antiproton-to-electron mass ratio”, Nature **475**, 484–488 (2011).

[43] D. Griffiths, *Introduction to elementary particles* (John Wiley & Sons, New York, USA, 1987).

[44] E. Segrè, *Nuclei and Particles: An Introduction to Nuclear and Subnuclear Physics*, Nuclei and Particles: An Introduction to Nuclear and Subnuclear Physics v. 33 (W.A. Benjamin, 1964).

[45] D. Garreta, P. Birien, G. Bruge, A. Chaumeaux, D. Drake, S. Janouin, D. Legrand, M. Lemaire, B. Mayer, J. Pain, J. Peng, M. Berrada, J. Bocquet, E. Monnand, J. Mougey, P. Perrin, E. Aslanides, O. Bing, J. Lichtenstadt, and A. Yavin, “Elastic scattering of antiprotons from carbon, calcium, and lead at 180 MeV”, en, Physics Letters B **149**, 64–68 (1984).

[46] D. Garreta, P. Birien, G. Bruge, A. Chaumeaux, D. Drake, S. Janouin, D. Legrand, M. Mallet-Lemaire, B. Mayer, J. Pain, J. Peng, M. Berrada, J. Bocquet, E. Monnand, J. Mougey, P. Perrin, E. Aslanides, O. Bing, A. Erell, J. Lichtenstadt, and A. Yavin, “Scattering of antiprotons from carbon at 46.8 MeV”, en, Physics Letters B **135**, 266–270 (1984).

[47] H. Heiselberg, A. Jensen, A. Miranda, G. Oades, and O. Dumbrajs, “Phenomenological analyses of antiproton elastic scattering data”, en, Nuclear Physics A **446**, 637–656 (1985).

[48] S. Janouin, M.-C. Lemaire, D. Garreta, P. Birien, G. Bruge, D. Drake, D. Legrand, B. Mayer, J. Pain, J. Peng, M. Berrada, J. Bocquet, E. Monnand, J. Mougey, P. Perrin, E. Aslanides, O. Bing, J. Lichtenstadt, and A. Yavin, "Optical-model analysis of antiproton-nucleus elastic scattering at 50 and 180 MeV", en, Nuclear Physics A **451**, 541–561 (1986).

[49] C.-Y. Wong, A. K. Kerman, G. R. Satchler, and A. D. MacKellar, "Ambiguity in antiproton-nucleus potentials from antiprotonic-atom data", en, Phys. Rev. C **29**, 574–580 (1984).

[50] K.-I. Kubo, H. Toki, and M. Igarashi, "Optical-potential description of antiproton-nucleus scattering at 46.8 MeV", en, Nuclear Physics A **435**, 708–716 (1985).

[51] V. Ashford, M. E. Sainio, M. Sakitt, J. Skelly, R. Debbe, W. Fickinger, R. Marino, and D. K. Robinson, "Low energy antiproton nuclear absorption cross sections", Phys. Rev. C **31**, 663–665 (1985).

[52] A. Rohatgi, *Webplotdigitizer: v4.6*, `https://automeris.io/WebPlotDigitizer`, 2022.

[53] P. E. Hodgson, "The optical model of the nucleon-nucleus interaction", en, Annu. Rev. Nucl. Sci. **17**, 1–32 (1967).

[54] N. S. Chant and P. G. Roos, "`THREEDEE` code", (unpublished), 1998.

[55] N. K. Glendenning, *Direct nuclear reactions*, en (World Scientific, New Jersey, 2004).

[56] E. W. Schmid, G. Spitz, and W. Lösch, *Theoretical Physics on the Personal Computer*, en (Springer Berlin Heidelberg, Berlin, Heidelberg, 1990).

[57] K. Nakamura, J. Chiba, T. Fujii, H. Iwasaki, T. Kageyama, S. Kuribayashi, T. Sumiyoshi, T. Takeda, H. Ikeda, and Y. Takada, "Absorption and forward scattering of antiprotons by c, al, and cu nuclei in the region 470-880 mev/c", Phys. Rev. Lett. **52**, 731–734 (1984).

[58] H. Dembinski and P. O. et al., "Scikit-hep/iminuit", `10.5281/zenodo.3949207` (2020).

[59] F. James and M. Roos, "Minuit: A System for Function Minimization and Analysis of the Parameter Errors and Correlations", Comput. Phys. Commun. **10**, 343–367 (1975).

[60] C. B. Dover, A. Gal, and J. M. Richard, "Neutron-antineutron oscillations in nuclei", Phys. Rev. D **27**, 1090–1100 (1983).

[61] O. V. Bespalova, E. A. Romanovsky, and T. I. Spasskaya, "Nucleon–nucleus real potential of Woods–Saxon shape between -60 and $+60$ mev for the $40 \leq a \leq 208$ nuclei", Journal of Physics G: Nuclear and Particle Physics **29**, 1193 (2003).

[62] T. W. Jones, R. M. Bionta, G. Blewitt, C. B. Bratton, B. G. Cortez, S. Errede, G. W. Foster, W. Gajewski, K. S. Ganezer, M. Goldhaber, T. J. Haines, D. Kielczewska, W. R. Kropp, J. G. Learned, E. Lehmann, J. M. LoSecco, H. S. Park, F. Reines, J. Schultz, E. Shumard, D. Sinclair, H. W. Sobel, J. L. Stone, L. R. Sulak, R. Svoboda, J. C. van der Velde, and C. Wuest (Irvine-Michigan-Brookhaven Collaboration), "Search for $n - \overline{n}$ oscillation in oxygen", Phys. Rev. Lett. **52**, 720–723 (1984).

[63] J. Chung, W. W. M. Allison, G. J. Alner, D. S. Ayres, W. L. Barrett, P. M. Border, J. H. Cobb, H. Courant, D. M. Demuth, T. H. Fields, H. R. Gallagher, M. C. Goodman, R. Gran, T. Joffe-Minor, T. Kafka, S. M. S. Kasahara, P. J. Litchfield, W. A. Mann, M. L. Marshak, R. H. Milburn, W. H. Miller, L. Mualem, A. Napier, W. P. Oliver, G. F. Pearce, E. A. Peterson, D. A. Petyt, K. Ruddick, M. Sanchez, J. Schneps, A. Sousa, B. Speakman, J. L. Thron, S. P. Wakely, and N. West, "Search for neutron-antineutron oscillations using multiprong events in soudan 2", Phys. Rev. D **66**, 032004 (2002).

[64] M. Baldo-Ceolin, P. Benetti, T. Bitter, F. Bobisut, E. Calligarich, R. Dolfini, D. Dubbers, P. El-Muzeini, M. Genoni, D. Gibin, A. Gigli Berzolari, K. Gobrecht, A. Guglielmi, J. Last, M. Laveder, W. Lippert, F. Mattioli, F. Mauri, M. Mezzetto, C. Montanari, A. Piazzoli, G. Puglierin, A. Rappoldi, G. L. Raselli, D. Scannicchio, A. Sconza, M. Vascon, and L. Visentin, "A new experimental limit on neutron-antineutron oscillations", Zeitschrift für Physik C Particles and Fields **63**, 409–416 (1994).

[65] D. Phillips, W. Snow, K. Babu, S. Banerjee, D. Baxter, Z. Berezhiani, M. Bergevin, S. Bhattacharya, G. Brooijmans, L. Castellanos, M.-C. Chen, C. Coppola, R. Cowsik, J. Crabtree, P. Das, E. Dees, A. Dolgov, P. Ferguson, M. Frost, T. Gabriel, A. Gal, F. Gallmeier, K. Ganezer, E. Golubeva, G. Greene, B. Hartfiel, A. Hawari, L. Heilbronn, C. Johnson, Y. Kamyshkov, B. Kerbikov, M. Kitaguchi, B. Kopeliovich, V. Kopeliovich, V. Kuzmin, C.-Y. Liu, P. McGaughey, M. Mocko, R. Mohapatra, N. Mokhov, G. Muhrer, H. Mumm, L. Okun, R. Pattie, C. Quigg, E. Ramberg, A. Ray, A. Roy, A. Ruggles, U. Sarkar, A. Saunders, A. Serebrov, H. Shimizu, R. Shrock, A. Sikdar, S. Sjue, S. Striganov, L. Townsend, R. Tschirhart, A. Vainshtein, R. Van Kooten, Z. Wang, and A. Young, "Neutron-antineutron oscillations: theoretical status and experimental prospects", Physics Reports **612**, 1–45 (2016).

[66] E. Friedman, "Antineutron and antiproton nuclear interactions at very low energies", en, Nuclear Physics A **925**, 141–149 (2014).

[67] V. Chohan, C. Alanzeau, M. Angoletta, J. Baillie, D. Barna, W. Bartmann, P. Belochitskii, J. Borburgh, H. Breuker, F. Butin, M. Buzio, O. Capatina, C. Carli, E. Carlier, M. Cattin, T. Dobers, P. Chiggiato, L. Ducimetiere, T. Eriksson, and T. Zickler, *Extra low energy antiproton (elena) ring and its transfer lines: design report* (Apr. 2014).

[68] C. P. Welsch, A. Papash, O. Gorda, J. Harasimowicz, O. Karamyshev, G. Karamysheva, D. Newton, M. Panniello, M. Putignano, M. Siggel-King, et al., "Ultra-low energy storage ring at flair", Hyperfine Interactions **213**, 205–215 (2012).

[69] E. Widmann, "Low-energy antiprotons physics and the flair facility", Physica Scripta **2015**, 014074 (2015).

[70] A. Bianconi, G. Costantini, G. Gosta, M. Leali, V. Mascagna, S. Migliorati, and L. Venturelli, "Antiproton-nuclei cross sections with Woods-Saxon potential at low energies", in International Conference on Exotic Atoms and Related Topics - EXA2021, Vol. 262, European Physical Journal: Web of Conference (2022), p. 01018.

[71] PySimpleGUI, *PySimpleGUI*, GitHub, `www.PySimpleGUI.com`, 2021.

[72] H. Dembinski, *Hdembinski/jacobi*, GitHub, version v0.9.2, doi:10.5281/zenodo.8252808, Aug. 2023.